

# Impacts of Atmospheric Dynamics on Winter-Spring Sea-Ice and Snow Thickness at a Coastal Site in East Antarctica

4 Diana Francis<sup>1\*</sup>, Ricardo Fonseca<sup>1</sup>, Narendra Nelli<sup>1</sup>, Petra Heil<sup>2,3,4</sup> Jonathan D. Wille<sup>5</sup>, Irina V.  
5 Gorodetskaya<sup>6</sup>, Robert A. Massom<sup>2,3,7</sup>

<sup>7</sup> <sup>8</sup> <sup>1</sup>Environmental and Geophysical Sciences (ENGEOS) Lab, Earth Sciences Department, Khalifa University, Abu Dhabi, 127788, United Arab Emirates

<sup>9</sup> <sup>2</sup> Australian Antarctic Division, Department of Climate Change, Energy, the Environment and Water,  
10 Kingston, Tasmania, Australia

<sup>3</sup> Australian Antarctic Program Partnership, Institute for Marine and Antarctic Studies, University of Tasmania, Hobart, Tasmania, Australia

<sup>4</sup>Institute Snow and Avalanche Research, Swiss Federal Institute for Forest, Snow and Landscape Research, Davos, Switzerland

<sup>5</sup> Institute for Atmospheric and Climate Science, ETH Zurich, Zurich, Switzerland

<sup>16</sup> Interdisciplinary Centre of Marine and Environmental Research, University of Porto, Porto, Portugal

<sup>7</sup>The Australian Centre for Excellence in Antarctic Science, University of Tasmania, Hobart, Tasmania, Australia

19 \*Correspondence to: [diana.francis@ku.ac.ae](mailto:diana.francis@ku.ac.ae)

## 20 Abstract:

21 Antarctic sea ice and its snow cover play a pivotal role in regulating the global climate system  
22 through feedback on both the atmospheric and the oceanic circulations. Understanding the intricate  
23 interplay between atmospheric dynamics, mixed-layer properties, and sea ice is essential for  
24 accurate future climate change estimates. This study investigates the relationship between the  
25 atmospheric conditions and sea-ice and snow characteristics at a coastal East Antarctic site using  
26 *in-situ* measurements in winter-spring 2022. The observed sea-ice thickness peaks at 1.16 m in  
27 mid-late October and drops to 0.06 m at the end of November, following the seasonal solar cycle.  
28 On the other hand, while the snow thickness variability is impacted by atmospheric forcing, with  
29 significant contributions from precipitation, Foehn effects, blowing snow, and episodic warm and  
30 moist air intrusions~~katabatic flows and atmospheric rivers (ARs)~~, which can lead to changes of up  
31 to 0.08 m within a day for a field that is in the range 0.02-0.18 m during July-November 2022. The  
32 in-situ measurements highlight the substantial effects of warm and moist air intrusions on the sea-  
33 ice, snow and atmospheric state. A high-resolution simulation with the Polar Weather Research  
34 and Forecasting model for the 14 JulyNovember atmospheric river (AR), the only intense AR that

35 occurred during the study period, reveals the presence of AR rapids and highlights the effects of  
36 the katabatic winds from the Antarctic Plateau in slowing down the low-latitude air masses as they  
37 approach the Antarctica coastline, with the resulting low level convergence of the two air flows,  
38 with meridional wind speeds in excess of  $45 \text{ m s}^{-1}$ , leading to precipitation rates above  $3 \text{ mm hr}^{-1}$   
39 around coastal Antarctica. The unsteady wind field in response to the passage of a deep low  
40 pressure system with a central pressure that dropped to 931 hPa triggers satellite-derived pack ice  
41 drift speeds in excess of  $60 \text{ km day}^{-1}$ , and promotes the opening up of a polynya in the Southern  
42 Ocean around  $64^{\circ}\text{S}, 45^{\circ}\text{E}$  from 14 to 22 July. Including the observed sea ice extent and a realistic  
43 SIT in the model does not yield more skillful predictions of surface/near-surface variables and  
44 atmospheric profiles. This suggests other factors such as boundary layer dynamics and/or land/ice  
45 processes may play a more important role than sea ice concentration and thickness during AR  
46 events. Our findings contribute to a better understanding of the complex interactions within the  
47 Antarctic climate system, providing valuable insights for climate modeling and future projections.  
48

49 **Keywords:**

50 Sea Ice, Snow Thickness, PolarWRF, Atmospheric River, Katabatic winds, Foehn Effects,  
51 Antarctica

52

53 **1. Introduction**

54 Sea ice, which forms from the freezing of seawater and covers 3-6% of the total surface area  
55 of the planet (depending on season), plays multiple crucial roles in the Earth's climate system and  
56 high-latitude ecosystems (Thomas, 2017; Eayrs et al., 2019). Changes in the formation and melt  
57 rates, extent, seasonality and thickness of Antarctic sea ice - both in the form of drifting pack ice  
58 and less extensive stationary near-shore landfast ice (fast ice) attached to coastal margins, sea floor  
59 and grounded icebergs (Fraser et al., 2023) - substantially impact the heat and salinity content of  
60 the ocean, and hence the oceanic circulation (e.g., Haumann et al., 2016; Li and Fedorov, 2021).  
61 At the same time, breaks in the sea ice such as leads and recurrent and persistent polynyas (Barber  
62 and Massom, 2007; Francis et al. 2019, 2020; Fonseca et al., 2023) act as a thermal forcing, with  
63 the exposure of ice-free ocean water leading to sensible heat fluxes that can exceed  $2000 \text{ W m}^{-2}$   
64 and heat up the atmosphere aloft (Guest, 2021), directly impacting the atmospheric flow (Trusel  
65 et al., 2023; Zhang and Screen, 2021). Both oceanic and atmospheric forcing directly affect impact  
66 sea ice and its spatial extent, seasonality and thickness (Wang et al., 2020; Yang et al., 2021),  
67 within a finely-coupled interactive ocean-sea ice-atmosphere system. At the same time, decreases  
68 in sea-ice thickness (SIT), sea-ice extent (SIE), and its snow cover have strong potential to impact  
69 low-latitude weather patterns (England et al., 2020), disrupt the global surface energy balance  
70 (Riihelä et al., 2021), and amplify climate warming at high southern latitudes (Williams et al.,  
71 2023), leading to increased sea-ice loss that is likely to be further accelerated by poorly-understood  
72 ocean-ice-snow-atmosphere feedback mechanisms (Goosse et al., 2023).

73

The Antarctic sea ice-snow system is particularly impacted by two atmospheric processes: (1) strong katabatic winds that cascade seawards off the ice sheet and promote sublimation of the sea ice and its snow cover (Elvidge et al., 2020; Francis et al., 2023); and (2) a number of more ephemeral but influential extreme atmospheric events in the form of atmospheric rivers (ARs; Wille et al., 2025). Foehn effects are an important trigger of surface melting around Antarctica, as the adiabatic compression of the downslope flow can lead to a marked increase in surface temperature in excess of 15 K (Bozkurt et al., 2018), while the strong winds can promote iceberg calving events (Miles et al., 2017). An AR is a narrow and highly elongated band of moisture-rich air that originates in the tropics and subtropics and propagates polewards into the mid- and high-latitudes (Wille et al., 2019; Gorodetskaya et al., 2020). ARs are associated with increased humidity and cloudiness, leading to an enhancement of the downward longwave radiation flux while still allowing some of the Sun's shortwave radiation to reach the surface (Djouma and Holland, 2021). The resulting increase in the surface net radiation flux gives a warming tendency and promotes surface melting (Gorodetskaya et al., 2013; Francis et al., 2020; Ghiz et al., 2021).

88

There are several examples of ARs triggering ice and snow melt around Antarctica: e.g. in the Weddell Sea in 1973 and 2017 (Francis et al., 2020); off the Antarctic Peninsula in March 2015 (Bozkurt et al., 2018) and February 2022 (Gorodetskaya et al., 2023); around the Amery Ice Shelf in September 2019 (Francis et al., 2021), in West Antarctica (Francis et al., 2023); and in the Ross Sea (Fonseca et al., 2023). The recent study of Liang et al. (2023) highlights that the largest impact of ARs on sea ice is found on the marginal ice zone, where the SIE reduction may exceed 10% day<sup>-1</sup>. Reduced coastal offshore SIE may also foster a deeper penetration of the low-latitude air onto the inland ice sheet, as is the case in the March 2022 “heat wave” in East Antarctica (Wille et al., 2024a,b). While ARs themselves are relatively rare and short-lived in coastal Antarctica, with a frequency of ~3 days year<sup>-1</sup> at any given location, the warm and moist air masses they transport can make a substantial contribution to the surface mass balance (SMB) and are linked to extreme precipitation events (Massom et al., 2004; Wille et al. 2021, 2025). For example, in East Antarctica, a series of ARs delivered an estimated 44% of the total mean-annual snow accumulation to the high interior ice sheet over an 18-day period in the austral summer of 2001/2 (Massom et al., 2004), and AR-associated rainfall has exceeded 30% of the total annual precipitation (McLennan et al. 2022, 2023). These studies highlight the impacts of extreme weather events on the coupled Antarctic ocean-ice-snow-atmosphere system and stress the need to better understand the role of low-latitude air incursions on the SMB and state of both the Antarctic Ice Sheet and its surrounding sea-ice cover - and how these may change in a warming climate.

Moreover, sea ice accumulates a highly reflective (high albedo) and insulative snow cover that then strongly modulates the physical and optical properties of the ice cover while also influencing its formation and melt rates (Sturm and Massom, 2017, and references therein). Decreases in the thickness and distribution of Antarctic sea ice and its snow cover have strong

113 potential to impact low latitude weather patterns (England et al., 2020), disrupt the global surface  
114 energy balance (Riihelä et al., 2021) and amplify climate warming at high southern latitudes  
115 (Williams et al., 2023) leading to further sea ice loss that is likely to be further accelerated by  
116 poorly understood ocean ice snow atmosphere feedback mechanisms (Goosse et al., 2018).

117  
118 Here, we investigate the impact of atmospheric dynamics on variability in both ~~sea ice~~  
119 ~~thickness~~ (SIT) and snow thickness (ST) state through analysis of high-resolution *in-situ*  
120 measurements obtained by an autonomous Snow Ice Mass Balance Array (SIMBA) buoy (Jackson  
121 et al., 2013), combined with atmospheric reanalysis and modeling products. The SIMBA buoy was  
122 deployed from July to November 2022 at a coastal fast-ice site close to Mawson Station in East  
123 Antarctica (~~at~~ 67.5912°S, 62.8563°E), which will be denoted as “Khalifa SIMBA site on fast-ice  
124 off ~~the~~ Mawson Station” throughout the manuscript. This station is selected as it has amongst the  
125 highest AR frequency in the continent, also with a statistically significant positive trend in AR  
126 frequency and intensity during 1980-2020 (Wille et al., 2025). The overall aim of this study is to  
127 further our understanding of the temporal evolution of the thickness and ~~the~~ vertical structure of  
128 coastal sea ice and its snow cover ~~in~~ around East Antarctica, and over a six-month period spanning  
129 austral winter through late spring, early summer when ARs are more frequent in the region (Wille  
130 et al., 2025). The motivation is to provide new observations and process information that will aid  
131 numerical-modelling efforts to more accurately simulate the annual cycle of ~~the~~ Southern Ocean  
132 sea ice, and observed trends and variability in its distribution (and ultimately thickness; ~~etc.~~ c.f. Eayrs  
133 et al., 2019). Such an advance is crucial to helping rectify present low confidence in model  
134 projections of future climate and Antarctic sea-ice conditions, that currently diverge for different  
135 models and scenarios (Roach et al., 2020). This study is also particularly timely, given the  
136 precipitous downward trend in Antarctic sea ice extent (SIE) since 2016 (Parkinson, 2019), an  
137 extraordinary record-low annual minimum in February 2023 and a sudden departure to major sea-  
138 ice deficits through the winters of 2023 and 2024 (Reid et al., 2024). This turn of events suggests  
139 that Antarctic sea ice has abruptly shifted into a new low-extent regime (Purich and Doddridge,  
140 2023; Hobbs et al., 2024) due to complex changes in the coupled ocean-ice-snow-atmosphere  
141 system that are far from well understood. Much less well known - though no less important - are  
142 the thicknesses of the ice and its snow thickness (ST) and whether these are changing. Obtaining  
143 more accurate and complete information on the Antarctic SIT distribution and its ST and  
144 precipitation rates - and the factors and processes controlling them - is a critical high priority in  
145 climate science, particularly in light of climate variability and change (Webster et al., 2018;  
146 Meredith et al., 2021).

147  
148 Accurate knowledge of SIT, SIE and concentration is needed to estimate sea-ice volume, a field  
149 that is more sensitive to climate change than SIE and SIT alone (Liu et al., 2020) and is also directly  
150 parameterized in numerical models (Massonnet et al., 2013; Zhang, 2014; Schroeter and Sandery,  
151 2022). Current large uncertainties in these quantities prevent proper model evaluation and  
152 undermine confidence in model predictions of future Antarctic sea-ice conditions and global  
153 weather and climate (MakSYM et al. 2008, 2012). Satellite radar and laser altimeters hold the key

154 to large-scale estimation and monitoring of both SIE/SIT (e.g., Fonseca et al., 2023) and ST  
155 (Kacimi and Kwok, 2020). Kurtz and Markus (2012) used the measurements collected by the Ice,  
156 Cloud, and land Elevation Satellite (ICESat) to estimate the ice thickness around Antarctica. A  
157 comparison with ship-based observations revealed a mean difference of 0.15 m for the period  
158 2003-2008, with a typical SIT of 1-1.5 m. Kacimi and Kwok (2020), using both laser (ICESat-2)  
159 and radar (CryoSat-2) altimeter estimates for the period 01 April to 16 November 2019, found the  
160 thickest sea ice in the western Weddell Sea sector (predominantly multi-year sea ice), with a mean  
161 thickness of 2 m, and the thinnest ice around polynyas in the Ross Sea and off the Ronne Ice Shelf.  
162 Coincident use of laser and radar altimetry also enables basin-scale estimates of ST. The thickest  
163 snow was again observed in the western Weddell Sea ( $0.228 \pm 12.4$  m in May) and the coastal  
164 region of the Amundsen-Bellingshausen seas sector ( $0.314 \pm 23.1$  m in September), while the  
165 thinnest was in the Ross Sea ( $0.0735 \pm 4.30$  m in April) and the eastern Weddell Sea  
166 ( $0.0821 \pm 5.81$  m in June) (Kacimi and Kwok, 2020). These studies focused on pack ice, but a  
167 similar range of values has been estimated for the thickness of fast ice, such as off the Mawson  
168 (Li et al., 2022) and Davis (Heil, 2006) stations in East Antarctica. The SIMBA buoy provides  
169 high-resolution measurements at a given location of the vertical temperature profile through the  
170 air-snow-ice-upper ocean column, from which ST and SIT can be derived and monitored (Jackson  
171 et al., 2013). Time series of such point observations provide invaluable gap-filling information on  
172 the temporal evolution and state of the snow-sea ice system and its response to atmospheric and  
173 oceanic variability. They also provide crucial information with which to both (i1) calibrate the key  
174 satellite SIT and ST data products, and (i2) evaluate and improve numerical idealized column and  
175 weather forecasting models (Hu et al., 2023; Plante et al., 2024; Sledd et al., 2024; Wang et al.,  
176 2024a).

177 In particular, In this study, and making use of the SIMBA observations, the we here focus is on  
178 assessing the influence on the sea ice snow system of: (1) strong katabatic winds that cascade  
179 seawards off the ice sheet and promote sublimation of the sea ice and its snow cover (Elvidge et  
180 al., 2020; Francis et al., 2023); and (2) a number of more ephemeral but influential extreme  
181 atmospheric events in the form of atmospheric rivers (ARs). An AR is a narrow and highly  
182 elongated band of moisture rich air that originates in the tropics and subtropics and propagates  
183 polewards into the mid- and high latitudes (Wille et al., 2019; Gorodetskaya et al., 2020). ARs are  
184 associated with increased humidity and cloudiness, leading to an enhancement of the downward  
185 longwave radiation flux while still allowing some of the Sun's shortwave radiation to reach the  
186 surface (Djouma and Holland, 2021). The resulting increase in the surface net radiation flux gives  
187 a warming tendency and promotes surface melting (Gorodetskaya et al., 2013; Francis et al., 2020;  
188 Ghiz et al., 2021). There are several examples of ARs triggering ice and snow melt around  
189 Antarctica e.g., in the Weddell Sea in 1973 and 2017 (Francis et al., 2020); off the Antarctic  
190 Peninsula in March 2015 (Bozkurt et al., 2010) and February 2022 (Gorodetskaya et al., 2023);  
191 around the Amery Ice Shelf in September 2019 (Francis et al., 2021); in West Antarctica (Francis  
192 et al., 2023); and in the Ross Sea (Fonseca et al., 2023).

194

195 The recent study of Liang et al. (2023) highlights that the largest impact of ARs on sea ice is  
 196 found on the marginal ice zone e.g., where the sea ice extent reduction there that may exceed  
 197 10% day<sup>-1</sup>. Reduced coastal offshore SIE may also foster a deeper penetration of the low latitude  
 198 air onto the inland ice sheet, as was the case in the March 2022 “heat wave” in East Antarctica  
 199 (Wille et al., 2024a,b). While ARs themselves are relatively rare and short lived in coastal  
 200 Antarctica, with a frequency of ~3 days year<sup>-1</sup> at any given location, the warm and moist air masses  
 201 they transport can make a substantial contribution to the surface mass balance (SMB), and they  
 202 are linked to extreme precipitation events (Massom et al., 2004; Wille et al., 2021, 2025). In East  
 203 Antarctica, a series of ARs delivered an estimated 44% of the total mean annual snow  
 204 accumulation to the high interior ice sheet (in the vicinity of Dome C) over an 18-day period in  
 205 the austral summer of 2001/2 (Massom et al., 2004), and AR-associated rainfall has exceeded 30%  
 206 of the total annual precipitation (Melenkann et al., 2022, 2023). Moreover, and on Mac Robertson  
 207 Land (also in East Antarctica), which includes the Amery Ice Shelf and is the focal region of this  
 208 study, more than half of the annual precipitation has been observed to fall in the 10 days of heaviest  
 209 precipitation (Turner et al., 2019). This region also has some of the largest positive trends in AR  
 210 frequency and AR-related snowfall occurrence in the period 1980–2018. These studies highlight  
 211 the important impacts of extreme weather events on the coupled Antarctic ocean–ice–snow–  
 212 atmosphere system, and stresses the need to better understand the role of low-latitude air incursions  
 213 on the mass balance and state of both the Antarctic Ice Sheet and its surrounding sea ice cover  
 214 and how these may change in a warming climate.

215

216 Continuous monitoring since 1978 of the circum Antarctic spatial extent, concentration and  
 217 seasonality of sea ice by satellite passive microwave remote sensing (Parkinson, 2019) has  
 218 revealed major losses around the continent since 2016—not only in summer but also latterly  
 219 through winter (Reid et al., 2024) and for reasons that are not fully understood. This abrupt and  
 220 precipitous decline has been viewed as a possible regime shift in the coupled ocean–sea ice–  
 221 atmosphere system (Hobbs et al., 2024). Much less well known—though no less important—are  
 222 the thicknesses of the ice and its snow cover and whether these are changing. Obtaining more  
 223 accurate and complete information on the thickness distributions of Antarctic sea ice and its snow  
 224 cover (and precipitation rates) and the factors and processes controlling them is a critical high  
 225 priority in climate science, particularly in light of climate change (and variability) (Webster et al.,  
 226 2018; Meredith et al., 2021).

227

228 Accurate knowledge of SIT, SIE and concentration is needed to estimate sea ice volume, a field  
 229 that is more sensitive to climate change than SIE and SIT alone (Liu et al., 2020) and is also directly  
 230 parameterized in numerical models (Massonnet et al., 2013; Zhang, 2014; Schroeter and Sandery,  
 231 2022). For climate modeling, sea ice volume (modulated by ST) represents a key integrated  
 232 measure of the total salinity and freshwater fluxes to the ocean in winter and summer, respectively,  
 233 and total heat flux to the atmosphere. Current large uncertainties in these quantities prevent proper  
 234 model evaluation and undermine confidence in model predictions of future Antarctic sea ice

235 conditions and global weather and climate (Maksym et al., 2012). An analysis of 10 models in the  
236 Coupled Model Intercomparison Project Phase 5 (CMIP5) revealed that, around the outer sea ice  
237 zone, changes in sea ice volume are largely driven by dynamic (wind driven motion) processes  
238 during annual advance and thermodynamic (freeze and melt) processes during the retreat phase,  
239 while thermodynamic processes predominate deeper within the sea ice zone (Schroeter et al.,  
240 2018). However, and for the trends, both dynamic and thermodynamic processes are at play,  
241 highlighting the sensitivity of sea ice volume to changes in oceanic and atmospheric properties  
242 and circulation in response to anthropogenic forcing (Schroeter et al., 2018) and natural variability.  
243

244 In addition to SIT, reliable large scale information on the coincident ratio of snow to sea ice  
245 thickness is required to determine the distribution of “snow ice” formation around Antarctica  
246 (Maksym and Markus, 2008). By this process, and where the snow is sufficiently thick to depress  
247 the sea ice surface to below sea level, resultant flooding of the snow creates a slush layer that  
248 subsequently freezes onto the ice surface (Jeffries et al., 1998; Massom et al., 2001). In this way,  
249 snow makes a direct contribution to the sea mass balance in the freezing season – in addition to its  
250 indirect contribution as a high albedo insulative layer that moderates Antarctic sea ice formation  
251 and melt rates (Sturm and Massom, 2017). These factors further underline the need for additional  
252 more accurate information on precipitation and accumulation rates over the sea ice zone, including  
253 rainfall events (Webster et al., 2018).

254  
255 Satellite radar and laser altimeters hold the key to large scale estimation and monitoring of both  
256 SIT (e.g., Fons et al., 2023) and ST (Kacimi and Kwok, 2020). Kurtz and Markus (2012) used the  
257 measurements collected by the Ice, Cloud, and land Elevation Satellite (ICESat) to estimate the  
258 ice thickness around Antarctica. A comparison with ship based observations revealed a mean  
259 difference of 0.15 m for the period 2003–2008, with a typical SIT of 1–1.5 m. Kacimi and Kwok  
260 (2020), using both laser (ICESat 2) and radar (CryoSat 2) altimeter estimates for the period 1 April  
261 to 16 November 2019, found the thickest sea ice in the western Weddell Sea sector (predominantly  
262 multi-year sea ice), with a mean thickness of 2 m, and the thinnest ice around polynyas in the Ross  
263 Sea and off the Ronne Ice Shelf. Coincident use of laser and radar altimetry also enables basin-  
264 scale estimates of ST. The thickest snow was again observed in the western Weddell Sea  
265 ( $22.8 \pm 12.4$  cm in May) and the coastal region of the Amundsen–Bellingshausen seas sector  
266 ( $31.4 \pm 23.1$  cm in September), while the thinnest was in the Ross Sea ( $7.35 \pm 4.30$  cm in April)  
267 and the eastern Weddell Sea ( $8.21 \pm 5.81$  cm in June) (Kacimi and Kwok, 2020). The studies  
268 mentioned above focus on pack ice, but a similar range of values has been estimated for the  
269 thickness of fast ice, such as off the Mawson Station (Li et al., 2022) and off the Davis Station  
270 (Heil, 2006) in East Antarctica. Validation of these and other satellite derived estimates of SIT, ST  
271 and sea ice volume is a crucially important step towards improving their accuracy, yet remains a  
272 considerable challenge, given the lack of regionally and seasonally diverse *in situ* and near-  
273 surface observations with which to assess the satellite datasets (Kacimi and Kwok, 2020).

275 The SIMBA buoy provides high resolution measurements at a given location of the vertical  
276 temperature profile through the air snow ice upper ocean column, from which snow and ice  
277 thickness can be derived and monitored (Jackson et al., 2013). Time series of such point  
278 observations provide invaluable gap filling information on the temporal evolution and state of the  
279 snow sea ice system and its response to atmospheric and oceanic variability. They also provide  
280 crucial information with which to both (i) calibrate the key satellite SIT and ST data products and  
281 (ii) evaluate and improve numerical idealized column and weather forecasting models (Hu et al.,  
282 2023; Plante et al., 2024; Sledd et al., 2024; Wang et al., 2024).

283  
284 While there are a number of studies on *in-situ* SIT and ST measurements around Antarctica  
285 (e.g., Worby et al., 2011; Xie et al., 2011; Liao et al., 2022), the area of East Antarctica around  
286 Mawson Station, where extreme precipitation events in the form of ARs have become more  
287 frequent and intense in the recent decades (Wille et al., 2025), has not been sampled. In addition,  
288 these works do not delve deep into the processes responsible for the observed changes in SIT and  
289 ST, which is a necessary step for refining Antarctic climate projections. The objectives of this  
290 study are twofold: (i1) to identify the mechanisms behind the variability of the *in-situ* measured  
291 SIT and ST at the Mawson Station during July-November 2022, and compare the measured values  
292 with those estimated from remote sensing assets; and (i2) to perform high-resolution numerical  
293 simulations for selected periods during the measurement campaign, in particular during extreme  
294 weather events, to gain further insight into the role of atmospheric forcing on the SIT and ST. This  
295 study will therefore contribute to further our understanding on the variability of the SIT and ST in  
296 coastal Antarctica and the respective driver processes.

297  
298 This paper is structured as follows. The observational datasets and model outputs and products  
299 considered, and analysis techniques used, are described in Section 2. The measurements of SIT  
300 and ST, including their variability and the mechanisms behind them, are discussed in Section 3.  
301 Section 4 provides a case-study analysis of the period 11-16 JulyNovember 2022, while in Section  
302 5 the main findings of the work are outlined and discussed.

## 303 2. Methodology & Diagnostics

304 In this section, the datasets, numerical model, and diagnostics used in this study are described.

### 305 2.1. In-Situ Measurements at Khalifa SIMBA site off the Mawson Station

306 *In-situ* measurements of SIT and ST are obtained using a sea-ice mass-balance (SIMBA) unit  
307 (Jackson et al., 2013). This SIMBA was deployed on landfast ice offshore from Mawson Station  
308 at 67.5912°S, 62.8563°E (Fig. 1c) on 07 July 2022, and remained *in-situ* until 07 December 2022.  
309 The SIMBA unit consists of a 5 m-long thermistor string with a 0.02 m sensor spacing, a  
310 barometer for surface air pressure, and an external sensor for near-surface ambient air temperature  
311 (Jackson et al., 2013). During deployment, manual measurements of SIT and ST, as well as

312 freeboard, were recorded. The positions of the sensors relative to the interfaces were noted to  
 313 establish the initial state (on 07 July 2022). The measured SIT upon deployment was 0.988 m, the  
 314 ST on top of the sea ice was 0.156 m, and the sea-ice freeboard was 0.046 m. No manual validation  
 315 or calibration is conducted during the measurement period of 07 July - 07 December 2022.

316

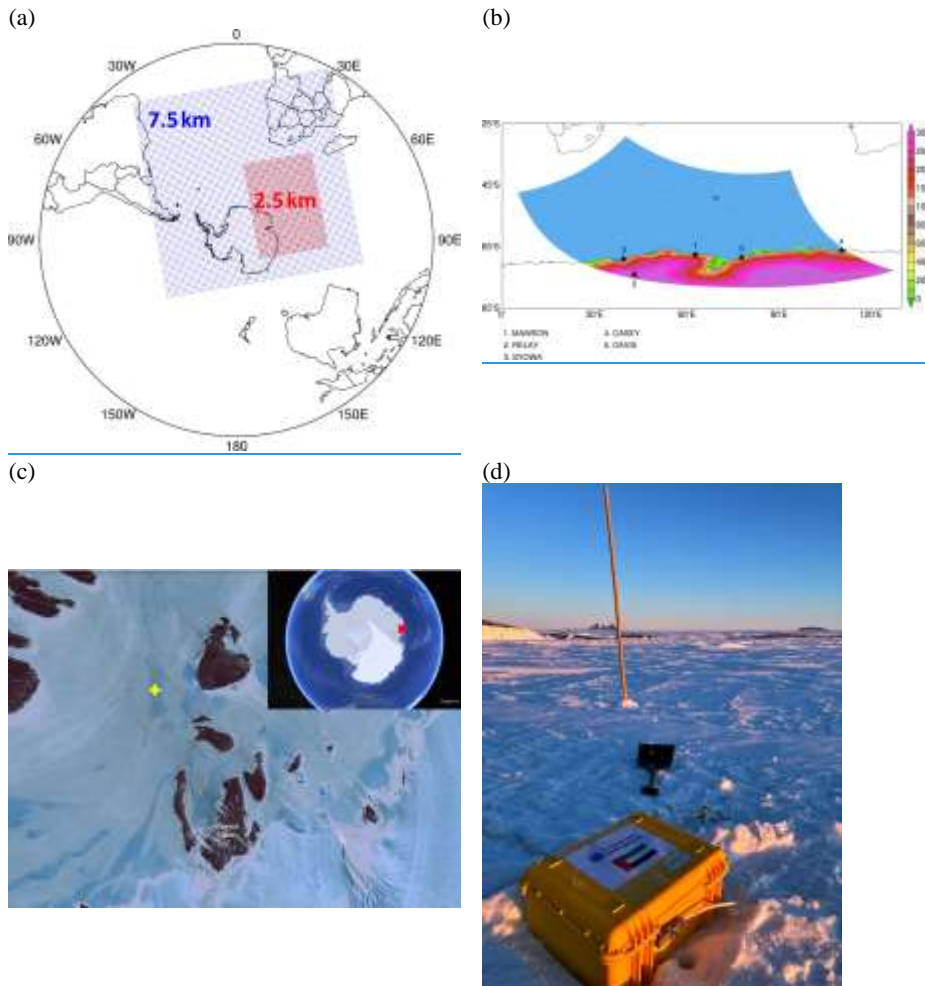


**Figure 1: PolarWRF Simulation:** (a) Spatial extent of the 7.5 km (blue) and 2.5 km (red) PWRF grids used in the numerical simulations. (b) Spatial extent and orography (m) of the 2.5 km PWRF grid. The stars highlight the location of the five weather stations considered in this work. Zoom in view around East Antarctica for the 2.5 km grid, with the location of the Mawson, Relay, Mizuho and Syowa weather stations highlighted by the stars. The shading gives the orography (m) as seen by the model. (c) SIMBA

deployment site (yellow cross) on the fast ice about 1.8 km off Mawson Station. Image source: Landsat 8 acquired on 19 November 2022. The red cross in the inset image, taken from Google Earth Pro, shows where ~~the~~ Mawson Station is located in Antarctica. (d) SIMBA instrument prior to deployment. Image credit: Peter Caithness.

317

318

319 The accuracy of the bus-addressable digital temperature sensing integrated circuit is  $\pm 0.0625$  K. A  
320 resistor is mounted directly underneath each thermistor sensor. A low voltage power supply (8 V)  
321 is connected to each sensor, to gently heat the sensor and its immediate surroundings. In this study,  
322 heating is applied to the sensor chain for durations of 30 s and 120 s once per day, with four vertical  
323 temperature profiles without heating also recorded daily. In this study, SIMBA data from 08 July  
324 to 30 November 2022 ~~is~~ are used to assess the evolution of SIT and ST at the site. The  
325 measurements are shown in Fig. 2. For the sensors 6 through 126, the actual temperature and the  
326 temperature rise after 120 s heating are given in Fig. 2a and 2b, respectively, with Fig. 2c showing  
327 the difference between the measurements of two adjacent temperature sensors after applying the  
328 heating.

329

330 The vertical temperature gradients in the air above the surface and in the water below the ice  
331 bottom are generally very small (Jackson et al., 2013; Hoppmann et al., 2015; Liao et al., 2018).  
332 After 120 s of heating, the rise in temperature is approximately 10 times higher in air than ~~it is~~ in  
333 ice and water (Jackson et al., 2013). For any two adjacent sensors in the ice, and following the  
334 algorithm detailed in Liao et al. (2018) based on a physical model applied to the SIMBA  
335 measurements, the temperature difference should be  $\leq 0.1875$  K, whereas for two adjacent sensors  
336 in snow, the temperature difference should be  $\geq 0.4375$  K. These thresholds are applied to the  
337 temperature differences between adjacent sensors in the heating profile to identify the air-snow  
338 and snow-ice interfaces (Jackson et al., 2013; Hoppmann et al., 2015; Liao et al., 2018). The ice-  
339 water interface is identified using a statistical approach based on Liao et al. (2018). A section of  
340 the thermistor string, spanning from the top of the sea ice to a few sensors below the water, is  
341 selected. The seawater temperature near the ice bottom remains stable around the freezing point  
342 ( $T_f$ ). The temperature readings from this section are analyzed as a time series, and the most frequent  
343 value is identified as  $T_f$ . Scanning from bottom up, the last sensor close to  $T_f$  is identified as the  
344 ice bottom. The allowed temperature difference is 1.5 times the thermistor resolution of 0.0625 K.  
345 The temporal evolutions of the three interface locations are plotted in Figs. 2a-c.

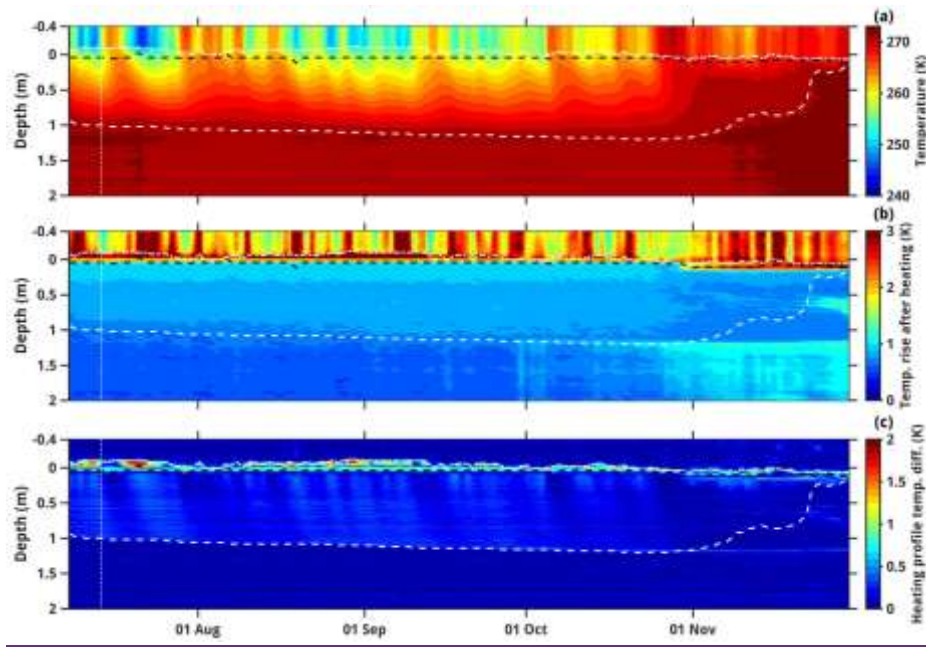


**Figure 2: SIMBA measurements:** (a) Temperature (K) evolution from the top of the chain through the ice down into the water (the zero line on the y-axis is at the snow-ice interface). (b) Temperature rise (K) after heating for 120 s. (c) Temperature difference (K) between adjacent sensors after applying the heating for 120 s. The vertical white dotted lines indicate the days of AR occurrence at the site (14 July, according to Lapere et al. (2024)). The horizontal dotted white line, black dashed line, and white dashed line indicate the air-snow (AS), snow-ice (SI), and ice-water (IW) interfaces, respectively.

346

347

## 2.2. Observational and Reanalysis Datasets

348 In addition to *in-situ* SIT and ST measurements, three observational datasets are  
 349 considered in this work: (i) satellite-derived SIE and sea-ice velocity; (ii) daily true colour visible  
 350 satellite images available at the National Aeronautics and Space Administration's (NASA's)  
 351 WorldView website (Boller, 2024); (iii) ground-based observations at five weather stations  
 352 located in the target region (Fig. 1b), namely at Mawson, Syowa, Relay, Mizuho, Casey, and  
 353 Davis Relay stations (Fig. 1b); and (iv) twice daily sounding profiles at the Mawson, Syowa,  
 354 Casey, and Davis stations (stations #1 and 3-5 in Fig. 1b) (Oolman, 2024). The Data from the fifth  
 355 generation of the European Centre for Medium Range Weather Forecasting reanalysis (ERA-5);

356 [reanalysis data](#) (Hersbach et al., 2020) [is](#) used to investigate the large-scale circulation and SMB  
357 during the study period. ERA-5 is regarded as one of the best reanalysis products currently  
358 available over Antarctica and the Southern Ocean (Gossart et al., 2019; Dong et al., 2020). All of  
359 these products are listed in Table 1.

<u>Dataset</u>	<u>Specifications</u>
<a href="#">In-situ Sea-Ice Thickness and Snow Thickness</a>	SIT and ST measurements just offshore of the Mawson Station (67.5912°S, 62.8563°E) using a SIMBA unit; data available from 07 July to 07 December 2022
<a href="#">Sea-Ice Extent</a>	Satellite-derived daily sea-ice extent SIE at 3.125 km resolution; data available from June 2002 - Present
<a href="#">Sea-Ice Velocity</a>	Satellite-derived daily sea-ice velocity at 62.5 km resolution; data available from December 2009 - Present
<a href="#">Weather Station Data</a>	Ground-based observations at Mawson (67.6017°S, 62.8753°E; January 1954 - Present), Relay (74.017°S, 43.062°E; November 2021 - Present), Syowa (69.0053°S, 39.5811°E; January 1994 - Present), Casey (66.2825°S, 110.5231°E; February 1989 - Present), and Davis (68.5744°S, 77.9672°E; January 1957 - Present) Stations
<a href="#">Sounding Profiles</a>	Twice daily at Mawson (67.6017°S, 62.8753°E; January 1954 - Present), Syowa (69.0053°S, 39.5811°E; January 2021 - Present), Casey (66.2825°S, 110.5231°E; February 1989 - Present), and Davis (68.5744°S, 77.9672°E; January 1957 - Present) Stations
<a href="#">ERA-5 reanalysis</a>	Hourly products at $0.25^\circ \times 0.25^\circ$ (~27 km) spatial resolution; available from January 1940 - Present

361  
362 **Table 1: Observational and Reanalysis Datasets:** List of observational and reanalysis datasets used in  
363 this study.

364  
365 Daily SIE data are available at a resolution of 3.125 km and on a daily basis for the period June  
366 2002 to present. It is estimated [is derived](#) from the measurements of sea-ice concentration collected  
367 by the Advanced Microwave Scanning Radiometer [for Earth Observing Systems](#) (AMSR-E) -  
368 [Earth Observing Systems](#) onboard [the National Aeronautics and Space Administration's](#) (NASA's)  
369 [Aqua](#) satellite from June 2002 to October 2011, and from the observations taken by the  
370 AMSR2 onboard Japan Aerospace and Exploration Agency's Global Change Observation Mission  
371 - Water (GCOM-W; "Shizuka") satellite from July 2012 to present (Spreen et al., 2008). Sea-ice  
372 velocity vectors [on the other hand](#), are [available also daily at 62.5 km spatial resolution](#). This  
373 product [is](#) obtained from the measurements collected by the Special Sensor Microwave

374 Imager/Sounder onboard the United States Air Force Defense Meteorological Satellite Program,  
375 the Advanced Scatterometer onboard the European Space Agency's Meteorological Operational  
376 ~~Satellite~~, and the ~~AMSR2 onboard the GCOM-W AMSR2 satellite, and is available from~~  
377 ~~December 2009 to present~~ (Lavergne et al., 2010). ~~Warm and moist air intrusions impacting~~  
378 ~~Antarctica can have substantial changes in SIE, with considerable sea ice drift velocities that can~~  
379 ~~exceed 50 km day<sup>-1</sup> (e.g., Francis et al., 2021; Fonseca et al., 2023)~~. ~~Given this, B~~oth the SIE and  
380 sea-ice velocity products are used to gain insight into the effects of the warm and moist air  
381 intrusions on the sea-ice state around ~~the~~ Mawson Station, ~~during the measurements as performed~~  
382 ~~in previous studies for other parts of Antarctica (e.g., Francis et al., 2021; Fonseca et al., 2023)~~.  
383 ~~Moderate Resolution Imaging Spectroradiometer (MODIS; (Xiong et al., 2006; Gumley et al.,~~  
384 ~~2010) satellite~~ true colour visible images are used to obtain additional high resolution information  
385 ~~on the SIE and its spatial variability (in the absence of clouds) including~~ (this is only possible in  
386 ~~the absence of clouds, as otherwise the sea ice and other features near sea level will not be visible~~).  
387 ~~They also provided information on the presence of polynyas and the fine structure within the ice~~  
388 ~~pack, as the spatial resolution is no lower than 1 km~~.  
389

390 *In-situ* observations at multiple Automatic Weather Stations (AWSs) are used in the analysis  
391 and model evaluation (Fig. 1b). These include: (i) 1-minute 2-m air temperature and humidity, 10-  
392 m horizontal wind velocity, and sea-level pressure (SLP) observations ~~at~~ from the ~~Australian~~  
393 ~~Antarctic stations of Mawson, Casey, and Davis Stations (67.6017°S, 62.8753°E)~~; (ii) 1-minute  
394 measurements of meteorological parameters (2-m air temperature, SLP, 10-m horizontal wind  
395 velocity, and 2-m relative humidity) and radiation fluxes (surface upward and downward and  
396 shortwave and longwave) at the coastal Syowa Station ~~(69.0053°S, 39.5811°E)~~; and (iii) 10-  
397 minute SLP, ~~and~~ horizontal wind velocity, and 2-m air temperature and relative humidity  
398 observations at the inland Mizuho Station ~~(70.70°S, 44.29°E)~~ and Relay Station ~~(74.017°S,~~  
399 ~~43.062°E~~). Also analyzed ~~awere~~ data from atmospheric sounding profiles acquired twice daily (at  
400 00 and 12 UTC) at ~~the~~ Mawson, Syowa, ~~Casey, and Davis S~~tations.  
401

402 ~~In addition, the fifth generation of the European Centre for Medium Range Weather~~  
403 ~~Forecasting reanalysis (ERA 5) dataset (Hersbach et al., 2020) is used to investigate the large~~  
404 ~~scale atmospheric circulation during the measurements and to analyze the surface energy budget~~  
405 ~~for the case study (11–16 July November 2022). At a spatial resolution of 0.25° × 0.25° (~27 km)~~  
406 ~~and an hourly temporal resolution from 1940 to present, ERA 5 is regarded as one of the best~~  
407 ~~reanalysis products currently available over Antarctica and the Southern Ocean (Gossart et al.,~~  
408 ~~2019; Dong et al., 2020).~~

### 409 2.3. Numerical Models

410 Here we use version 4.3.3 of the Polar WRF (Weather Research and Forecasting) model, a  
411 version of the WRF model (Skamarock et al., 2019) optimized for the polar regions (Bromwich et  
412 al., 2013; Hines et al., 2021; Xue et al., 2022; Zou et al., 2023), to simulate and investigate the AR

413 that impacted the Mac Robertson Land region on 14 JulyNovember 2022. The model is run in a  
414 nested configuration, with a 7.5 km horizontal resolution grid domain comprising Antarctica, the  
415 Southern Atlantic Ocean, southern Africa and the southwestern Indian Ocean, and a 2.5 km  
416 horizontal resolution grid domain extending from the Southern Ocean just south of South Africa  
417 around 30°E into coastal East Antarctica all the way to around as far east as approximately  
418 120°Earound the Mawson Station (Fig. 1a). The choice of resolution, in particular the 2.5 km grid  
419 that covers the bulk of the AR and associated warm and moist air intrusion into East Antarctica,  
420 reflects the findings of Box et al. (2023) and Francis et al. (2024). These studies stressed the need  
421 to properly resolve the fine-scale structure of an AR due to the possible presence of AR rapid-like  
422 features embedded in the convective region, which can generate copious amounts of precipitation  
423 and hence have a substantial impact on the SMB of the ice. AR rapids are narrow (5-15 km wide),  
424 elongated (100-200 km long) and shallow ( $\sim$ 3 km deep) linear features within the AR that  
425 propagate at high speed ( $>30 \text{ m s}^{-1}$ ) and last for more than 24 h. They have been reported for an AR  
426 that impacted Greenland in September 2017 (Box et al., 2023) and another that wreaked havoc in  
427 the Middle East in April 2023 (Francis et al., 2024). AR rapids are distinct from mesoscale  
428 convective systems (MCSs; Houze, 2004; Feng et al., 2021; Nelli et al., 2021), which propagate  
429 at a slower speed (10-20  $\text{m s}^{-1}$ ), typically do not last as long (6-10 h), and generate broader (as  
430 opposed to linear) precipitation structures.

431  
432 The physics schemes selected, listed in Table 2, reflect the optimal model configuration for  
433 Antarctica and the Southern Ocean (Zou et al. 2021a, 2021b, 2023); the two moment Morrison-  
434 Milbrandt P3 cloud microphysics scheme (Morrison and Milbrandt, 2015), with the Vignon  
435 adjustment to improve the simulation of mid level mixed phase clouds over the Southern Ocean  
436 (Hines et al., 2021; Vignon et al., 2021); the Mellor Yamada Nakanishi Niino (MYNN) level 1.5  
437 planetary boundary layer (PBL) scheme (Nakanishi and Niino, 2006); the Rapid Radiative  
438 Transfer Model for Global Circulation Models (RRTMG; Iacono et al., 2008) for shortwave and  
439 longwave radiation; the Noah Land Surface Model (Chen and Dudhia, 2001; Tewari et al., 2004);  
440 the Kain Fritsch cumulus scheme (Kain, 1994) with subgrid scale cloud feedbacks to radiation  
441 (Alapaty et al., 2012), switched on in the 7.5 km grid only; and the Zeng and Beljaars (2005)  
442 surface skin temperature scheme. PWRF is run from 10 JulyNovember 2022 at 00 UTC to 17  
443 JulyNovember 2022 at 00 UTC, comprising the only strongest AR that impacted the site during  
444 July-November 2022, with the first day regarded as spin-up and the output discarded. The hourly  
445 outputs of the 7.5 km and 2.5 km grids are used for analysis. PWRF is driven by 6 hourly ERA-5  
446 data, with the reanalysis' fractional SIE and ice concentration ingested into the model. The physics  
447 schemes selected, listed in Table 2, reflect the optimal model configuration for Antarctica and the  
448 Southern Ocean (Zou et al. 2021a, 2021b, 2023). In order to prevent the large-scales in the model  
449 from drifting from the forcing fields, spectral nudging (Attada et al., 2021) is employed in both  
450 grids for spatial scales  $\gtrsim$  1,000 km above  $\sim$ 800 hPa and excluding the boundary layer. Fields  
451 nudged include the horizontal wind components, the potential temperature perturbation, and the  
452 geopotential height. In the vertical, 60 levels are considered, with the lowest level above the surface

453 at ~27 m and roughly 20 levels in the range of ~1-6 km. The higher resolution in the low- to mid-  
454 troposphere is crucial to correctly representing the fine-scale variability of the warm and moist air  
455 masses impacting the site, and associated cloud processes (Rauber et al., 2020; Finlon et al., 2020).  
456

Physics Scheme	Option Selected
<a href="#">Cloud Microphysics</a>	<a href="#">Two-moment Morrison-Milbrandt P3 (Morrison and Milbrandt, 2015), with Vignon adjustment to improve the simulation of mid-level mixed-phase clouds over the Southern Ocean (Hines et al., 2021; Vignon et al., 2021)</a>
<a href="#">Planetary Boundary Layer</a>	<a href="#">Mellor-Yamada-Nakanishi-Niino level 1.5 (MYNN; Nakanishi and Niino, 2006)</a>
<a href="#">Radiation</a>	<a href="#">Rapid Radiative Transfer Model for Global Circulation Models (Iacono et al., 2008) for shortwave and longwave radiation</a>
<a href="#">Cumulus</a>	<a href="#">Kain-Fritsch (Kain, 2004) with subgrid-scale cloud feedbacks to radiation (Alapaty et al., 2012) only in 7.5 km grid</a>
<a href="#">Land Surface Model (LSM)</a>	<a href="#">Noah LSM (Chen and Dudhia, 2001; Tewari et al., 2004)</a>
<a href="#">Sea Surface Temperature (SST)</a>	<a href="#">6-hourly ERA-5 SSTs + Zeng and Beljaars (2005) surface skin temperature scheme</a>

457  
458 **Table 2: WRF Experimental Setup:** Physics scheme used in the WRF simulation.  
459

460 [PWRF is driven by 6-h ERA-5 data, with the SSTs and SIE used in the simulations taken from](#)  
461 [ERA-5. Due to the lack of availability of SIT in ERA-5, the model's default SIT value of 3 m is](#)  
462 [used in all sea-ice covered grid-boxes in the PWRF simulations. The sea-ice albedo is](#)  
463 [parameterized as a function of air and skin temperature following Mills \(2011\), with the model](#)  
464 [explicitly predicting ST on sea ice. A sensitivity experiment is performed in which a more realistic](#)  
465 [representation of SIE and SIT is considered. In particular, satellite-derived values are used for SIE,](#)  
466 [extracted from the 3.125 km-resolution daily product available at the University of Bremen](#)  
467 [website \(UoB, 2024\), while the SIT estimates at Mawson are employed at all sea-ice covered](#)  
468 [pixels. A similar model performance is obtained with respect to the \*in-situ\* observations \(not](#)  
469 [shown\). Therefore, and for consistency with the atmospheric forcing, the ERA-5's SIE and the](#)  
470 [PWRF's default SIT values are used in the model runs. This configuration is denoted as control](#)  
471 [simulation \("PWRF"\). Given the order of magnitude difference between the spatial resolution of](#)  
472 [the innermost model grid \(2.5 km\) and that of ERA-5 \(~27 km\), and how important a realistic](#)  
473 [representation of the sea ice may be in the model forecasts, an additional simulation is performed](#)  
474 [in which satellite derived values are used for SIE, while the SIT estimates at Mawson are employed](#)

475 at all sea ice covered pixels. This run is denoted as “PWRF\_SIE\_SIT” throughout the manuscript.  
476 The SIE is extracted from is repeated using as sea ice concentration boundary conditions for the  
477 full 7.5 km and 2.5 km PWRF domains the 3.125 km resolution daily product available at the  
478 University of Bremen website (UoB, 2024). For the SIT, and to contrast with the excessively thick  
479 3 m default value used in the control run, the range of values measured *in situ* at the Khalifa  
480 SIMBA site on fast ice off the Mawson Station towards the end of November, which is about 0.18  
481 m to 0.30 m (Fig. 3a), is ingested into the model at all sea ice covered grid boxes. This simulation  
482 will be denoted as “PWRF\_SIE\_SIT” throughout the manuscript. Satellite derived measurements  
483 suggest an overall similar range of values for the thickness of pack ice and fast ice at multiple sites  
484 around Antarctica (Heil, 2006; Kacimi and Kwok, 2020; Li et al., 2022), justifying the usage of  
485 the same value for all sea ice pixels in the model domain.

486  
487 In order to prevent the large scales in the model from drifting from the ERA-5 forcing fields,  
488 spectral nudging (Attada et al., 2021) is employed in both grids for spatial scales  $\geq 1,000$  km above  
489  $\sim 800$  hPa and excluding the boundary layer. Fields nudged include the horizontal wind  
490 components, the potential temperature perturbation, and the geopotential height. In the vertical, 60  
491 levels are considered, with the lowest level above the surface at  $\sim 27$  m and roughly 20 levels in  
492 the range of  $\sim 1.6$  km. The higher resolution in the low to mid troposphere is crucial to correctly  
493 representing the fine scale variability of the warm and moist air masses impacting the site, and  
494 associated cloud processes (Rauber et al., 2020; Finlon et al., 2020).

495  
496 The moisture sources that contributed to the AR during 11-16 July November 2022 are  
497 diagnosed based on 96-h back-trajectories obtained with the Hybrid Single-Particle Lagrangian  
498 Integrated Trajectory (HYSPLIT; Stein et al., 2015) model driven by ERA-5 reanalysis data.

#### 499 2.4. Diagnostics and Metrics

500 The performance of the PWRF model is assessed with the verification diagnostics proposed  
501 by Koh et al. (2012) outlined in Supplement Section S1. In addition to the model bias, the two key  
502 skill scores are (i) the normalized bias  $\mu$ , defined as the ratio of the bias to the standard  
503 deviation of the discrepancy between the model forecasts and observations; and (2ii) the  
504 normalized error variance  $\alpha$ , which accounts for both phase and amplitude errors. When  $|\mu| < 0.5$   
505 the model biases can be regarded as not significant, while when  $\alpha < 1$ , the model forecasts are  
506 deemed as to be practically useful, defined in Equations (1) to (5) below. These diagnostics are the  
507 (i) bias,  $B$ , given by the mean discrepancy between the model forecasts,  $F$ , and the observations,  
508  $O$ ; (ii) normalized bias,  $\mu$ , defined as the ratio of the bias to the standard deviation of the  
509 discrepancy  $B$  between  $F$  and  $O$  (following Koh et al. (2012), if  $|\mu| < 0.5$ , the bias makes a smaller  
510 contribution to the Root Mean Square Error than the error variance and can therefore be  
511 regarded as not significant); (iii) correlation,  $\rho$ , which measures the phase agreement between the  
512 modelled and observed data; (iv) variance similarity,  $\eta$ , an indication of the amplitude agreement  
513 between the two signals; and (v) normalized error variance,  $\alpha$ , a diagnostic that combines phase

514 and amplitude errors. For a random forecast based on the climatological mean and variance  $\alpha = 1$ ,  
 515 the model predictions can be deemed as practically useful if  $\alpha < 1$ . The  $\rho$ ,  $\eta$  and  $\alpha$  skill scores are  
 516 non-dimensional, symmetrical with respect to observations and forecasts, and applicable to scalar  
 517 and vector fields – meaning that the model performance for scalars such as air temperature and  
 518 vector quantities such as the wind vector can be directly compared. The verification diagnostics  
 519 are:

$$B = F - O \quad (1)$$

$$\mu = \frac{\langle B \rangle}{\sigma_B} \quad (2)$$

$$\rho = \frac{1}{\sigma_O \sigma_F} \langle (F - \mu_F) - (O - \mu_O) \rangle; -1 \leq \rho \leq 1 \quad (3)$$

$$\eta = \frac{\sigma_O \sigma_F}{\sqrt{2}(\sigma_O^2 + \sigma_F^2)}; 0 \leq \eta \leq 1 \quad (4)$$

$$\alpha = 1 - \rho \eta = \frac{\sigma_B^2}{\sigma_O^2 + \sigma_F^2}; 0 \leq \alpha \leq 2 \quad (5)$$

530 ARs are identified based on the meridional Integrated Vapour Transport (IVT;  $\text{kg m}^{-1} \text{s}^{-1}$ ),  
 531 which is the column integral of the water-vapour flux advected by the horizontalmeridional wind.  
 532 This quantity is more appropriate for AR detection if the focus is on snowfall, which is the case  
 533 here, whereas for surface melting IVT is a better metric (Wille et al., 2019). It is quantified as:

$$vIVT = \frac{1}{g} \int_{1000 \text{ hPa}}^{200 \text{ hPa}} qv dp \quad (6)$$

$$IVT = \sqrt{\left( \frac{1}{g} \int_{1000 \text{ hPa}}^{200 \text{ hPa}} qu dp \right)^2 + \left( \frac{1}{g} \int_{1000 \text{ hPa}}^{200 \text{ hPa}} qv dp \right)^2} \quad (1)$$

535 In equation (16), where  $g$  is the gravitational acceleration ( $9.80665 \text{ m s}^{-2}$ ),  $q$  is the specific humidity  
 536 ( $\text{kg kg}^{-1}$ ),  $u$  is the zonal wind speed ( $\text{m s}^{-1}$ ),  $v$  is the meridional wind speed ( $\text{m s}^{-1}$ ), and  $dp$  is the  
 537 pressure difference between adjacent vertical levels (hPa). The criteria of Wille et al. (2021)  
 538 applied to ERA-5 data is are used here to identify ARs. In particular, IVT has to exceed The AR  
 539 outer boundaries are taken from Lapere et al. (2024), who used the 3-hourly 987<sup>th</sup> percentile  
 540 extracted for 1979-2022 at a given grid-box, of vIVT at a given grid box and a minimum latitudinal  
 541 extent of  $20^\circ$  is required for the feature to be considered ant to identify ARs, from the Modern Era  
 542 Retrospective Analysis for Research and Applications Version 2 dataset (MERRA-2; Gelaro et al.,  
 543 2017). The ARs in that study were extracted globally for the period 1980–2022, with the respective  
 544 outlines made publicly available. The ARs for July–November 2022 are considered in this work.  
 545 During the July to November 2022 study period, the Khalifa SIMBA site on fast-ice off the  
 546 Mawson Station was affected by one three ARs: on 14 July, 04–05 October, 07 October, 13 August  
 547 and 14 November. The IVT and vIVT values around the Mawson Station, in particular the area-

550 averaged values in a  $120^\circ \times 120^\circ$  domain centred around the station and obtained with MERRA-2  
551 data to be consistent with the AR outlines, are highest for the 14 July November AR. For this case,  
552 the maximum absolute IVT and vIVT values are  $15161 \text{ kg m}^{-1} \text{ s}^{-1}$  and  $78112 \text{ kg m}^{-1} \text{ s}^{-1}$ , respectively,  
553 compared to  $8587 \text{ kg m}^{-1} \text{ s}^{-1}$  and  $4639 \text{ kg m}^{-1} \text{ s}^{-1}$  for the 04–05 13 October August AR,  $48 \text{ kg m}^{-1} \text{ s}^{-1}$   
554 and  $36 \text{ kg m}^{-1} \text{ s}^{-1}$  for 07 October AR, and  $71148 \text{ kg m}^{-1} \text{ s}^{-1}$  and  $4382 \text{ kg m}^{-1} \text{ s}^{-1}$  for the 14  
555 November July AR. Based on these findings, the 14 July November This event is selected for more  
556 in-depth analysis and modeling in Section 4. Large-scale circulation patterns that favour ARs,  
557 including the presence of blocking and interaction with tropopause polar vortices (TPVs), are also  
558 explored. Further details regarding the metrics used to diagnose them are given in Supplementary  
559 Sections S2–S3. Except for IVT and vIVT, for which MERRA-2 data are used as noted above,  
560 ERA-5 data are used to extract the other diagnostics outlined below.

561  
562 For ARs to reach Antarctica, a large scale circulation pattern that promotes the advection of  
563 warm and moist low latitude air masses into the continent must be present. The leading mode of  
564 variability in the Southern Hemisphere extratropical atmospheric flow is the Southern Annular  
565 Mode (SAM; Marshall, 2003). This metric is based on the difference in mean sea level pressure  
566 averaged over six stations at about  $40^\circ\text{S}$  and six stations at about  $65^\circ\text{S}$ , which are deemed  
567 representative of the zonal flow at the two latitudes. A positive index value indicates a stronger  
568 westerly flow in the Southern Hemisphere mid latitudes, while a negative SAM phase is  
569 accompanied by an increase in blocking frequency (Oliveira et al., 2013). Atmospheric blocking  
570 promotes the development and propagation of ARs (Massom et al., 2004; Francis et al., 2021,  
571 2022a; Wille et al., 2024). In this study, it is quantified using the blocking index ( $BI$ ) proposed by  
572 Pook et al. (2013) and optimized over Antarctica by Wille et al. (2024e):

$$573 \quad BI = 0.5 (U_{35} + U_{40} + U_{65} + U_{70} - U_{50} - U_{60} - 2U_{55}) \quad (7)$$

574 where  $U_X$  is the geostrophic zonal wind computed from the 5 day running mean (in order to  
575 exclude temporary features) of the 500 hPa geopotential height at latitude  $X^\circ\text{S}$ . Mid-latitude  
576 blocking events correspond therefore to higher values of  $BI$ , with values in excess of  $40 \text{ m s}^{-1}$   
577 indicating a high degree of blocking.

578  
579 The AR investigated in Section 4 originated over southern Africa, where tropical–temperate  
580 troughs (TTTs), which arise from the interaction of mid-latitude baroclinic weather systems and  
581 tropical convection (Hart et al., 2013), are a regular occurrence. In order to assess whether a TTT  
582 event took place during the study period, we use the TTT index proposed by Ratna et al. (2023),  
583 which is based on Outgoing Longwave Radiation ( $OLR$ ) and meridional wind speed as defined in  
584 equations (8a) and (8b), respectively:

$$585 \quad OLR = \{[(OLR_{E1} + OLR_{E2})/2] \times 0.4 - [(OLR_{W1} + OLR_{W2})/2] \times 0.6\} \quad (8a)$$

591 In Equation (8a), E1 and E2 correspond to regions over Madagascar and southeastern Africa (E1: 592  $37^{\circ} 42^{\circ}$ E,  $12^{\circ} 17^{\circ}$ S; E2:  $45^{\circ} 50^{\circ}$ E,  $23^{\circ} 15^{\circ}$ S), with W1 and W2 located to the southwest of E1 and 593 E2, the former over South Africa and the latter just offshore (W1:  $22^{\circ} 32^{\circ}$ E,  $24^{\circ} 18^{\circ}$ S; W2:  $32^{\circ} 594$   $42^{\circ}$ E,  $36^{\circ} 28^{\circ}$ S). In a TTT event, there are higher values of OLR ahead of the trough (E1 and E2) 595 and lower values in the region where the trough is typically located (W1 and W2), with the 596 placement of E1-E2 and W1-W2 reflecting the southeast northwest orientation of the trough. The 597 0.4 and 0.6 factors in equation (8a) are indicative of the regional strength of the anomalies between 598 the east and west regions, with the latter generally stronger than the former. The associated 599 meridional wind index is defined as:

600  $WIND = V_W - V_E$  (8b)

601 The 850 hPa meridional wind speed is averaged over the western region ( $0^{\circ} 15^{\circ}$ E,  $38^{\circ}$ S  $27^{\circ}$ S) to 602 the southwest of South Africa, and the eastern region ( $34^{\circ} 46^{\circ}$ E,  $38^{\circ} 27^{\circ}$ S) to the southeast of South 603 Africa. If a trough is present, the associated clockwise circulation will lead to southerly winds to 604 its west and northerly winds to its east, giving a positive value of the wind index. A TTT event 605 requires the OLR and wind indices computed using the area averaged anomalies to exceed their 606 climatological standard deviations by 1.5 and 0.5, respectively.

607 Besides blocking and TTTs, the poleward transport of warm and moist low latitude air is linked 608 to the strength of the attendant cyclone, which is itself modulated by the presence of tropopause 609 polar vortices (TPVs). As detailed in Wille et al. (2024c), TPVs are characterized by a minimum 610 in potential temperature and a maximum in potential vorticity at the dynamic tropopause (PV =  $2$  611  $\times 10^{-6} \text{ m}^2 \text{ K s}^{-1} \text{ kg}^{-1}$  =  $2$  PV Units =  $2$  PVU in the Northern Hemisphere and  $2$  PVU in the Southern 612 Hemisphere). When co-located with increased low level baroclinicity, they can trigger 613 cyclogenesis, with a deeper low promoting an enhanced poleward propagation of the warm and 614 moist low latitude air mass. The TPVs are identified using the TPVTrack (v1.0) software described 615 in Szapiro and Cavallo (2018), here driven by ERA-5 data.

616 The extratropical circulation can be modulated by tropical forcing, such as thermal (heating 617 and cooling) anomalies (Hoskins and Karoly, 1981; Hoskins et al., 2012). In order to explore 618 whether this occurs during the case study, the stationary wave activity flux that indicates the 619 direction of the anomalous stationary Rossby wave propagation, defined in Takaya and Nakamura 620 (2001), is derived in equations (2a-b), is derived (and and plotted) as:

621 
$$W_X = \frac{p \cos(\phi)}{2|u\psi|} \left\{ \frac{u\psi}{a^2 \cos(\phi)^2} \left[ \left( \frac{\partial \psi'}{\partial \lambda} \right)^2 - \psi' \frac{\partial^2 \psi'}{\partial \lambda^2} \right] + \frac{v\psi}{a^2 \cos(\phi)} \left[ \frac{\partial \psi'}{\partial \lambda} \frac{\partial \psi'}{\partial \phi} - \psi' \frac{\partial^2 \psi'}{\partial \lambda \partial \phi} \right] \right\} \quad (2a) \text{ and}$$

622 
$$W_Y = \frac{p \cos(\phi)}{2|u\psi|} \left\{ \frac{u\psi}{a^2 \cos(\phi)} \left[ \frac{\partial \psi'}{\partial \lambda} \frac{\partial \psi'}{\partial \phi} - \psi' \frac{\partial^2 \psi'}{\partial \lambda \partial \phi} \right] + \frac{v\psi}{a^2} \left[ \left( \frac{\partial \psi'}{\partial \phi} \right)^2 - \psi' \frac{\partial^2 \psi'}{\partial \phi^2} \right] \right\} \quad (2b)$$

628 In equations (2a-b), where  $p$  is the ratio of the pressure level at which the W-vector is computed  
629 and 1000 hPa,  $\phi$  is the latitude,  $\lambda$  is the longitude,  $U$  and  $V$  are the zonal and meridional  
630 climatological wind speeds, respectively,  $|U|$  is the climatological mean wind speed, and  $\psi'$  is the  
631 streamfunction anomaly.

632  
633 Variability in the ST, and perhaps to a lesser extent the SIT, is directly related to by the surface  
634 mass balance (SMB), which can be expressed as

635 
$$SMB = P - Q_{sfc} - M - Q_{snow} - D \quad (3)$$

636 where  $P$  is the precipitation rate (mostly snowfall mm w.e. day<sup>-1</sup>),  $Q_{sfc}$  is the surface  
637 evaporation/sublimation rate,  $M$  is the surface melt and runoff rate,  $Q_{snow}$  is the blowing snow  
638 sublimation rate, and  $D$  is the blowing snow divergence rate term, all with units of mm w.e. hr<sup>-1</sup>.  
639 Blowing snow refers to unconsolidated snow moved horizontally across the ice surface by winds  
640 above a certain threshold speed (Massom et al., 2001). As detailed in Francis et al. (2023), the  $P$   
641 and  $M$  terms are directly extracted from ERA-5, for which the reanalysis values are in close  
642 agreement with satellite-derived estimates over Antarctica, while the remaining three ( $Q_{sfc}$ ,  $Q_{snow}$ ,  
643  $D$ ) are calculated using parameterization schemes, described in Supplement Section S4. The hourly  
644 PWRF output is also used to estimate the SMB for the 11-16 July 2022 case study, with  $M$  given  
645 by the decrease in ST when the air temperature is above freezing after accounting for the other  
646 processes. Positive values of SMB indicate an accumulation of snowfall at the site, while negative  
647 values represent a reduction due to melting, sublimation or wind erosion processes, or a  
648 combination of the three. It is also important to note that, following the convention of Dery and  
649 Yau (2002) adopted by Francis et al. (2023), positive values of  $Q_{sfc}$  indicate deposition while  
650 negative values indicate sublimation. For  $Q_{snow}$ , on the other hand, positive values indicate  
651 sublimation and negative values indicate deposition.

### 652 3. Sea-Ice and Snow Thickness Variability

653 In the bottom panels of Figs. 3e-fa, the derived values of ST and SIT from 08 July to 30  
654 November 2022 at the Khalifa SIMBA site on fast ice off the Mawson Station are plotted. The  
655 uncertainty, which is estimated to be 7% for ST and 2% for SIT (Liao et al., 2018), is highlighted  
656 by the blue shading. The SIT exhibits a gradual increase starting on 08 July, peaking at 1.14-1.16  
657 m from 19-24 October, followed by a steady decline to 0.06-0.10 m at the end of November. These  
658 values are comparable to those estimated for this region and time of the year using satellite-derived  
659 products, which are typically in the range 0.50-1.50 m (Kacimi and Kwok, 2020). The ST on top  
660 of the ice, on the other hand, exhibits pronounced day-to-day variations as high as 0.08 m, peaking  
661 in mid-August to early September, and with values not exceeding 0.10 m from mid-September to  
662 the end of November. These values are also in the range of those derived from satellite altimeter  
663 data for that coastal region (Kacimi and Kwok, 2020).

665 In order to explore whether atmospheric forcing could have played a role in the observed  
666 variability in SIT and ST, the local SMB is estimated around the Khalifa SIMBA site on fast-ice  
667 off the Mawson Station using ERA-5 data. An analysis of Figs. 2 and 3 reveals that the SIT  
668 appears to be mostly driven by the growth (increase in SIT) and melting (decrease in SIT) at the  
669 ice bottom which, on top of the oceanic heat flux (Heil et al., 1996; Haas, 2017), depends on the  
670 conductive heat flux driven by the atmospheric forcing, ocean forcing, and involving both ocean-  
671 driven fast ice deformation and thermodynamic growth (Heil et al., 1996; Haas, 2017), and to a  
672 lesser extent, the SIT is impacted by the seasonal solar cycle, with the annual SIT decrease that  
673 initiates in late October/early November coinciding with the time when the air temperatures  
674 regularly climbs above 265 K (Fig. 2a; Fig. 3c) and there is increased solar insolation (note the  
675 strong diurnal variation in air temperature in Fig. 3c) at the site. The marked drop in SIT of 0.6 m  
676 from 20 November to 25 November seen in the bottom panel of Fig. 3fa corresponds to a period  
677 of warmer temperatures (>265 K; Figs. 2a and 3c) and increased solar insolation (note the strong  
678 diurnal variation in air temperature in Fig. 3c) at the site when the surface and air temperature  
679 climbed above freezing at the site (Fig. 2a). On the other hand, a comparison of the ST observations  
680 and the sea ice SMB estimated from ERA-5 (Equation 3+10) reveals a good correspondence  
681 between the two (cf. Figs. 3a-b with 3e). In particular, instances of positive SMB values (based on  
682 ERA-5) are typically associated with and followed by an increase in the measured ST at the site  
683 (e.g., in early July, mid-August, early and mid-October and mid-November), while negative SMB  
684 values from ERA-5 are accompanied by a decrease in the observed ST (e.g., in late July-early  
685 August and in late September-early October). Besides precipitation (snowfall) events, which can  
686 lead to an increase in ST by up to 0.06 m, Foehn effects winds also modulate ST. These correspond  
687 to episodes when the wind direction is offshore (typically southerly to southeasterly), with an  
688 increase in wind speed and air temperature and a decrease in relative humidity. Several of these  
689 occurrences are seen during the study period, such as in mid-July, early August, mid-September  
690 and late October, leading to a reduction in ST of up to 0.08 m in a day (cf. Figs. 3c-e). This is not  
691 surprising, as the Khalifa SIMBA site on fast-ice off the Mawson Station is exposed to katabatic  
692 winds flowing seaward off the interior plateau (Dare and Budd, 2001), which experience adiabatic  
693 compression as they descend towards coastal areas. Blowing snow, albeit less frequently, also  
694 affects the variability of ST: e.g., at the beginning of August, there is a 0.08 m decrease in ST  
695 during a blowing snow sublimation episode ( $Q_{\text{snow}}$  reaches 0.25 mm w.e.  $\text{hr}^{-1}$ ) followed by a  
696 Foehn event (Figs. 3b-e). Blowing snow divergence,  $D$ , on the other hand, plays a much-reduced  
697 role in the SMB, being of a larger magnitude during the passage of the AR on 14 July that brought  
698 wind speeds in excess of 30  $\text{m s}^{-1}$  (Figs. 3b-e). Surface melting is unlikely to be a major driver of  
699 ST, as evidenced by the zero values of  $M$  during the measurement period (Fig. 3b). This is because  
700 during July-November 2022, the surface and air temperatures at the site remained below freezing  
701 (Figs. 2a and 3c).  
702

703 Figs. 3g-l zoom-in during 11-16 July, when an AR impacted the site. On 14 July, very heavy  
704 precipitation (>2 mm w.e.  $\text{hr}^{-1}$ ) and strong easterly to southeasterly winds (> 30  $\text{m s}^{-1}$ ) occurred in

705 association with the AR, with a steady increase in air temperature from around 245 K on 13 July  
706 to 256 K at the beginning of 15 July (Figs. 3g and 3i-j). On the following day, Foehn effects  
707 occurred, as evidenced by the decrease in relative humidity from ~83% to 60%, the increase in  
708 wind speed from 12 to 28 m s<sup>-1</sup> with a shift from an easterly (96°) to a southeasterly (156°)  
709 direction, and a further 4 K increase in air temperature, Figs. 3i-j. The negative  $Q_{sfc}$ , which  
710 indicates surface sublimation, plays the largest role in the SMB during Foehn periods, Figs. 3g-h,  
711 in line with Francis et al. (2023). The 0.02 m drop in ST from 15 to 16 July, Fig. 3k, can be  
712 attributed to Foehn effects, while the absence of an increase in ST during the AR may be explained  
713 by the strong winds that blow the snow away and prevent it from accumulating at the instrument's  
714 location (note the positive blowing snow divergence,  $D$ , during the precipitation event, Fig. 3h).  
715 In fact, it has been reported that strong katabatic winds have blown the snow away as quickly as it  
716 falls on nearshore fast ice near the Mawson (Dare and Budd, 2001) and Syowa (Kawamura et al.,  
717 1995) stations, resulting in very low accumulation close to the coast. ERA-5 predicts some  
718 precipitation on 16 July, Fig. 3g, even though at much reduced levels compared to 14 July.  
719 However, the fact that the wind speed is much lower on this day, dropping below 2 m s<sup>-1</sup> (Fig. 3j),  
720 allows for snow accumulation at the Khalifa SIMBA site on fast ice off the Mawson Station that  
721 contributes to the observed 0.04 m increase in ST. The 0.02 m variations in SIT during 15-16  
722 July (Fig. 3l) are within the uncertainty range and hence can be ascribed to uncertainties in the  
723 methodology used for its estimation. It is important to note that a longer measurement period that  
724 comprises multiple AR passages would be needed for a robust link between ARs and their effects  
725 on ST and SIT to be established. Foehn winds are unlikely to play a dominant role in the sea ice  
726 SMB off the Mawson Station, even though the SIMBA site is exposed to katabatic winds flowing  
727 seaward off the interior plateau (Dare and Budd, 2001). This is evidenced in Fig. 3a, which shows  
728 that the sea ice SMB is largely controlled by precipitation ( $P$ ), while in Foehn wind events, surface  
729 sublimation ( $Q_{sfc}$ ) is the predominant term (Francis et al., 2023). For the case study discussed in  
730 Section 4 (11-16 November; Fig. 3b), there is a 0.06 m increase in ST from 14-15 November while  
731 the observed SIT increases by 0.04 m from 0.74 m to 0.78 m at the same time, returning to the  
732 previous levels (0.74 m) on 19 November. The results in Fig. 3b show a clear link between the  
733 observed measurements and the reanalysis' SMB for 14 November AR. The increase in SIT, on  
734 the other hand, may be explained by the freezing of (some of) the snow on top of the sea ice, as  
735 the surface and air temperatures were below freezing, around 265 K (Fig. 2a), and/or by  
736 metamorphic processes that can transform snow into ice (Sturm and Massom, 2017). The  
737 possibility that the added snow would depress the sea ice surface to below sea level, with the  
738 resulting flooding of the snow and subsequent freezing of the slush increasing SIT is unlikely. This  
739 is because the required conditions, namely a snow:ice thickness ratio in excess of 1:3, and an ocean  
740 water that is warm, with a temperature exceeding 268 K, and saline, with a bulk salinity higher  
741 than 5 psu (Sturm and Massom, 2017), are not met during this period.

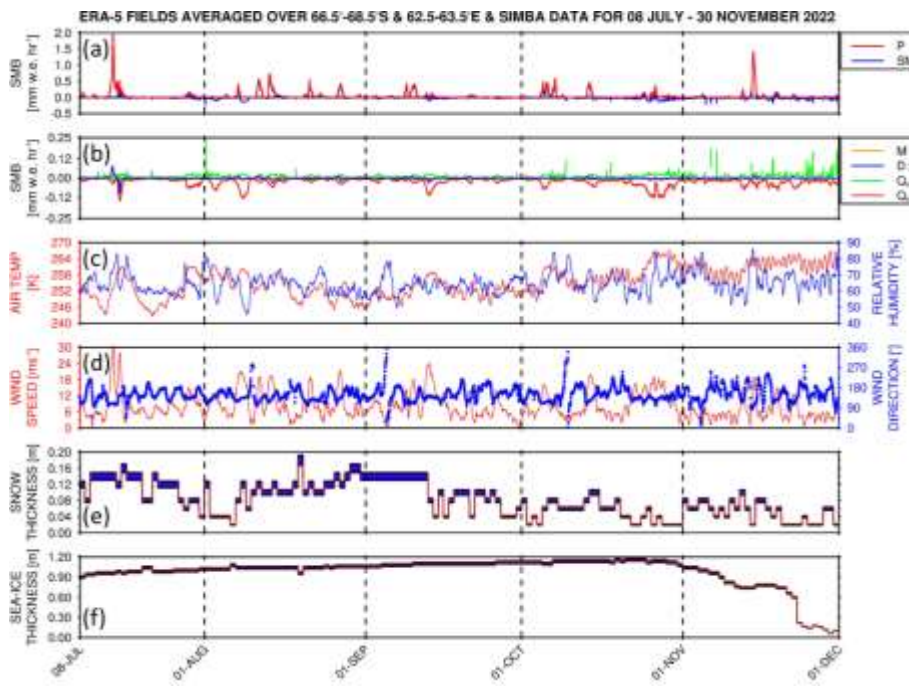
742  
743 Figure 4a gives the Pook Blocking Index, defined in Equation (S6), for the study period. It  
744 shows that a few blocking events occurred around east of the site during the

745 measurements, in particular around 120°E in late July-early August, 150°E in mid-late September,  
746 and around the Dateline in mid- to late-November-early October, and 180°E 120°W in mid- to  
747 late November during the month of October, when the ST was decreasing (Fig. 3a). Zoomed-in  
748 plots around the time of the Mawsoneach AR passage highlight the occurrence of blocking around  
749 the Dateline and 60°W in particular in August (Fig. 4d). The latter, which actually coincided with  
750 the passage of three consecutive ARs west of the Antarctic Peninsula during 10-12 and 13-15  
751 August (Fig. 4f), with the air temperature climbing above freezing (Fig. 4e). Wille et al. (2024c)  
752 and MacLennan et al. (2023) stressed that the occurrence of blocking can lead to the development  
753 of an “AR family” (or multi-AR) event, with the counterclockwise flow around the high-pressure  
754 and subsequent poleward advection of warm and moist low-latitude air masses leading to a marked  
755 rise in temperature. This is evident in particular around 120°E in late July-early August and mid-  
756 September, and around 150°E in late November (Figs. 4a-c). At the Khalifa SIMBA site on fast-  
757 ice off the Mawson Station, on the other hand, blocking did not occur, as evidenced by the small  
758 values of the Pook Blocking Index (Fig. 4a). During the case study in mid-July (–Figs. 4d-f),  
759 the presence of a ridge east of Mawson led to a second warm and moist air intrusion around 70°-  
760 90°E on 16 July. The passage of the AR at Mawson on 14 July two ARs also coincided with an  
761 increase in air temperature by more than 150 K in a couple of days (Fig. 4e), consistent with the  
762 observed rise in air temperature of ~18 K at the site (Fig. 2a) which is also noted for July. It is  
763 explained by the counterclockwise flow around high pressure systems and subsequent poleward  
764 advection of warm and moist low-latitude air masses. The most prominent such instance is around  
765 150°-180°E in late November 2022, when blocking around 180° led to an air temperature increase  
766 of more than 15 K to above freezing levels at some locations (cf. Figs. 4a-b).  
767

768 In Fig. 2, the timings of AR passages at the site i.e., 14 July, 13 August and 14 November, are  
769 highlighted by vertical dashed lines. In particular and in the July and August events, during the  
770 polar night, there is a marked increase in air temperature of up to 18 K as the low-latitude air mass  
771 reached the SIMBA site; this is also seen in the ERA 5 Hovmöller diagrams (Fig. 4e). In the 14  
772 November event, the increase is substantially reduced (by up to 3 K) as the air temperature is  
773 already much higher i.e., typically between 263-268 K. The ST increases by up to 0.06 m within  
774 1-2 days of the AR event, returning to pre-AR levels in the following 2-4 days. The small  
775 magnitude effect may arise from an increase due to snowfall during the passage of the AR and a  
776 decrease before and after the event due to evaporation/sublimation in response to the drier and  
777 windier conditions or snow removal by katabatic winds (Fig. 3a). Other processes, such as snow  
778 metamorphism, by which snow changes to sea ice (Sturm and Massom, 2017), can also play a  
779 role. In fact, strong katabatic winds have been observed to blow the snow away as quickly as it  
780 falls on nearshore fast ice near the Syowa Station, resulting in very low accumulation close to the  
781 coast (Kawamura et al., 1995), and off the Mawson Station as well (Dare and Budd, 2001). The  
782 SIT does not show a clear response to the passage of the ARs, except for the 14 November AR  
783 where a 0.04 m increase may arise from snow-ice interactions as noted before (Sturm and Massom,

784 2017). It is important to note that a longer measurement period would be needed for a robust link  
785 between ARs and their effects on ST and SIT to be established.  
786

787 The results in Figure 4 ~~stress highlight~~ the role of atmospheric dynamics in modulating the ST at  
788 the Khalifa SIMBA site on fast-ice off ~~the~~ Mawson Station, with the SIT largely controlled by  
789 ~~the oceanic and conductive heat flux dynamics (ocean driven fast ice deformation and~~  
790 ~~thermodynamic growth)~~ and ~~the~~ seasonal variability in ~~the~~ incoming solar radiation.  
791



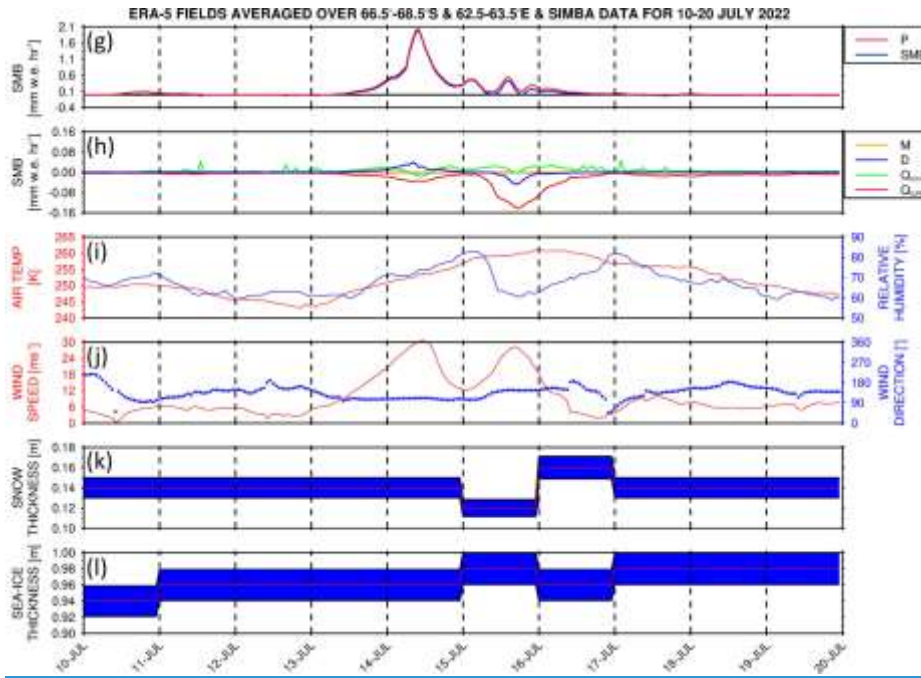


**Figure 3: Surface Mass Balance and SIMBA Observations:** ERA-5 hourly (a)-(b) surface mass balance ( $\text{mm w.e. hr}^{-1}$ ) from ERA-5 (top two plots), (c) air temperature (red; K) and relative humidity (blue; %), and (d) horizontal wind speed (red;  $\text{m s}^{-1}$ ) and direction (blue;  $^{\circ}$ ) averaged over  $66.5^{\circ}$ - $68.5^{\circ}$ S and  $62.5^{\circ}$ - $63.5^{\circ}$ E for the period 08 July and 30 November 2022. The local SMB terms plotted are the SMB (blue) and precipitation (red;  $P$ ) in (a), and the snowmelt (orange;  $M$ ), surface sublimation (red;  $Q_{sf}$ ), blowing snow sublimation (green;  $Q_{snow}$ ), and blowing snow divergence (blue;  $D$ ) in (b). No snowmelt occurred during the measurement period, and the  $D$  term is multiplied by two for visualization purposes. (e)-(f) give the and ST (m) and sea ice thickness (SIT; m) from the SIMBA measurements, respectively (bottom two plots) for the period 8 July to 30 November 2022. The red line shows the observed value while the blue shading gives the uncertainty, which is estimated as 7% for ST and 2% for SIT (Liao et al., 2018). (b) is as (a) but for 10-20 July/November 2022. The local SMB terms plotted are the SMB, precipitation (P), snowmelt (M), surface sublimation ( $Q_{sf}$ ), blowing snow sublimation ( $Q_{snow}$ ), and blowing snow divergence (D). (g)-(l) are as (a)-(f) but for 10-20 July 2022. No scaling is applied to the  $D$  term.

**Formatted:** Not Superscript/ Subscript

**Formatted:** Not Superscript/ Subscript

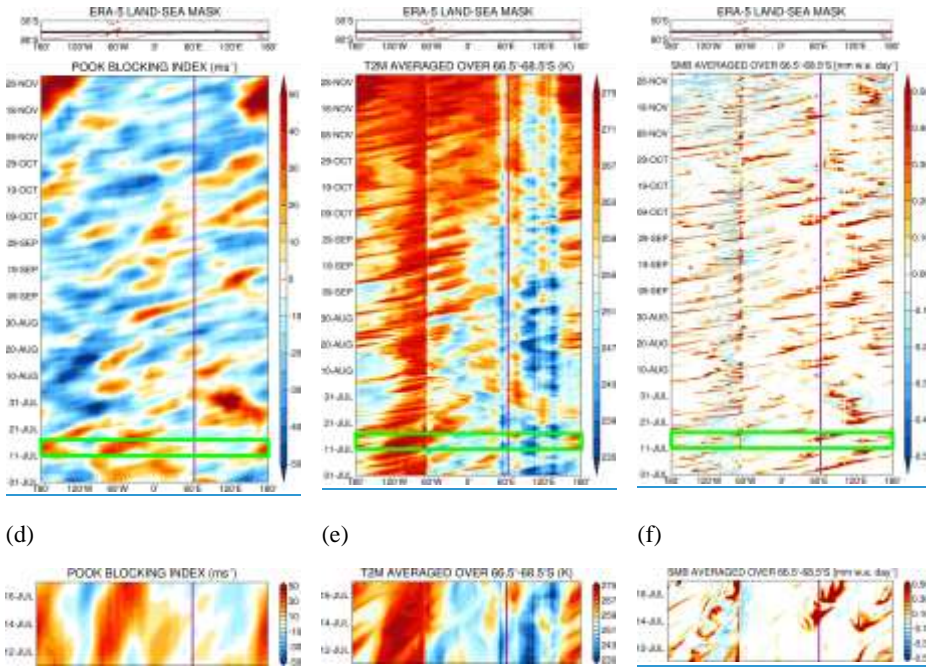


**Figure 4: Atmospheric dynamics and thermodynamics during the Observational Period:** (a) Pook blocking index ( $\text{m s}^{-1}$ ) for July-November 2022. The vertical purple line gives the approximate longitude of the measuring site. Regions where the index exceeds  $40 \text{ m s}^{-1}$ , an indication of a high degree of blocking, are stippled. The green rectangles indicate the periods when an AR impacted the site: 11-16 July, 10-15 August, and 11-16 November. The latter is considered for modeling and is highlighted with a thick line. Above the Hovmöller plot, the land-sea mask as seen by ERA-5 is plotted in red and the averaging region is highlighted with a black rectangle. (b) and (c) are as (a) but for air temperature (K) and the SMB, defined in equation (3), respectively, averaged over  $68.5^{\circ}$ - $66.5^{\circ}$ S. The sharp transition in the temperature field around  $60^{\circ}$ W arises due to the presence of the Antarctic Peninsula (landmass). While the stipple in (b) indicates regions and times when the temperature is above freezing ( $273.15 \text{ K}$ ). (e) is as (b) but for the SMB defined in equation (310). (d)-(f) are as (a)-(c) but zooming in for 11-16 July 2022 each of the three periods.

793

794 **4. Case Study: 11-16 JulyNovember 2022**

795 An The strongest AR to impacted the site during July-November 2022 occurred on 14  
 796 JulyNovember. In Section 4.1, the large- and regional-scale environment that promoted the  
 797 development of the AR is investigated, while in Section 4.2 the results of the PWRF simulations  
 798 are discussed.

799 **4.1 Large-Scale Atmospheric Patterns**

300 The period 10-19 JulyNovember 2022 is characterized by a strong wavenumber #3 pattern  
301 alongin the Southern Hemisphere polar jet at about 60°Smidlatitudes and a wavenumber #5  
302 pattern along the subtropical jet at about 30°S (Fig. 5a), projecting onto the in association with a  
303 positive phase of SAM (Fig. 5b)-phase. In fact, the SAM index for November 2022 is the third  
304 highest since 1979, and is more than 1.5 standard deviations above the 1979-2021 climatological  
305 mean (Fig. S1a). The stationary wave activity flux vectors in Fig. 5a show little wave propagation  
306 from the tropics into the Southern Hemisphere mid-latitudes, with a prevailing zonal propagation  
307 within the wavenumber #5 pattern. This is also evidenced by the strong westerly flow around  
308 Antarctica (Figs. 5c-d). One of the reasons for the positive SAM is the La Niña that was taking  
309 place at the time, the third consecutive La Niña year after the 2018-2019 El Niño (NOAA/NWS,  
310 2024). La Niña events favour a stronger than normal Amundsen Sea Low (Raphael et al., 2016),  
311 as was the case during November 2022 (Fig. 5b). In the previous month (October) it was even  
312 deeper, with a cyclone in the South Pacific Ocean reaching a sea level pressure of 900 hPa, making  
313 it the strongest extratropical cyclone since the start of the satellite era in 1980 to date (Lin et al.,  
314 2023).

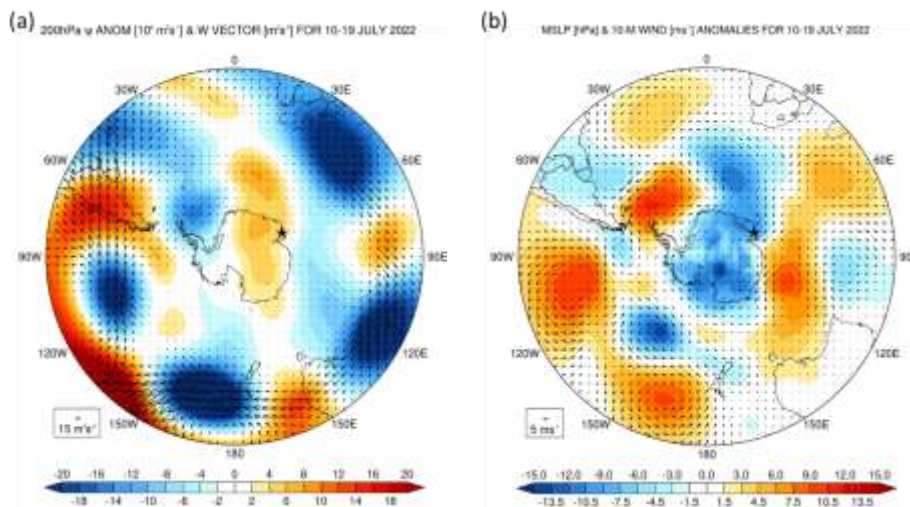
315 **Formatted:** Font: 14 pt, Bold

**Formatted:** Font: 14 pt, Bold

**Formatted:** Font: 14 pt, Bold

**Formatted:** Not Highlight

**Formatted:** Font: 12 pt



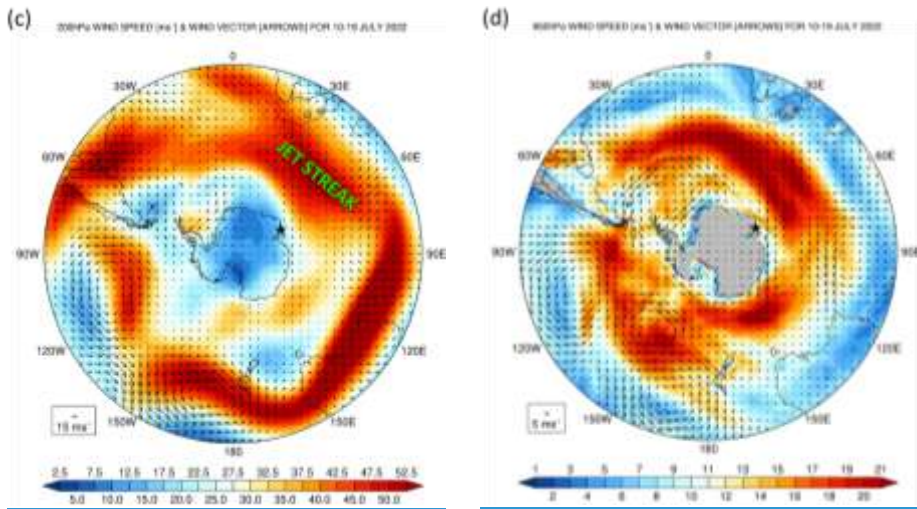


**Figure 5: Large-Scale Circulation during 10-19 July/November 2022:** (a) 200 hPa stream-function anomalies (shading;  $10^6 \text{ m}^2 \text{ s}^{-1}$ ), with respect to the hourly 1979-2021 climatology, and the stationary W vectors (Takaya and Nakamura, 2001; equations (2a) and (2b); arrows;  $\text{m}^2 \text{ s}^{-2}$ ) averaged over 10-19 July/November 2022. (b) Sea-level pressure (shading; hPa) and 10-m wind vectors (arrows;  $\text{m s}^{-1}$ ) anomalies for the same period. (c) and (d) show the 200 hPa and 850 hPa wind speed (shading;  $\text{m s}^{-1}$ ) and vectors (arrows) averaged over the same period. The jet streak referred to in the text is highlighted in (c). In all panels, the star gives the location of the Mawson Station (67.5912°S, 62.8563°E).

816  
817

818 North of Mawson Station, a pressure dipole is present around 40°-65°S (Fig. 5-b), with a ridge to  
819 the east and a trough to the west, with both features more than one two standard deviations away  
820 from the climatological mean (not shown Fig. 6e). This pattern favours the poleward propagation  
821 of warm and moist low-latitude air into the Khalifa SIMBA site on fast ice off the Mawson Station  
822 in East Antarctica, and is conducive to the development of ARs (Francis et al., 2022b;  
823 Gorodetskaya et al., 2023). The interaction between the subtropical jet and polar jet (Fig. 5c) led  
824 to the development of a jet streak (Fig. 5c), a localized maximum in the strength of the flow. with  
825 The low pressure associated with the AR (Fig. 5a) is located to the south of the jet entrance, in an  
826 area favourable for cyclogenesis (Wallace and Hobbs, 2006) on 13-14 November that promoted  
827 an intensification of the low. Despite its slow eastward movement and anomalous high strength,  
828 the meridional extent of the ridge from East Antarctica to southeastern Madagascar may explain  
829 why it is not detected by the Pook blocking index (Fig. 4a and eE) equation (S67),  
830 as the westerly flow at 35°-40°SN and 65°-70°SN is also weaker. In any case, this pressure dipole  
831 fosters the transport of warm and moist low-latitude air across the SIMBA site and is conducive  
832 to the development of ARs (Francis et al., 2022b; Gorodetskaya et al., 2023). The ARone that  
833 developed on 14 July/November 2022 is particularly remarkable, extending from the southwestern

Formatted: Font: 14 pt, Bold

Formatted: Font: 14 pt, Bold

834 Indian Ocean ~~tropical Africa~~ into the Southern Ocean and East Antarctica, ~~and having its primary~~  
835 ~~origin in South America~~ (Figs. 6a-b). ~~The wavetrain extending from South America to the~~  
836 ~~southeastern Pacific Ocean to South America~~ comprises a ridge over southern parts of Chile and  
837 Argentina, and a low over northern Argentina to the west of South Atlantic subtropical high (Figs.  
838 S1b, S1d and S1f). The pressure gradient between the latter two systems leads to a strengthening  
839 of the South American low-level jet (Marengo et al., 2004; Montini et al., 2019), which advects  
840 moisture from equatorial South America into the subtropics and helps to feed convection east of  
841 the Andes (Figs. S1a, S1c, and S1e). The moist outflow coming out of South America and the  
842 latent heat release from the convection strengthen the low pressure to the southwest of South Africa  
843 that is tracking southeastwards, and promote the development of the AR that impacted the Khalifa  
844 SIMBA site on fast-ice off the Mawson Station on 14 July. After a first landfall on 14 July around  
845 Mawson Station, Fig. 6a, the AR made a second landfall around 75°-90°E, Fig. 6b, impacting a  
846 wide swath of East Antarctica from about 45°E to 100°E. Here, the air temperature anomalies  
847 generally exceeded 10 K, with some parts of East Antarctica having near-surface temperatures in  
848 the top 1% of the 1979-2021 climatological distribution (Fig. 6d). The IVT anomalies at 06 UTC  
849 on 14 July November exceeds  $1560 \text{ kg m}^{-1} \text{ s}^{-1}$  around the Khalifa SIMBA site on fast-ice off the  
850 Mawson Station and  $8400 \text{ kg m}^{-1} \text{ s}^{-1}$  further north along the AR (Fig. 6b), with the hourly IVT on  
851 this day being in the top  $0.54\%$  of the climatological distribution (Fig. 6e), an attestation to the  
852 extreme nature of this event. The air temperature anomalies are also noteworthy, exceeding  $108 \text{ K}$   
853 in parts of East Antarctica around and just eastwest of the SIMBA site (Fig. 6d), where in some  
854 parts they are in the top 1% of more than two standard deviations above the 1979-2021  
855 climatological distribution mean (not shown). A back-trajectory analysis performed with  
856 HYSPLIT forced with ERA-5 data revealed tropical and subtropical moisture sources contributed  
857 to the 14 July 2022 AR (Fig. S2a). While at lower levels the moisture came from the Southern  
858 Ocean, with specific humidity values generally below  $2 \text{ g kg}^{-1}$  and air temperatures generally  
859 below freezing, at 2250 m it originated in the subtropics just south of South Africa with specific  
860 humidity values in excess of  $6 \text{ g kg}^{-1}$  and air temperatures around 280-290 K (Figs. S2b-e). The  
861 latter air mass ascended from roughly 200 m to 2250 m just north of the Mawson Station, when it  
862 encountered the colder and drier katabatic airflow (Fig. S2a). Several studies report on ARs  
863 impacting Antarctica being fed by subtropical moisture, such as the February 2011 (Terpstra et al.,  
864 2021) and the November-December 2018 (Gorodetskaya et al., 2020) ARs over East Antarctica,  
865 and the February 2022 AR over the Antarctica Peninsula (Gorodetskaya et al., 2023).  
866  
867 This AR and attendant cyclone also and associated warm and moist air intrusion left a  
868 considerable imprint on the weather conditions over East Antarctica around and to the west of the  
869 Mawson Station. Furthermore, it had an important effect on the sea ice in the region. As seen in  
870 Figs. S3a-b, there was a considerable reduction in SIE from 124 to 167 July November both around  
871 coastal Antarctica and upstream, with an open-ocean polynya developing well northwest of the  
872 Mawson Station around  $64^{\circ}\text{S}, 45^{\circ}\text{E}$  on 14 July and disappearing on 22 July. The role of ARs and  
873 the surface divergent flow associated with the attendant cyclone in opening up polynyas has been

Formatted: Font: 12 pt

874 reported at multiple sites around Antarctica (Francis et al. 2019, 2020). The low-pressure system  
875 northwest of Mawson reached a minimum value of 944 hPa on 12 July over the Southern Ocean,  
876 with the secondary low that formed on 14 July reaching 933 hPa on this day at 06 UTC just off the  
877 Khalifa SIMBA site on fast ice off the Mawson Station (Fig. 6a), and deepening further to 931  
878 hPa late on 15 July just to the northeast of the site (Fig. 6b). These systems are stronger than those  
879 that played a role in the opening up of the Weddell Sea ~~Polynya~~ in September 1973 and 2017  
880 (Francis et al., 2020), and the Maud Rise ~~Polynya~~ in September 2017 (Francis et al., 2019). The  
881 sea-ice vectors in Figs. S3c-d show an equatorward movement north of Mawson Station from 124-  
882 143 July November (prior to the event) ~~at speeds in excess of 40 km day<sup>-1</sup>~~ and a southward  
883 movement from 14-16 July November (post event) at speeds in excess of 205 km day<sup>-1</sup>, ~~the latter~~  
884 ~~an order of magnitude larger than that estimated during 12-14 November at the same site.~~ These  
885 sea-ice drift velocities, ~~which are associated with the changing wind field in response to the shift~~  
886 ~~in the position of the mid-latitude weather systems in the region (Figs. 6a-b, 6d and 7)~~, are ~~higher~~  
887 ~~than~~ ~~comparable to~~ those observed in the western Ross Sea in late April 2017 (Fonseca et al., 2023)  
888 ~~and comparable to those estimated in the region in September 2017 (Francis et al., 2019). They~~,  
889 ~~and are associated with the changing wind field in response to the shift in the position of the mid-~~  
890 ~~latitude weather systems in the region (Figs. 6a-b, 6d and 7).~~

891  
892 The southeast northwest convective band over southern Africa is a potential TTT event, resulting  
893 from the interaction of mid-latitude weather systems with tropical convection. Such TTTs are  
894 known to precondition the environment for the development of ARs, as in the March 2022 East  
895 Antarctica “heat” wave (Wille et al. 2024a,b). In order to quantify its strength and check whether  
896 a TTT event took place during the study period, the TTT index put forward by Ratna et al. (20123),  
897 which is based on OLR and meridional wind (equations S7-S88a,b), is utilized (Fig. S1b). While  
898 the meridional wind index does exceed half of its climatological standard deviation during 12-13  
899 November, the OLR index does not meet its condition of being higher than 1.5 the climatological  
900 standard deviation. Hence, no TTT event occurred during 10-20 November 2022. Having said this,  
901 tropical and subtropical moisture contributed to the warm and moist air intrusion that impacted  
902 East Antarctica. This is evident in the back trajectories obtained with HYSPLIT forced with ERA-  
903 5 data (Fig. S2). While at lower levels (500 m and 1500 m) the moisture came from the Southern  
904 Ocean, at 2500 m it originated in the subtropics just south of South Africa before rising just north  
905 of the Mawson Station when this moist air mass encountered the colder and drier katabatic airflow.  
906 Even at 500 m, the dry air parcels descending the Antarctic plateau into the Southern Ocean are  
907 moistened over the water before turning back to Antarctica and reaching the site (Figs. S2b-e).  
908 Several studies report on ARs impacting Antarctica being fed by subtropical moisture, such as the  
909 February 2011 (Terpstra et al., 2021) and the November-December 2018 (Gorodetskaya et al.,  
910 2020) ARs over East Antarctica, and the February 2022 AR over the Antarctica Peninsula  
911 (Gorodetskaya et al., 2023).

912

(a)

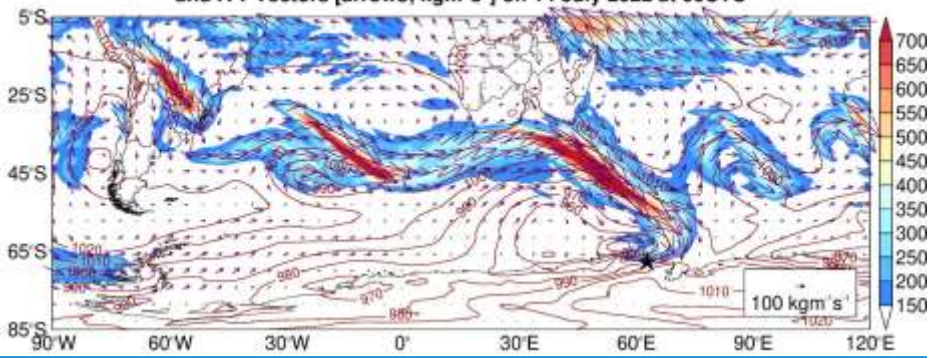
Formatted: Font: 12 pt

Formatted: Font: 12 pt

Formatted: Font: 12 pt

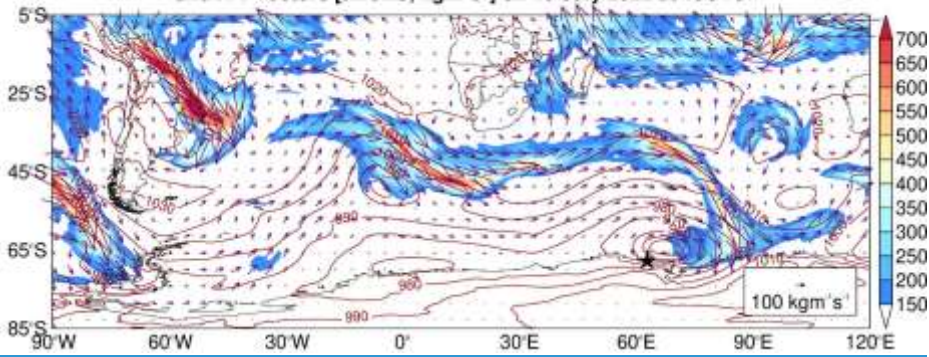
Formatted: Font: 12 pt

Sea-Level Pressure [contours; hPa], IVT Magnitude [shading; kgm's<sup>-1</sup>]  
and IVT Vectors [arrows; kgm's<sup>-1</sup>] on 14 July 2022 at 06UTC

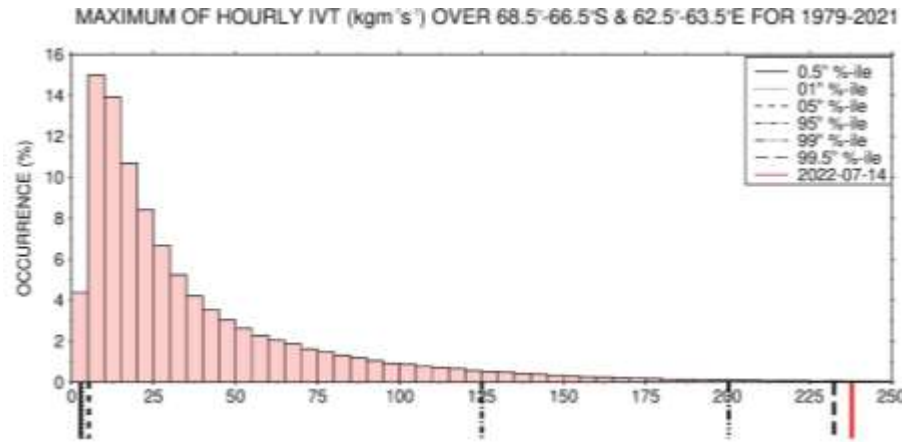


(b)

Sea-Level Pressure [contours; hPa], IVT Magnitude [shading; kgm's<sup>-1</sup>]  
and IVT Vectors [arrows; kgm's<sup>-1</sup>] on 15 July 2022 at 15UTC



(c)



(d) AIR TEMPERATURE [K] & 10-M WIND [ $\text{ms}^{-1}$ ] ANOMALIES ON 16-JUL-2022 @ 00UTC  
GREEN STIPPLE: AIR TEMPERATURE IN TOP 1% OF 1979-2021 CLIMATOLOGY

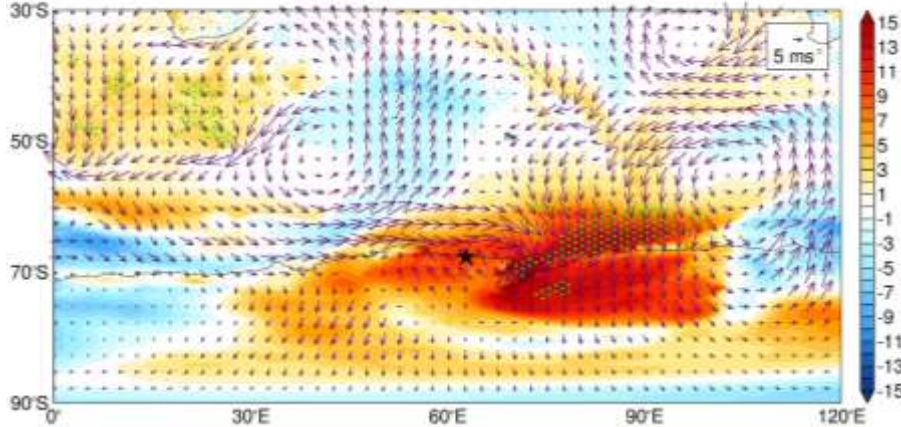


**Figure 6: Atmospheric River on 14 July/November 2022:** (a) Sea-level pressure (contours; every 10 hPa), Integrated Vapour Transport (IVT) magnitude (shading;  $\text{kg m}^{-1} \text{s}^{-1}$ ) and vectors (arrows;  $\text{kg m}^{-1} \text{s}^{-1}$ ) on (a) 14 July 2022 at 06 UTC and (b) 15 July 2022 at 15 UTC from ERA-5. The star gives the location of the Mawson station. MODIS visible image on 14 November 2022 over the domain 10°W-90°E and 50°N-75°S. The location of the Atmospheric River, Mawson Station (star) and a coastal polynya to the east of the station are highlighted. Image Credits: NASA WorldView. (b) Integrated Vapour Pressure (IVT;  $\text{kg m}^{-1} \text{s}^{-1}$ ) anomalies, the shading gives the magnitude and the arrows the vectors, on 14 November 2022 at 06 UTC with respect to the hourly 1979-2021 climatology from ERA-5. (c) Histogram of the maximum/median hourly IVT around the Mawson station (for the domain 68.5°-66.5°S and 62.5°-63.5°E); black box in (b), for 1979-2021. The solid, dotted, dashed, dotted-dashed, and dashed-dotted-dotted and long dashed lines give the 0.5<sup>th</sup>, 1<sup>st</sup>, 5<sup>th</sup>, 95<sup>th</sup>, and 99.5<sup>th</sup> percentiles, respectively, while the red-

Formatted: Font: 14 pt

Formatted: Font: 11 pt

Formatted: Not Superscript/ Subscript

Formatted: Font: 11 pt, Not Superscript/ Subscript

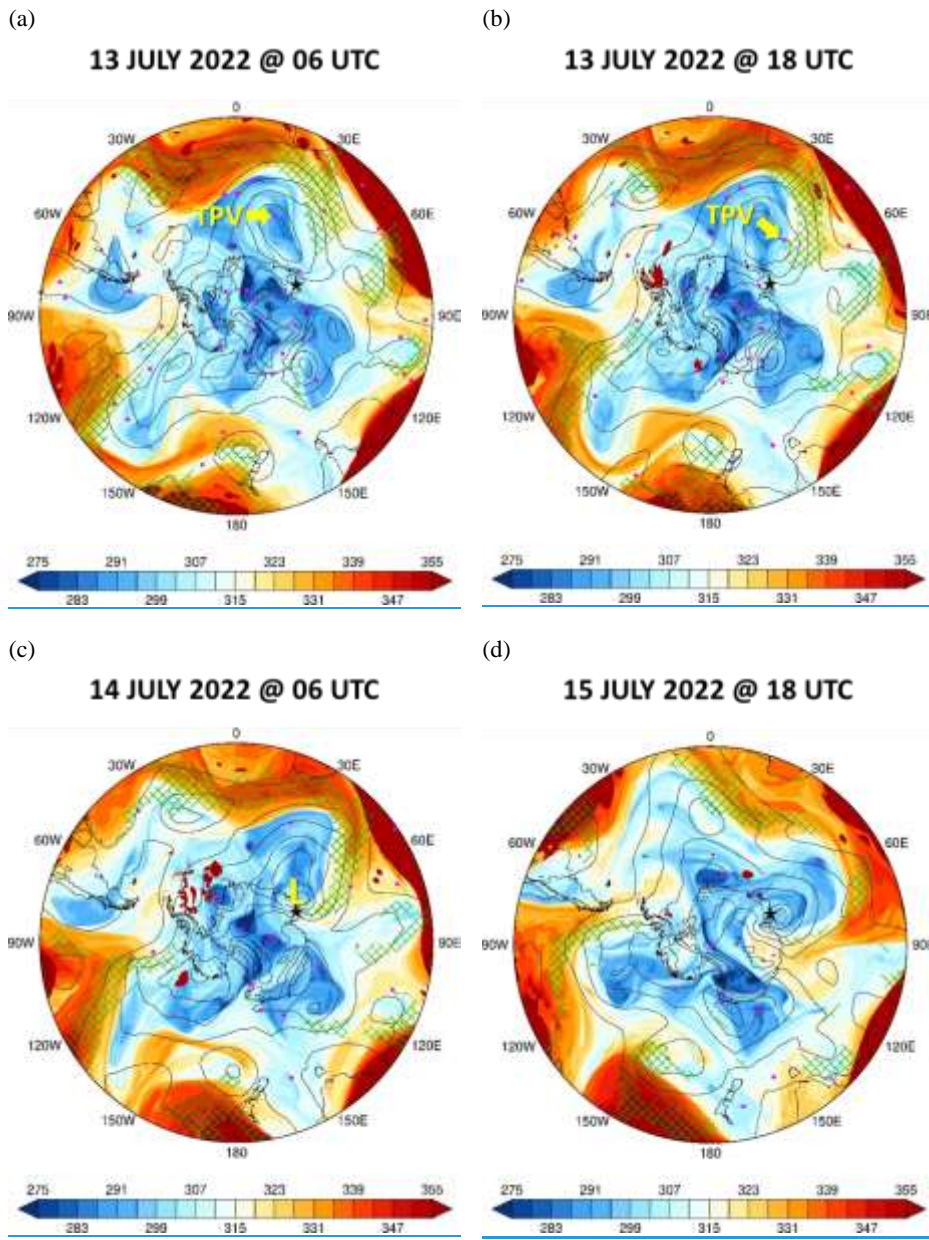
Formatted: Not Superscript/ Subscript

green and blue lines indicates the minimum, mean and maximum hourly values on 14 JulyNovember 2022. (d) is as (b) but for the air temperature (shading; K) and 10-m wind vectors (arrows;  $m s^{-1}$ ) anomalies with respect to 1979-2021 climatology on 16 July 2022 at 00 UTC. The green stipple indicates regions where the air temperatures are in the top 1% of the 1979-2021 climatological distribution, while in (e) the shading gives the sea-level pressure and the arrows give the 10-m wind vector standardized anomalies.

913  
914 Figures 5-6 provide a summary of the weather conditions during 10-1920 JulyNovember 2022, with Fig. 6 focusing on the AR event that impacted the Mawson Station peaked on 14  
915 JulyNovember. In order to gain insight into this AR event, it is important to assess the temporal  
916 evolution of the atmospheric circulation prior to and during the event itself. This is achieved in  
917 Fig. 7, which shows multiple fields every 12 h from 13 JulyNovember at 0618 UTC to 15  
918 JulyNovember at 1806 UTC. At 0618 UTC on 13 JulyNovember (Fig. 7a), a broad low-pressure  
919 system is centered northwest of the site, coincident with a TPV (highlighted in the figure), which  
920 came from the Antarctic plateau (full track shown in Fig. S1e), with a ridge to its east. The  
921 TPV helps the surface low to intensify, together with the jet streak at upper levels (Fig. 5c), with  
922 the central pressure dropping to around 944 hPa on 12 July at 12 UTC. The pressure dipole  
923 promotes the southward advection of a warmer and moist low-latitude air mass into the Southern  
924 Ocean, as noted by the hatching that highlights regions where the IVT exceeds  $250 \text{ kg m}^{-1} \text{ s}^{-1}$ . A  
925 secondary low, which develops later on 134 JulyNovember (highlighted in Fig. 7cb, also  
926 noted by the additional sea-level pressure contour), is not co-located with a TPV. Instead, the  
927 secondary low is driven by the interaction of the warm and moist air mass from the west and  
928 northwest around the low pressure with that from the northeast around the ridge. Closer and also  
929 closer to the Antarctic coast, the aforementioned low-level convergence is reinforced by also with  
930 the drier and colder katabatic flow blowing from the continent. The maximum Eady growth  
931 rate, a measure of baroclinicity (Hoskins and Valdes, 1990), at 850 hPa exceeded  $3 \text{ day}^{-1}$  on 14  
932 JulyNovember (not shown), indicating a highly baroclinic environment.  
933

Formatted: Font: 12 pt

934  
935 Figures 7b-de show cyclonic Rossby wave breaking, with the secondary low exhibiting little  
936 eastward movement owing to the presence of a strong ridge to the east (Figs. 6a-be), and instead  
937 shifting southwards towards Antarctica. The incursion of the higher low-latitude potential  
938 temperature values into East Antarctica (Figs. 7b-d) is consistent with the warmer (Fig. 6d) and  
939 more moist (Figs. 6ab-c) conditions in the region. The flow became westerly and the warm and  
940 moist air intrusion weakened and shifted eastwards from 14 to 15 JulyNovember (Figs. 7c-d) and  
941 penetrated deeper into East Antarctica on 15-16 July (Figs. 7d and 6d), with air temperatures more  
942 than 15 K above climatology in some parts (Fig. 6d), with another warm and moist air intrusion  
943 (albeit weaker) developing to the northwest of the site (Fig. 7d) later impacting the area on 16-17  
944 November (not shown). Fig. 7 shows more than one episode of intrusion of low-latitude air masses  
945 into Antarctica. For example, on 14-16 JulyNovember a warm and moist air intrusion reached the  
946 Antarctic Peninsula/Victoria Land just to the west of the Ross Sea (Figs. 7c-d). Such occurrences  
947 are more common in an amplified pattern and can be aided by TPVs that act to strengthen the  
948 attendant cyclone (Wille et al., 2024c).



950

**Figure 7: Evolution of Atmospheric State during 13-15 JulyNovember 2022:** Potential temperature ( $\theta$ ; shading; K) on the dynamical tropopause (PV = -2 PVU), sea-level pressure (black contours; every 15 hPa starting at 900 hPa) and integrated vapour transport (IVT; hatching if  $> 250 \text{ kg m}^{-1} \text{ s}^{-1}$ ) on (a) 13 JulyNovember at (a) 06 UTC and (b) 18 UTC, (c) 14 JulyNovember at (b) 06 UTC, and (d) 15 July at 18 UTC, and (d) 15 November at 06 UTC. The purple dots indicate the location of tropopause polar vortices (TPV) at the respective times. The TPV and the secondary low pressure discussed in the text are highlighted in panels (a) and (b) and (c), respectively.

Formatted: Font: 11 pt

951

## 4.2 PolarWRF Simulation

952 In this subsection, the focus is on the modeling experiments. In Section 4.2.1, the PWRF  
 953 predictions are evaluated against *in-situ* measurements at the five four stations in East Antarctica  
 954 given in Fig. 1b, while in Section 4.2.2 the emphasis is on the additional insight the higher-  
 955 resolution model data gives on the mid-JulyNovember 2022 AR event.

Formatted: Font: 14 pt, Bold

956

### 4.2.1 Evaluation of PolarWRF

957 The PWRF simulations for 11-16 JulyNovember 2022 are evaluated against *in-situ*  
 958 meteorological observations at the Mawson, Syowa, Mizuho and Relay, Davis and Casey stations,  
 959 in addition to surface radiation fields at Syowa Station. Fig. 8 shows the time-series of hourly data  
 960 for the Mawson and Syowa stations, with the corresponding time series for the other two stations  
 961 given in Fig. S4. A quantitative assessment of the model performance for all stations and variables  
 962 is presented in Table 34.

963

964 The PWRF simulates the weather conditions well at the Mawson (Figs. 8a-f), Syowa (Figs. 8g-lb  
 965 and S4a-f), Mizuho (Fig. S4a) and Relay (Fig. S4g-lb), Davis (Fig. S4m-r) and Casey (Fig. S4s-x)  
 966 stations for 11-16 JulyNovember 2022. In particular, (i) the observed variability in sea-level  
 967 pressure is well replicated, with the model correctly capturing the time of passage and strength of  
 968 the secondary cyclone on 14-15 JulyNovember at Mawson (Figs. 7c-db-e; Fig. 8c) and on 15 July  
 969 at the Davis (Fig. 7d; Fig. S4p) stations. Moreover, (ii) the warmer, more moist and  
 970 windier conditions on 12-14 July at Syowa Station (Figs. S4a-c and S4f), on 14-15 JulyNovember  
 971 at Mawson (Fig. 8a-c and 8e) and Relay (Fig. S4g-i and S4l) stations, and on 15-16 July at Davis  
 972 (Fig. S4m-o and S4r) and Casey (Fig. S4s-u and S4x) stations are predicted by the model at all  
 973 sites; and (iii) it. Also, the model captures the reduction in the surface downward shortwave  
 974 radiation flux by about 200 W m<sup>-2</sup>, or a third of its value, and the increase in the downward long-  
 975 wave radiation flux by up to 890 W m<sup>-2</sup> at Syowa Station (Fig. 8k) in association with the warm  
 976 and moist air intrusion on 13-14 July. An inspection of Table 34 reveals that, and except  
 977 mostlyainly for the air temperature and surface pressureby and large, the normalized bias  $\mu$  is  
 978 smaller than 0.5, indicating the (small magnitude) biases can be regarded as not significant, while  
 979 the normalized error variance  $\alpha$  does not exceed 1 for all fields and stations (except for the wind

Formatted: Font: 12 pt

Formatted: Font: 12 pt

Formatted: Not Superscript/ Subscript

Formatted: Font: 14 pt, Bold

vector at the higher-elevation Relay [and coastal Davis Stations](#)), indicating that the PWRF predictions can be regarded as trustful. The performance of PWRF for this [site and](#) event is comparable to that for the McMurdo Station in early January 2016 (Hines et al., 2019), for West Antarctica in early to mid-January 2019 (Bromwich et al., 2022), and for the Antarctic Peninsula for May-June 2019 and January 2020 (Matejka et al., 2021). This reflects the improvements made to PWRF by the model developers, with the aim of optimizing its performance and skill over Antarctica (e.g., Hines et al., 2021).

A closer inspection of Figs. 8 and [S45 and Table 3](#) reveals some discrepancies in the PWRF predictions. For example, at Syowa Station, the model has a tendency to over-predict the air temperature by  $\sim 1.32$  K. [This may explain the overestimation of the upward longwave radiation flux by about  \$14.3 \text{ W m}^{-2}\$  \(Fig. 8l\), which can also arise from an overprediction of the observed surface emissivity. The downward longwave radiation flux \(Fig. 8k\), on the other hand, is underestimated by roughly  \$7.7 \text{ W m}^{-2}\$ , likely related to the reduced atmospheric moisture content in the model by about  \$\sim 0.16 \text{ g kg}^{-1}\$ . While the downward shortwave radiation flux is generally well captured by the model, the upward shortwave flux has a significant negative bias of  \$\sim 68 \text{ W m}^{-2}\$ , which can arise e.g. from an underestimation of the observed surface albedo by around 10% \(roughly 0.84 for observations and 0.75 for PWRF for 11–16 November\). This suggests the need to properly represent land surface properties in the model, which has been highlighted by other studies \(e.g., Hines et al., 2019\). The lower albedo in PWRF leads to a positive bias in the net shortwave radiation flux, which is consistent with the warmer air temperatures and the enhanced upward longwave radiation flux biases of  \$\sim 11 \text{ W m}^{-2}\$ . At all four \[coastal Antarctica\]\(#\) stations, the predicted wind direction is \[generally\]\(#\) shifted clockwise by  \$45^\circ\$ – \$90^\circ\$  compared to that observed \(Figs. \[8d, S4e, S4q and S4w\]\(#\)\), with this mismatch \[at times reaching  \\$180^\circ\\$  being more evident\]\(#\) at the Relay Station \(Fig. \[S4k\]\(#\)\) located on the Antarctic plateau more than 3,000 m above sea-level \(Fig. \[12b\]\(#\)\). This \[discrepancy\]\(#\) can be attributed to an incorrect representation of the surface topography which, \[as for surface properties such as the albedo\]\(#\), exhibits a complex spatial heterogeneity in the region \(Lea et al., 2024\). Despite these issues, both the magnitude and variability of the observed wind speed are generally well represented by PWRF \(Figs. \[8e, S4f, S4l, S4r, and S4x3\]\(#\)\). The more offshore wind direction at the coastal \[Antarctica Mawson and Syowa\]\(#\) stations reflect a stronger katabatic wind regime that acts to slow the poleward movement of the \[warm and moist\]\(#\) low-latitude air mass, which is consistent with the dry bias of \[up to  \\$0.11\\$ – \\$0.216 \text{ g kg}^{-1}\\$\]\(#\) . \[The positive mixing ratio bias at the Relay Station occurs primarily on 15–16 July\]\(#\) \(Fig. \[S4h\]\(#\)\), and is associated with \[increased \\(but still rather low, generally below  \\$0.1 \text{ g kg}^{-1}\\$ \\) moisture levels advected from the interior of Antarctica\]\(#\). At all stations except Mawson, PWRF exhibits a warm bias \(Figs. \[8a, 8g, S4g, S4m, and S4s\]\(#\)\), with the near-surface wind speed being \[underestimated at Mawson \\(Fig. 8e\\) and overestimated at the other stations \\(Figs. S4f, S4l, S4r, and S4x\\)\]\(#\). Together with the dry bias, this suggests a tendency for excessive boundary layer mixing in the model compared to observations, which \[In fact, and in particular at the Mawson Station, when the model overpredicts the strength of the near-surface wind \\(e.g., around 00 UTC on 12 and 16 November and between 18–24 UTC on 13 November\\) from an offshore direction, there is a cold and dry bias, confirming\]\(#\)](#)

**Formatted:** Font: 12 pt

**Formatted:** Font: 12 pt

**Formatted:** Not Superscript/ Subscript

**Formatted:** Font: 12 pt

**Formatted:** Font: 12 pt

**Formatted:** Not Superscript/ Subscript

**Formatted:** Font: 14 pt, Bold

**Formatted:** Font: 12 pt

**Formatted:** Font: 12 pt

1021 the occurrence of an enhanced katabatic airflow. Table 1 also reveals that the control and model  
1022 simulation with updated SIE and SIT yield similar skill scores, a fact that is confirmed by the time-  
1023 series in Figs. 8 and S4. This suggests that a more realistic representation of the sea ice state, and  
1024 at least for this particular event and model configuration, does not translate into more accurate  
1025 predictions. By and large, the results in Figs. 8 and S4 indicate a tendency for drier and windier  
1026 conditions compared to observations. This has been reported in a number of PWRF studies (e.g.,  
1027 Wille et al. 2016, 2017; Vignon et al., 2019), and has been attributed to excessive too much  
1028 boundary layer mixing in the model. An optimized PBL scheme, which at least partially corrects  
1029 for the excessive mixing, and/or a more sophisticated land surface model that more accurately  
1030 represents the boundary layer and surface processes, have to be considered to address the  
1031 aforementioned biases. Despite this, PWRF captures the effects of the AR as seen in observations,  
1032 most notably the increase in air temperature and water vapour mixing ratio, and the strengthening  
1033 of the near-surface wind in particular at the more impacted Mawson (Figs. 8a-e) and Davis (Figs.  
1034 S4m-r) Stations. The SMB analysis performed using ERA-5 data is repeated using the hourly  
1035 PWRF predictions. PWRF gives a similar estimate of the different terms of the SMB with respect  
1036 to the reanalysis dataset (cf. Figs. S5a-b with 3g-h), with the roughly 30% higher surface  
1037 sublimation on 15 July arising from the drier (~10% lower relative humidity; cf. Figs. S5c with 3i)  
1038 and windier (~10% higher wind speed; cf. Figs. S5d with 3j) near-surface conditions in the model.  
1039 The fact that ERA-5 can capture Foehn effects at this site and for this event, at least for  
1040 this one, suggests that it can be used for the study wider analysis of Foehn events in around East  
1041 Antarctica, as has been done over West Antarctica (Francis et al., 2023) and the Antarctica  
1042 Peninsula (Laffin et al., 2021). The up to ~2 mm w.e.  $hr^{-1}$  precipitation rate (Figs. S5a and 3g), ~5  
1043 K air temperature increase (Fig. S5c and 3i), and 30 m  $s^{-1}$  wind speeds (Fig. S5d and 3j) associated  
1044 with the passage of the AR on 14 July are simulated by PWRF, with the cold bias in the model  
1045 also seen in comparison with *in-situ* measurements at Mawson Station (Table 3).  
1046

1047 Fig. 8f shows a comparison of the observed and simulated snow depth at the Khalifa SIMBA site  
1048 on fast ice off the Mawson Station. The ST in PWRF is initialized to zero, and hence the  
1049 discrepancy with respect to the observed values during 11-13 July (the observed ST is equal to  
1050 0.14 m during 10-14 July). PWRF predicts around 0.24 m of snowfall in association with the  
1051 passage of the AR on 14 July and the weaker wind speeds in the model, at times by more than 20  
1052 m  $s^{-1}$ , likely allow for snow to accumulate at the site instead of it being blown away by the wind.  
1053 The model fails to capture the observed decrease of 0.02 m in ST on 15 July in response to Foehn  
1054 effects, which can be attributed to less favourable conditions for Foehn events in the model, both  
1055 with respect to the wind direction (west-southwesterly in PWRF as opposed to southeasterly in  
1056 observations) and speed (lower by as much as 20 m  $s^{-1}$ ). A higher spatial resolution of at least 1  
1057 km would probably be needed for a more accurate simulation of the interaction of the AR with the  
1058 complex Antarctic topography including the Foehn effects (Gilbert et al., 2025). The increase in  
1059 ST on 16 July due to falling precipitation snowfall is simulated by PWRF, even though its  
1060 magnitude is underestimated by the model (0.01 m in PWRF as opposed to 0.04 m in observations),

1061 possibly because of the drier environment brought on by a more offshore wind direction (Figs. 8b,  
1062 8d-e, and S5b-d).

1063  
1064 Besides ground-based observations, sounding data are available at the Mawson, Syowa, Davis,  
1065 and Casey stations every 12 h (Figs. S5a) and can be compared with the hourly PWRF predictions  
1066 (Figs. S6 and S7b-e). The model captures the timing of the arrival of the warm and moist air mass  
1067 at Mawson on 14-15 July November well, as evidenced by the higher values of  $\theta_E$  (2780-2890 K;  
1068 Figs. S6a and S6e) and relative humidity (690-9100%; Figs. S6b and S6f). However, the katabatic  
1069 wind flow is stronger in the model as seen by the offshore wind direction (Fig. S6h) and drier  
1070 conditions (Figs. S6b and S6f), and also evident in the ground-based observations (Figs. 8d and  
1071 8b), with a strong low-level jet (mostly below 700 hPa) on 14 and 16 July (Fig. S6g). At Syowa,  
1072 the PWRF and observed profiles are in closer agreement than at the Mawson station (cf. Figs.  
1073 S6a-h with S6i-p). Here, the main discrepancy between the observed and modelled profiles is the  
1074 dry bias (Figs. S6j and S6n), which is more pronounced on 13-14 July, and is also evident in the  
1075 near-surface data (Fig. 8i). The arrival of the low-latitude air mass at Davis on 15 July is seen in  
1076 both the PWRF and observed profiles (Figs. S7a-h), with a less pronounced katabatic regime in  
1077 the model compared to that at the Mawson Station (cf. Figs. S6e-h with S7e-h). At Casey (Figs.  
1078 S7i-p), PWRF simulates the more moist conditions on 14 July and the drier conditions on 15-16  
1079 July. The analysis of the sounding profiles reveals, however, that PWRF tends to overestimate the  
1080 strength of the katabatic flow over coastal East Antarctica during 11-16 July. This has been noted  
1081 by Vignon et al. (2019), who attribute such overestimates to more stable boundary layers over  
1082 the Antarctic Plateau and, to a smaller lesser extent, steeper synoptic land-ocean pressure gradients  
1083 in the model. The northwesterly flow between 750 and 950 hPa late on 14 November is also  
1084 simulated by PWRF, even though the wind direction in the model tends to be more from an easterly  
1085 component compared to observations.

1086  
1087 The results in Figs. 8, S4-S7, and S64-S75, and Table 34 reveal a reasonably good PWRF  
1088 performance in the study area for the period 11-16 July November 2022. In the next subsection,  
1089 the model simulations are used to gain further insight into the dynamics of the 14 July AR for this  
1090 event. The simulation with the updated SIE and SIT was used for this purpose.

Formatted: Font: 14 pt

Formatted: Font: 12 pt

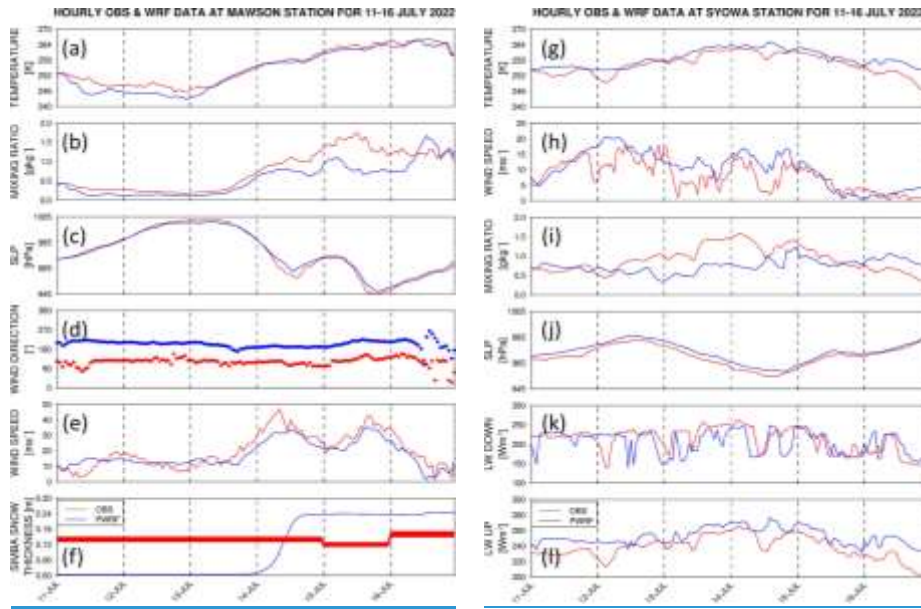


**Figure 8: Evaluation of PolarWRF against ground-based observations:** (a) Hourly (a) air temperature ( $^{\circ}\text{C}$ ), (b) water vapour mixing ratio ( $\text{g kg}^{-1}$ ), (c) relative humidity (RH; %), (d) sea-level pressure (SLP; hPa), and horizontal wind (d) direction ( $^{\circ}$ ) and (e) speed ( $\text{m s}^{-1}$ ) from observations (red) and for the PWRF simulation control (blue), PWRF simulation and the one with updated SIE and SIT (green) for 11-16 July November 2022 at the Mawson Station. (f) shows the daily observed (red) and hourly PWRF-predicted (blue) ST (m) at the Khalifa SIMBA site on fast ice off the Mawson Station, the former with the estimated 7% uncertainty. (g)-(l) is as (a)-(f) but for the hourly air temperature (K), horizontal wind speed ( $\text{m s}^{-1}$ ), water vapour mixing ratio ( $\text{g kg}^{-1}$ ), sea-level pressure (SLP; hPa), and surface downward and upward shortwave and longwave radiation fluxes ( $\text{W m}^{-2}$ ), respectively at the Syowa Station. The wind fields at Syowa Station are shown in Figs. S4e-f. The location of the stations is given in Fig. 1b.

Formatted: Font: 12 pt

Variable	Station	Bias	$\mu$	$\rho$	$\eta$	$\alpha$
Air Temperature	Mawson	-1.420.04 K	-0.9204	0.9884	$\sim 1.00 \pm 0$	0.0227
	Syowa	2.154.89 K	1.0877	0.8777	$0.98 \pm 0$	0.124
	Relay	2.514.13 K	0.6532	0.9084	$\sim 1.00 \pm 0$	0.109

	Davis	<u>3.11</u> K	<u>1.30</u>	<u>0.98</u>	<u>0.97</u>	<u>0.05</u>
	Casey	<u>2.66</u> K	<u>1.22</u>	<u>0.75</u>	<u>0.97</u>	<u>0.27</u>
Water Vapour Mixing Ratio	Mawson	-0. <u>2146</u> g kg <sup>-1</sup>	-0. <u>852</u>	<u>0.8677</u>	<u>0.98</u> ± <u>0</u>	<u>0.162</u> <u>4</u>
	Syowa	-0.1 <u>64</u> g kg <sup>-1</sup>	-0. <u>4534</u>	<u>0.0583</u>	<u>0.8298</u>	<u>0.964</u> <u>9</u>
	Relay	0.0 <u>12</u> g kg <sup>-1</sup>	<u>0.6928</u>	<u>0.753</u>	0.99	<u>0.258</u>
	Davis	<u>-0.09</u> g kg <sup>-1</sup>	<u>-0.28</u>	<u>0.97</u>	<u>0.94</u>	<u>0.08</u>
	Casey	<u>-0.02</u> g kg <sup>-1</sup>	<u>-0.12</u>	<u>0.61</u>	<u>0.92</u>	<u>0.43</u>
Wind Vector (Bias and $\mu$ are for wind speed)	Mawson	<u>-2.394.24</u> m s <sup>-1</sup>	-0. <u>4823</u>	<u>0.2735</u>	<u>0.967</u>	<u>0.746</u> <u>6</u>
	Syowa	<u>2.360.13</u> m s <sup>-1</sup>	<u>0.6104</u>	<u>0.3962</u>	<u>~1.00.9</u> <u>9</u>	<u>0.613</u> <u>9</u>
	Relay	<u>2.020.41</u> m s <sup>-1</sup>	<u>1.820.2</u> <u>5</u>	- <u>0.6073</u>	<u>~1.00.9</u> <u>8</u>	<u>1.607</u> <u>2</u>
	Davis	<u>1.40</u> m s <sup>-1</sup>	<u>0.36</u>	<u>-0.30</u>	<u>0.99</u>	<u>1.29</u>
	Casey	<u>0.79</u> m s <sup>-1</sup>	<u>0.24</u>	<u>0.08</u>	<u>0.98</u>	<u>0.93</u>
Surface Pressure	Mawson	- <u>3.784.22</u> hPa	- <u>1.722.7</u> <u>5</u>	<u>0.998</u>	~1.0	<u>0.013</u>
	Syowa	<u>3.084.03</u> hPa	<u>2.375</u>	0.99	~1.0	<u>0.012</u>
	Relay	<u>2.5324</u> hPa	<u>3.1620</u>	0.99	<u>0.99</u> ± <u>0</u>	<u>0.024</u>
	Davis	<u>-0.74</u> hPa	<u>-0.50</u>	<u>~1.0</u>	<u>~1.0</u>	<u>0.01</u>
	Casey	<u>-2.48</u> hPa	<u>-2.16</u>	<u>~1.0</u>	<u>0.99</u>	<u>0.01</u>
<b>Downward LW</b>	Syowa	<u>-7.714.40</u> W	-0. <u>2419</u>	<u>0.4763</u>	<u>~1.00.9</u>	<u>0.533</u>

		$\text{m}^{-2}$			$\varrho$	$\varrho$
Upward LW		14.260.71 W $\text{m}^{-2}$	1.5469	0.793	0.95 $\pm$ $\vartheta$	0.257

1094  
1095  
1096  
1097  
1098  
1099  
1100  
1101  
1102  
1103  
1104

**Table 34: Verification diagnostics with respect to station data:** Bias, normalized bias ( $\mu$ ), correlation ( $\rho$ ), variance similarity ( $\eta$ ), and normalized error variance ( $\alpha$ ) for air temperature, water vapour mixing ratio, horizontal wind vector and sea-level pressure for the Mawson, Syowa, Mizuho and Relay, Davis, and Casey Stations for 11-16 July/November 2022. For the Syowa Station, the scores are also given for the surface downward and upward shortwave and longwave radiation fluxes at the bottom of the table. Humidity measurements are not available at the Mizuho Station for this period. The first value gives the score for the control simulation, while the one in parenthesis is for the simulation with updated SIE and SIT. The model values are those at the closest model grid-point to the location of the station, and the evaluation is performed for hourly data. The correspondent time-series are given in Figs. S7 and S13.

1105 **4.2.2 Insights into the Dynamics and Effects of the AR**

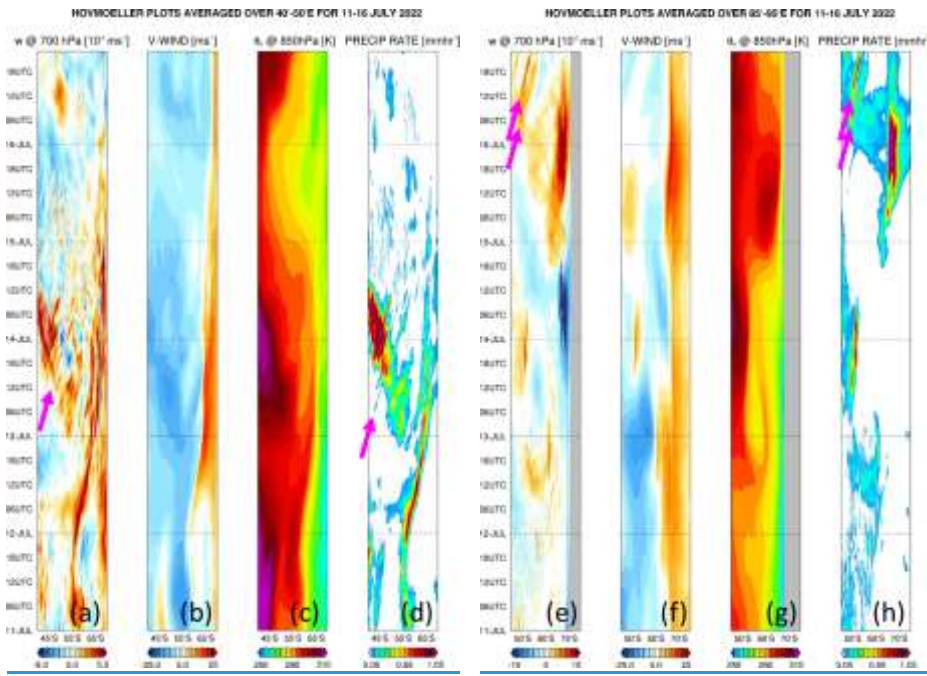
1106 One of the motivations for implementing the high-resolution (2.5 km) innermost grid is to  
1107 check for the presence of AR rapids (Box et al., 2023; Francis et al., 2024). Figs. 9a-de show a  
1108 hovmoeller plot of the vertical velocity at 700 hPa, 10-m meridional wind speed, the 850 hPa  
1109 equivalent potential temperature ( $\theta_E$ ), and precipitation rate averaged over 40°-50°E, a latitude  
1110 band that comprises the bulk of the AR (Figs. 6a7a-b and, 7a-c10a and 9i). It reveals AR rapids,  
1111 in particular one on 13-14 July between 40°-60°S (pink arrows in Figs. 9a and 9d), which is  
1112 embedded within the AR, as seen on 13 July at 12 UTC when it is located at 40°-50°S (Fig. 9i). No  
1113 AR rapids are seen in all fields as well as in the vertical profiles at the coastal Antarctic stations  
1114 (Figs. S6 and S75b), suggesting they are confined to the Southern Ocean. The linear structure  
1115 propagating from ~55°S late on 11 July to 65°S early on 13 July does not correspond to an AR  
1116 rapid. Instead, the heavy precipitation ( $>1 \text{ mm hr}^{-1}$ ; Fig. 9d) arises instead and from 12 UTC on 13  
1117 November to 12 UTC on 14 November, the AR exhibits mesoscale frontal wave structures between  
1118 50°-60°S, with an increase in precipitation just off the Antarctica coast at ~65°-67.5°S, Fig. 9e,  
1119 likely arising from the interaction of the low-latitude air mass with the katabatic wind regimeflow  
1120 originating from the Antarctic Plateau, as it is placed at the interface between the two flows (cf.  
1121 Figs. 9a-b with 9d). The low-level convergence of these two air masses can be seen in Fig. 9i  
1122 around 65°S. The katabatic flow is characterized by southerly winds (Fig. 9b) and low  $\theta_E$  values  
1123 (260-270 K, compared to 290-300 K for the low-latitude air mass; Fig. 9c), extending from the  
1124 Antarctic Plateau to the Southern Ocean. At about 50°S at 18 UTC on 13 November, there are two  
1125 propagating atmospheric structures: one moving southwards and reaching Antarctica on 14  
1126 November, and another moving northwards, reaching 40°S at about the same time (Figs. 9a-c). The  
1127 initial AR band breaks into two pieces, with one moving southwards into Antarctica, the one  
1128 discussed here, while the counter clockwise circulation associated with a ridge moving in from the  
1129 west slows down and gradually pushes the northern part equatorwards (cf. Figs. 10a and 10c). A

Formatted: Font: 12 pt

Formatted: Font: 12 pt

Formatted: Font: 12 pt

1130 similar contrasting poleward and equatorward propagation is seen on 15-16 November at about  
1131  $65^{\circ}\text{S}$ , here driven by the interaction of the katabatic winds off Antarctica with the flow around the  
1132 ridge to the east (Figs. 5b and 6e). Figs. 9e-h are as Figs. 9a-d but the fields are averaged over  
1133  $85^{\circ}\text{-}95^{\circ}\text{E}$ . The low-latitude air mass reaches this part of East Antarctica on 15-16 July, when  
1134 precipitation rates exceed  $1.8 \text{ mm w.e. hr}^{-1}$ . The maximum precipitation rate ~~at~~ in coastal Antarctica  
1135 and averaged over  $85^{\circ}\text{-}95^{\circ}\text{E}$  is about 66% higher than that averaged over  $40^{\circ}\text{-}50^{\circ}\text{E}$  ( $1.81 \text{ vs. } 1.09$   
1136  $\text{mm w.e. hr}^{-1}$ ). This can be explained by ~~the~~ (1i) the higher moisture levels (maximum  
1137 longitudinally-averaged  $\theta\text{E}$  values of  $297.9 \text{ K}$  vs.  $289.7 \text{ K}$ ), as the low-latitude air mass penetrates  
1138 further polewards due to a more favourable synoptic pressure pattern, and (H2) a stronger katabatic  
1139 flow off the Antarctic Plateau (maximum longitudinally-averaged meridional wind speed of  $22 \text{ m}$   
1140  $\text{s}^{-1}$  vs.  $19 \text{ ms}^{-1}$ ). Around  $45^{\circ}\text{-}55^{\circ}\text{S}$  on 16 July, AR rapids are present in the plots averaged over  $85^{\circ}\text{-}$   
1141  $95^{\circ}\text{E}$  (pink arrows in Figs. 9e and 9h), when the low-level air intrusion was in the area (Fig. 9j).  
1142 The fact that these structures have been identified in modelling products in the Southern Ocean in  
1143 this study, around Greenland in Box et al. (2023), and in the Middle East in Francis et al. (2024),  
1144 stresses the need for high spatial and temporal resolution three-dimensional radar observations  
1145 along the ARs to check whether they actually exist or are just model artefacts.  
1146



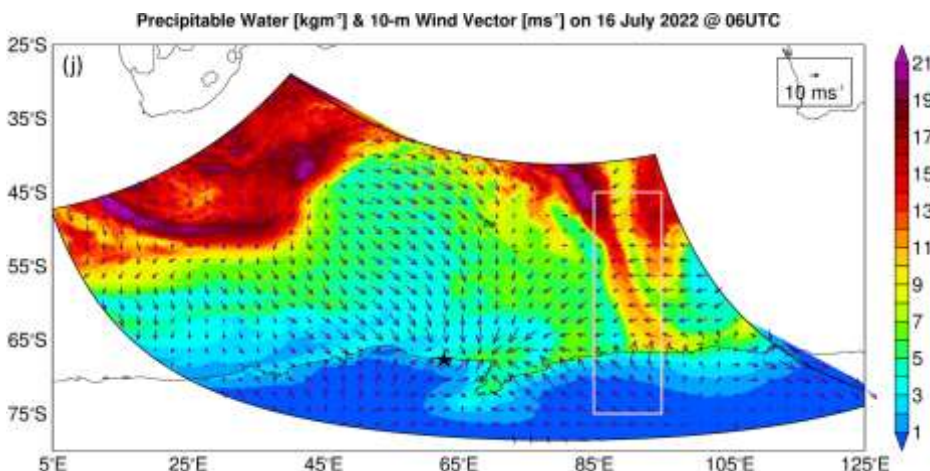
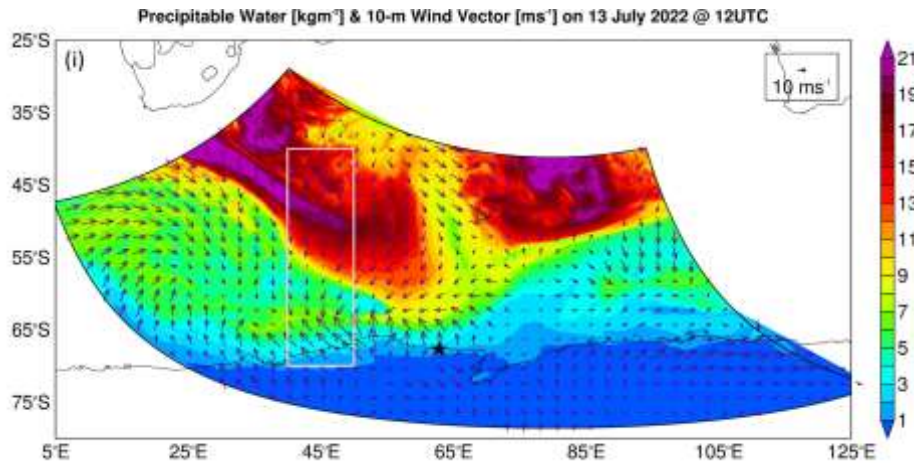


**Figure 9: Hovmöller Plots:** Hovmöller of hourly (a) 700 hPa vertical velocity ( $10^2 \text{ m s}^{-1}$ ), (b) 10-m meridional wind speed ( $\text{m s}^{-1}$ ), (c) 850 hPa equivalent potential temperature ( $\theta_E$ ; K), and (d) precipitation rate ( $\text{mm hr}^{-1}$ ) for 11-16 July 2022 averaged over  $40^{\circ}$ - $50^{\circ}$ E, the core of the AR. The pink arrows highlight AR rapids. (e)-(h) are as (a)-(d) but for the (d) 10-m meridional wind speed ( $\text{m s}^{-1}$ ), (e) 850 hPa equivalent potential temperature (K) and (f) precipitation rate ( $\text{mm hr}^{-1}$ ) averaged over  $85^{\circ}$ - $95^{\circ}$ E, where there is a strong interaction between the low-latitude air mass and the katabatic wind.

flow. The thick blue line in (f) indicates the latitude of the SIMBA site. The grey shading in (e) and (g) highlights latitudes for which the 700 hPa and 850 hPa pressure levels, respectively, are below topography. (i) Precipitable water (shading;  $\text{kg m}^{-2}$ ) and 10-m wind vector (arrows;  $\text{m s}^{-1}$ ) at 12 UTC on 13 July. The star indicates the location of Mawson Station. The fields given in (a)-(d) are averaged over the longitude band of the pink box ( $40^{\circ}$ - $50^{\circ}$ E) and plotted over its latitude range. (j) is as (i) but at 06 UTC on 16 July, with the pink box also giving the latitude range over which the fields in (e)-(h) are plotted, and its longitude band ( $85^{\circ}$ - $95^{\circ}$ E) that used for averaging to generate the hovmöller plots.

1147

1148 On top of surface evaporation from the subtropics (Fig. S2), the convergence of the flow  
1149 around the low-pressure system to the west and the ridge to the east helped feed the AR and  
1150 associated warm and moist air mass (Fig. 7). This can be seen in Figs. 10a-cb. The zonal moisture  
1151 transport in Fig. 10b highlights the convergence of the westerly flow at  $540$ - $105 \text{ m s}^{-1}$  associated  
1152 with equivalent potential temperature ( $\theta_E$ ) values of  $2980$ - $2985 \text{ K}$ , with the and the more moist  
1153 easterly flow around the high with zonal wind speeds in excess of  $20$ - $25 \text{ m s}^{-1}$  and  $\theta_E$  values of-  
1154  $300$ - $290$ - $3050 \text{ K}$ , as this air mass comes directly from the tropics. At about  $65^{\circ}$ E, where the AR is  
1155 located (Fig. 10a), the vertical velocity peaks in the mid-troposphere around  $600$ - $800 \text{ hPa}$  with  
1156 speeds up to  $0.3 \text{ m s}^{-1}$  (Fig. 10c). The vertical structure of the updrafts, with a peak in the low-to-  
1157 mid troposphere, and the updraft speeds are comparable to the AR rapids reported by Box et al.  
1158 (2023) over Greenland on 14 September 2017. Precipitation rates in excess of  $3 \text{ mm hr}^{-1}$  are  
1159 simulated by the model at 12 UTC on 143 July November (Fig. 10d) and at 00 UTC on 15 July (Fig.  
1160 10a) along the AR (Fig. 10a). As the moisture plume moved closer to the Antarctic coast, it  
1161 interacted with the katabatic wind regime. This is evident in Figs. 10e-fd, with the colder, drier ( $\theta_E$   
1162 ~  $260$ - $255$ - $265$ - $280 \text{ K}$ ) and strong (meridional wind speeds in excess of  $450 \text{ m s}^{-1}$ ) airflow from  
1163 Antarctica, which descends the steep slopes with downward vertical velocities down up to  $-0.6 \text{ m}$   
1164  $\text{s}^{-1}$ , converging with the slower ( $350$ - $430 \text{ m s}^{-1}$ ) and more moist ( $\theta_E$  ~  $275$ - $280$ - $285 \text{ K}$ ) flow from  
1165 lower-latitudes with vertical velocities in the bottom 5 km reaching  $+0.3 \text{ m s}^{-1}$ . This convergence  
1166 led to precipitation rates in excess of  $3 \text{ mm hr}^{-1}$  around just north of the Mawson Station (Fig. 10de).  
1167 The pattern of the precipitation field (Figs. 10a and 10e), which has a gap core structure, reflects  
1168 the complex topography of the region (Fig. 1b). The evolution of the interaction between the warm  
1169 and moist southward moving and the colder and drier northward moving air masses is displayed  
1170 in Figs. 9d f, where the meridional wind speed,  $\theta_E$  and precipitation rate are averaged over  $55^{\circ}$   
1171  $65^{\circ}$ E, the band of strong convergence (Fig. 10e). On 12 November, and in particular on 14-15  
1172 November, the strong southerly winds with speeds in excess of  $20 \text{ m s}^{-1}$  converged with, at times,  
1173 an equally strong northerly flow, Fig. 9d, with precipitation around the convergence line, Fig. 9f,  
1174 where  $\theta_E$  values exhibit steep meridional gradients that can exceed  $25 \text{ K}$ , Fig. 9e. The katabatic  
1175 winds on 12 and 14-15 November led to the opening up of a polynya east of the site (Fig. 6a).  
1176 Coastal polynyas are a regular and persistent feature at certain locations around Antarctica owing  
1177 to the steep coastal terrain and topographic channeling of katabatic winds (Barber and Massom,  
1178 2007), with warm and moist air intrusions also playing a role in their spatial extent (Fonseca et al.,  
1179 2023).

1180 The results in Figs. 9d and 10e-d suggest that it can be difficult for ARs and associated warm and  
 1181 moist air intrusions to reach this region of East Antarctica owing to the interaction with the strong  
 1182 katabatic flow. This factor has been highlighted for other regions of East Antarctica (e.g., Terpstra  
 1183 et al., 2021; Gehring et al., 2022).

1184

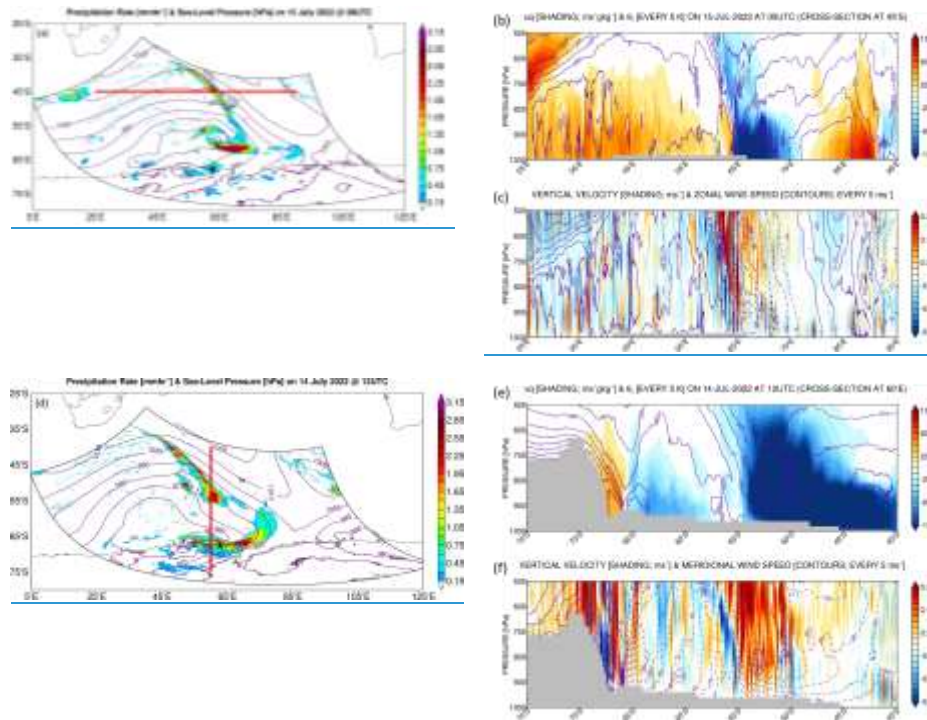


**Figure 10: Precipitation mechanisms in the Southern Ocean:** (a) Precipitation (shading;  $\text{mm hr}^{-1}$ ) and sea-level pressure (contours; hPa) at 0000 UTC on 15 July 2022, from PWRF's 2.5 km grid. (d) Vertical cross-section at 45.5°S, red line in (a), of (b) zonal mass transport (shading;  $\text{m s}^{-1} \text{g kg}^{-1}$ ) and equivalent potential temperature ( $\theta_E$ ; contours; every 5 K) in the top plot, and (c) vertical velocity (shading;  $10^{-2} \text{ m s}^{-1}$ ) and zonal wind speed (contours; every  $5 \text{ m s}^{-1}$ ) in the bottom plot, at the same time. Regions below the orography are shaded in grey. (e)-(f) are as (a)-(c) but at 1200 UTC on 14 July 2022. The cross-section is at 60°E, with the meridional mass transport and meridional wind speed in (e) and (f) the top and bottom plots plotted instead of their zonal counterparts, respectively.

1185

1186 **5. Discussion and Conclusions**

1187 Sea ice is a critically important component of the climate system, modulating atmosphere-  
1188 ocean interactions and ultimately the global climate (Raphael et al., 2011; Goosse et al., 2023).  
1189 The Antarctic SIE has abruptly dropped from 2016 to 2019 (Eayrs et al., 2021; Yang et al., 2021)  
1190 with an all time-record low in 2023, driven by a complex and as yet poorly-understood  
1191 combination of oceanic and atmospheric processes (Wang et al., 2024b). Climate model  
1192 projections indicate major changes in the atmospheric circulation driven by the projected reduction  
1193 in Antarctic sea ice in a warming climate: the Polar Cell and the katabatic flow off the coast of  
1194 Antarctica are projected to strengthen, with a marginal weakening of the Ferrel and Hadley cells,  
1195 and an equatorward shift in the position of the Polar Jet (Tewari et al., 2023). This stresses the  
1196 need for a much-improved understanding of the observed variability of sea-ice properties, such as  
1197 the SIE and SIT that are highly heterogeneous around Antarctica, in order to increase confidence  
1198 in future climate-change projections.

1199  
1200 The SIT at the Khalifa SIMBA site on fast-ice off the Mawson Station largely follows the  
1201 annual solar (seasonal) cycle, with a gradual increase during winter to mid-to-late October  
1202 followed by a steady decline in late spring. The maximum values of ~1.1-1.2 m are in the 0.50-  
1203 1.50 m range estimated from satellite altimeter products for fast-ice in the region around the  
1204 Mawson Station (Li et al., 2022) and are also comparable to the thickness of pack ice around  
1205 Antarctica (Kurtz and Markus, 2012; Kacimi and Kwok, 2020). The ST, on the other hand, is  
1206 highly variable, with values in the range 0.02-0.18 m; these are also consistent with the estimates  
1207 from the satellite altimetry. In contrast to SIT, the temporal variability of ST is strongly linked to  
1208 atmospheric forcing, and in particular to precipitation (snowfall), Foehn effects, blowing snow,  
1209 and episodic warm and moist air intrusions, which can lead to variations of up to ±0.08 m in a day.  
1210 During July-November 2022, an three ARs impacted the site i.e., on 14 July. It led, 13 August and  
1211 14 November to an 18 K increase in air temperature within 24 h. A comparison of reanalysis data  
1212 with in situ observations revealed and a variation of up to 0.046 m in ST due to Foehn effects and  
1213 snowfall (the 0.02 m change in and SIT is within the estimated uncertainty range) in response to  
1214 the ARs in both July and August ARs. The warm and moist air masses associated with ARs have  
1215 a larger impact on sea ice in the colder months, as in the summer the increases in the heat fluxes  
1216 are partially offset by a decrease in the downward shortwave radiation flux (Liang et al., 2023).  
1217 These changes ST and SIT response to the AR occurred within one 12 days of the AR's arrival,  
1218 followed by a recovery to pre-AR levels in the following 12 24 days. However, it is important to  
1219 stress that a longer observational period (than the current 5 month record) would be needed to  
1220 establish more robust and statistically significant links between atmospheric phenomena such as  
1221 Foehn effects, blowing snow, and incursions of warm and moist low-latitude air from low latitudes  
1222 and the coastal SIT and ST (and potentially SIT). In addition, having measurements for at least a  
1223 full year would also allow for the quantification of the potential role of surface melting in ST and  
1224 SIT, which is more likely in the summer months but may occur at other times in a warming climate.  
1225 Simulations with coupled ocean-atmosphere-sea-ice models should also be considered to further

1226 explore the role of atmospheric forcing in ST and SIT. In addition, refined methods to extract SIT  
1227 and ST are desirable, as in particular for SIT, the variation during weather events such as the  
1228 passage of the AR is within the uncertainty range, preventing a clear signal from being extracted  
1229 from the data. The air temperature exhibited a marked increase of up to 18 K within 24 h at the site  
1230 in the case of the 14 July AR, with a less pronounced effect in the summer months (3 K). The in-  
1231 situ snow, sea ice and temperature observations highlight the, at times, strong response in  
1232 particular to ARs impacting the site.

1233  
1234 The 14 JulyNovember AR was particularly intense, with the highest IVT around the Khalifa  
1235 SIMBA site on fast-ice off the Mawson Station of  $\sim 1566 \text{ kg m}^{-1} \text{ s}^{-1}$ , which is in the top 0.5%  
1236 of the climatological distribution. From 14 to 15 November, there is a 0.06 m increase in ST and  
1237 0.04 m increase in SIT, followed by a return to pre-AR levels on 19 November for SIT and 20  
1238 November for ST. The increase in SIT can be explained by the freezing of (some of) the snow on  
1239 top of the sea ice, during a time when the surface and air temperatures were below freezing at the  
1240 site. This AR has its origins in South America, where a wavetrain coming from the Pacific Ocean  
1241 leads to an intensification of the South American Low Level Jet and increased moisture outflow  
1242 into the South Atlantic Ocean. The period 10-19 JulyNovember 2022 is characterized by a  
1243 wavenumber #5 pattern along the subtropical jet and a wavenumber #3 along the polar jet in the  
1244 Southern Hemisphere, the latter projecting into the strong positive SAM phase, with the SAM  
1245 index being more than 1.5 standard deviations above the 1979-2021 climatological mean, in line  
1246 with which is expected given the ongoing La Niña. A pressure dipole, with a low to the west  
1247 and a ridge to the east, promotes the advection of warm and moist low-latitude air across the  
1248 Mawson Station, with the IVT values in the top 1% of the 1979-2021 climatological distribution  
1249 and air temperature anomalies in excess of 8 K or more than two standard deviations above the  
1250 1979-2021 mean in parts of East Antarctica between 0° and 70°E. A back-trajectory analysis  
1251 indicates that contributions from evaporation both in the subtropics and the Southern Ocean  
1252 contributed to the precipitation event on 14 JulyNovember 2022. A more in-depth analysis  
1253 reveals that a secondary low formed just northwest of the site on 134 JulyNovember, driven by  
1254 highly baroclinicity arising from the interaction of the warmer low-latitude air masses with the  
1255 cold katabatic winds that prevail around the Mawson Station. At the same time, a TPV and a jet  
1256 streak at upper-levels contributed to the intensification of the primary low to the west. The  
1257 changing wind field in response to the passage of the deep cyclone, which had a central pressure  
1258 as low as 931 hPa, also has an impact on the sea-ice dynamics. In particular, in the region, with  
1259 maximum pack-ice drift velocities north of Mawson Station exceeded in excess of  $4025 \text{ km day}^{-1}$   
1260 north of the Mawson Station from 124-146 July and  $20 \text{ km day}^{-1}$  from 14-16 JulyNovember, with  
1261 the opening of a polynya in the Southern Ocean northwest of Mawson Station around  $65^{\circ}\text{S}, 45^{\circ}\text{E}$   
1262 from 14 to 22 July. These pack-ice drift speeds are comparable to those estimated during the  
1263 opening of the Maud Rise polynya in September 2017 (Francis et al., 2019), an order of magnitude  
1264 larger than the  $2.5 \text{ km day}^{-1}$  during 12-14 November 2022.

1266 A high-resolution simulation with PWRF down to 2.5 km is conducted to gain further insight  
1267 into this event. An evaluation against *in-situ* observations indicates<sup>4</sup> a good performance for both  
1268 coastal and inland stations in the target region. A dry bias at coastal sites is attributed to an  
1269 excessive offshore wind direction in the model and/or too much boundary layer mixing. An  
1270 evaluation of the simulated vertical profiles against those observed at four coastal sites reveals a  
1271 stronger katabatic flow in PWRF, which is consistent with the drier near-surface conditions. as  
1272 This is reported by other studies (e.g., Vignon et al., 2019), which attributed it to more stable  
1273 boundary layers over the Antarctic Plateau and steeper land-sea synoptic pressure gradients.  
1274 Twile at Syowa Station, for which surface radiation fields are available for evaluation, an  
1275 overunderestimation of the surface upward longwave shortwave radiation flux may be a reflection  
1276 of higher surface temperatures and/or a too higha higherlower surface emissivityalbedo in  
1277 PWRF, the model. Regarding the latter, and for 11–16 November 2022, the surface albedo in PWRF  
1278 is typically 10% lower than that observed. This suggests the need to optimize the land surface  
1279 properties in the modelPWRF, as has been highlighted by other studies (such as Hines et al.,  
1280 2019), which will be left for future work. Ingesting a more realistic representation of the SIE and  
1281 SIT does not translate into higher skill scores for this particular event. This indicates suggests that  
1282 improvements to the boundary layer dynamics and/or land/ice processes, notedhighlighted by  
1283 studies such as Wille et al. (2016, 2017) and Vignon et al. (2019), and at least for this case study  
1284 considered here, are probably more important than having a more accurate sea-ice representation  
1285 in the model. Besides calibrating surface parameters, future PWRF studies should explore other  
1286 physics schemes and/or optimize the tunable parameters defined inside the selected ones, in  
1287 particular in the PBL and land surface model as done for other regions (e.g., Quan et al., 2016;  
1288 Chinta and Balaji, 2020), in an attempt to improve the model performance. In contrast to a  
1289 September 2017 AR over Greenland (Box et al., 2023) and an April 2023 AR in the Arabian  
1290 Peninsula (Franeis et al., 2024), AR rapids are not seen for this particular event. The high-  
1291 resolution PWRFmodel simulations<sup>5</sup> revealed the presence of AR rapids, with a similar vertical  
1292 structure and propagation speed as those reported in Box et al. (2023) over Greenland in September  
1293 2017. The model simulation also highlighted the strong interaction between the air masses around  
1294 the low to the west and the high to the east in the Southern Ocean, as well as the effects of the  
1295 katabatic wind regime in slowing down and weakening the lower-latitude warm and moist air  
1296 incursions as they approach the Antarctic coast. It is this latter interaction that triggers  
1297 precipitation rates in excess of  $3 \text{ mm hr}^{-1}$  around the Mawson Station during 14 July November AR,  
1298 with the precipitation spatial pattern reflecting the complex topography of the region.

1299  
1300 The SIMBA deployment at a fast-ice site off the Mawson Station during July–November 2022  
1301 enabled a better understanding of the spatial and temporal variability of SIT and ST in that part of  
1302 coastal East Antarctica. Such measurements should also be conducted at other sites given the  
1303 marked regional differences in sea-ice properties in the Southern Ocean (Parkinson and Cavalieri,  
1304 2012). This will also help to evaluate and improve the ST, SIE and SIT estimates derived and key  
1305 products from satellite remote sensing assets and numerical models. Besides ocean dynamics and

1306 thermodynamics, the findings of the study stress the role of atmospheric forcing in driving ~~in particular the ST~~the variability of ST in particular. Long-term measurements are needed to further  
1307 explore ~~and quantify~~ how Foehn effects, blowing snow, -warm and moist air intrusions, and surface  
1308 melting modulate ~~the~~ SIT (~~not just the SIE~~) and ST, and how they respond to seasonal and inter-  
1309 annual variations in the atmospheric and oceanic state. This is a crucial step to improving the  
1310 quality and confidence of future ~~climate-climate~~-change projections and medium- and long-range  
1311 weather forecasts owing to the global effects influence of sea-ice variability on the climate system.  
1312  
1313

## 1314 Acknowledgements

1315 This work was funded by Khalifa University Polar Research Center. The authors wish to  
1316 acknowledge the contribution of Khalifa University's high-performance computing and research  
1317 computing facilities to the results of this research. The SIMBA deployment at a fast-ice site off  
1318 ~~the~~-Mawson Station, *in-situ* measurements and the technical assistance were supported under  
1319 Australian Antarctic Science [AAS] project #4506 (CI: P. Heil). The work of P. Heil and R.  
1320 Massom was supported by the Australian Antarctic Division. For R. Massom, this work was also  
1321 supported by the Australian Research Council Special Research Initiative the Australian Centre  
1322 for Excellence in Antarctic Science (Project Number SR200100008). PH acknowledges support  
1323 from the AAS Program (AAS4496, AAS4506, AAS4625) and grant funding from the International  
1324 Space Science Institute (Switzerland; Project 405) and the Swiss Federal Research Fellowship  
1325 program. This For P. Heil and R. Massom, this work contributes to Project 6 of the Australian  
1326 Antarctic Program Partnership (ASCI000002) funded under the Australian Government's  
1327 Antarctic Science Collaboration Initiative program. We are also grateful for the Byrd Polar and  
1328 Climate Research Center at The Ohio State University for developing and maintaining PolarWRF  
1329 and making it freely available to the scientific community. We greatly appreciate the support of  
1330 the Automatic Weather Station Program and the Antarctic Meteorological Research Center for the  
1331 weather station data used in this study (National Science Foundation grants numbers ARC-  
1332 0713843, ANT-0944018, and ANT-1141908). The authors also gratefully acknowledge the  
1333 National Oceanic and Atmospheric Administration Air Resources Laboratory for the provision of  
1334 the Hybrid Single-Particle Lagrangian Integrated Trajectory (HYSPLIT) transport and dispersion  
1335 model used in this work. We would like to thank the editor and two anonymous reviewers for their  
1336 insightful and constructive comments and suggestions that helped to substantially improve the  
1337 quality of this work.  
1338

## 1339 Code/Data availability

1340 The sea-ice and snow thickness measurements at the Khalifa SIMBA site on fast-ice off ~~the~~  
1341 Mawson Station for July-November 2022 are available upon request from the corresponding

1342 author (Diana Francis; [diana.francis@ku.ac.ae](mailto:diana.francis@ku.ac.ae)). The remaining observational and the reanalysis  
1343 datasets used in this study are freely available online: (i) ERA-5 reanalysis data were downloaded  
1344 from the Copernicus Climate Data Store website (Hersbach et al., 2023a,b); (ii) Automatic  
1345 Weather Station (AWS) data at the Mawson, [Davis, and Casey](#) Stations can be requested at the  
1346 Australian Antarctic Data Center website (AADC, 2022); (iii) AWS and surface radiation data for  
1347 Syowa Station were obtained from the World Radiation Monitoring Center - Baseline Surface  
1348 Radiation Network website (AWI, 2024); (iv) AWS data for the [Mizuho and Relay](#) Stations  
1349 ~~wasere~~ extracted from the Antarctic Meteorological Research Center & Automatic Weather  
1350 Stations Project (Lazzara, 2024); ~~(v) true colour visible daily satellite images from the~~  
1351 ~~measurements collected by the Moderate Resolution Imaging Spectroradiometer instrument~~  
1352 ~~onboard the Terra satellite were accessed on the National Aeronautics and Space Administration's~~  
1353 ~~Worldview website (Boller, 2024)~~; (vi) sea-ice velocity vectors from the low resolution sea-ice  
1354 drift product are available at the European Organization for the Exploitation of Meteorological  
1355 Satellites (EUMETSAT) Ocean and Sea Ice Satellite Application Facility (EUMETSAT, 2024);  
1356 (vii) sea-ice concentration maps derived from the measurements collected ~~by the Advanced~~  
1357 ~~Microwave Scanning Radiometer (AMSR) for Earth Observing Systems instrument onboard the~~  
1358 ~~National Aeronautics and Space Administrations (NASA) Aqua satellite and the AMSR-2~~  
1359 ~~instrument onboard the Japan Aerospace and Exploration Agency by the Advanced Mierowave~~  
1360 ~~Scanning Radiometer 2 instrument onboard the Japan Aerospace and Exploration Agency~~ Global  
1361 Change Observation Mission 1<sup>st</sup>-Water "Shizuku" satellite from January 2013 to present, were  
1362 obtained from the University of Bremen website (UoB; 2024); (viii) [twice daily atmospheric](#)  
1363 sounding profiles ~~at thefrom Mawson, Syowa, Davis, and Casey~~ Stations were accessed at the  
1364 University of Wyoming website (Oolman, 20254). The Hybrid Single-Particle Lagrangian  
1365 Integrated Trajectory (HYSPLIT) transport and dispersion model is downloaded from the National  
1366 Aeronautic and Space Administration Air Resources Laboratory website (NOAA ARL, 2024). The  
1367 PolarWRF model version 4.3.3 is available at the Byrd Polar and Climate Research Center at The  
1368 Ohio State University website (PWRF, 2024). The figures presented in this manuscript have been  
1369 generated with the Interactive Data Language (IDL; Bowman, 2005) and MATLAB (Mathworks,  
1370 2024) software.

1371  
1372 **Competing interests**  
1373 One co-author is a member of The Cryosphere editorial board.  
1374  
1375

1376 **Author Contributions: CRediT**  
1377 **DF**: Conceptualization of the study, Interpretation and validation of the results, Writing the draft,  
1378 Funding Acquisition; **RF**: Formal analysis, Data processing and analysis of the results, Writing  
1379 the draft; **NN**: Data acquisition, processing and analysis, Interpretation of the results, Inputs to the

1380 manuscript; **PH**: Interpretation of the results, Inputs to the manuscript; **JDW**: Interpretation of the  
1381 results, Inputs to the manuscript; **IVG**: Interpretation of the results, Inputs to the manuscript;  
1382 **RAM**: Interpretation of the results, Inputs to the manuscript. All authors interpreted the results and  
1383 provided input to the final manuscript.

1384

## 1385 **References**

1386 AADC (2022) Antarctic Climate Data Collected by Australian Agencies. Australian Antarctic Data Center  
1387 [Dataset]. Accessed on 22 April 2024, available online at [Australian Antarctic Data Centre \(aad.gov.au\)](https://aad.gov.au).

1388

1389 Alapaty, K., Herwehe, J. A., Otte, T. L., Nolte, C. G., Bullock, O. R., Mallard, M. S., Kain, J. S., Dudhia,  
1390 J. (2012) Introducing subgrid-scale cloud feedbacks to radiation for regional meteorological and climate  
1391 modeling. *Geophysical Research Letters*, 39, L24809. <https://doi.org/10.1029/2012GL054031>

1392

1393 Attada, R., Kunchala, R. K., Dasari, H. P., Sivareddy, S., Yesubabu, V., Knio, O., Hoteit, I. (2021) Representation of Arabian Peninsula summer climate in a regional atmospheric model using spectral  
1394 nudging. *Theoretical and Applied Climatology*, 145, 13-30. <https://doi.org/10.1007/s00704-021-03617-w>

1395

1396

1397 AWI (2024). WRMC-BSRN: World Radiation Monitoring Center - Baseline Surface Radiation Network  
1398 [Dataset]. Accessed on 15 April 2024, available online at <https://bsrn.awi.de/>.

1399

1400 Barber, D. G., Massom, R. A. (2007) The Role of Sea Ice in Arctic and Antarctic Polynyas. In W. O. Smith  
1401 and D. G. Barber (Editors), *Polynyas: Windows to the World's Oceans*, pp. 1-54. Elsevier. Amsterdam.

1402

1403 *Beller, R. (2024) National Aeronautics and Space Administration (NASA) Worldview. Accessed on 15*  
1404 *May 2024, available online at <https://worldview.earthdata.nasa.gov/>*

1405

1406 Bowman, K. P. (2005) An Introduction to Programming with IDL: Interactive Data Language [Software].  
1407 Academic Press, 304 pp.. ISBN-10: 012088559X, ISBN-13: 978-0120885596.

1408

1409 Box, J. E., Nielsen, K. P., Yang, X., Niwano, M., Wehrle, A., van As, D., Fettweis, X., Koltzow, M. A. O.,  
1410 Palmason, B., Fausto, R. S., van den Broeke, M. R., Huai, B., Ahlstrom, A. P., Langley, K., Dachauer, A.,  
1411 Noel, B. (2023) Greenland ice sheet rainfall climatology, extremes and atmospheric river rapids.  
1412 *Meteorological Applications*, 30, e2134. <https://doi.org/10.1002/met.2134>

1413

1414 Bozkurt, D., Rondanelli, R., Marin, J. C., Garreaud, R. (2018) Foehn event triggered by an atmospheric  
1415 river underlies record-setting temperature along continental Antarctica. *Journal of Geophysical Research:*  
1416 *Atmospheres*, 123, 3871-3892. <https://doi.org/10.1002/2017JD027796>

1417

1418 Bromwich, D. H., Otieno, F. O., Hines, K. M., Manning, K. W., Shilo, E. (2013) Comprehensive evaluation  
1419 of polar weather research and forecasting model performance in the Antarctic. *Journal of Geophysical*  
1420 *Research: Atmospheres*, 118, 274-292. <https://doi.org/10.1029/2012JD018139>

1421

1422 Bromwich, D. H., Powers, J. G., Manning, K. W., Zou, X. (2022) Antarctic data impact experiments with  
1423 Polar WRF during the YOPP-SH summer special observing period. *Quarterly Journal of the Royal*  
1424 *Meteorological Society*, 148, 2194-2218. <https://doi.org/10.1002/qj.4298>

1425

1426 Chen, F., Dudhia, J. (2001) Coupling an Advanced Land Surface-Hydrology Model with the Penn State -  
1427 NCAR MM5 Modeling System. Part I: Model Implementation and Sensitivity. *Monthly Weather Review*,  
1428 129, 569-585. [https://doi.org/10.1175/1520-0493\(2001\)129<0569:CAALSH>2.0.CO;2](https://doi.org/10.1175/1520-0493(2001)129<0569:CAALSH>2.0.CO;2)

1429

1430 [Chinta, S., Balaji, C. \(2020\) Calibration of WRF model parameters using multiobjective adaptive surrogate](#)  
1431 [model-based optimization to improve the prediction of the Indian summer monsoon. \*Climate Dynamics\*,](#)  
1432 [55, 631-650. https://doi.org/10.1007/s00382-020-05288-1](#)

1433

1434 Dare, R. A., Budd, W. F. (2001) Analysis of Surface Winds at Mawson, Antarctica. *Weather and*  
1435 *Forecasting*, 16, 416-431. [https://doi.org/10.1175/1520-0434\(2001\)016<0416:AOSWAM>2.0.CO;2](https://doi.org/10.1175/1520-0434(2001)016<0416:AOSWAM>2.0.CO;2)

1436

1437 Djoumna, G., Holland, D. M. (2021) Atmospheric rivers, warm air intrusions, and surface radiation balance  
1438 in the Amundsen Sea Embayment. *Journal of Geophysical Research: Atmospheres*, 126, e2020JD034119.  
1439 <https://doi.org/10.1029/2020JD034119>

1440

1441 [Dery, S. J., Yau, M. K. \(2002\) Large-scale mass balance effects of blowing snow and surface sublimation.](#)  
1442 [Journal of Geophysical Research, 107, 4679. https://doi.org/10.1029/2001JD001251](#)

1443

1444 Dong, X., Wang, Y., Hou, S., Ding, M., Yin, B., Zhang, Y. (2020) Robustness of the Recent Global  
1445 Atmospheric Reanalyses for Antarctic Near-Surface Wind Speed Climatology. *Journal of Climate*, 33,  
1446 4027-4043. <https://doi.org/10.1175/JCLI-D-19-0648.1>

1447

1448 Eayrs, C., Holland, D. M., Francis, D., Wagner, T. J. W., Kumar, R., Li, X. (2019) Understanding the  
1449 seasonal cycle of Antarctic sea ice extent in the context of long-term variability. *Reviews of Geophysics*,  
1450 57, 1037-1064. <https://doi.org/10.1029/2018RG000631>

1451

1452 Eayrs, C., Li, X., Raphael, M. N., Holland, D. M. (2021) Rapid decline in Antarctic sea ice in recent years  
1453 hints at future change. *Nature Geosciences*, 14, 460-464. <https://doi.org/10.1038/s41561-021-00768-3>

1454

1455 Elvidge, A. D., Munneke, K., King, P., Renfrew, I. A., Gilbert, E. (2020) Atmospheric drivers of melt on  
1456 Larsen C Ice Shelf: Surface energy budget regimes and the impact of foehn. *Journal of Geophysical*  
1457 *Research: Atmospheres*, 125, e2020JD032463. <https://doi.org/10.1029/2020JD032463>

1458

1459 [England, M. R., Wagner, T. J. W., Eisenman, I. \(2020\) Modeling the breakup of tabular icebergs. \*Science\*](#)  
1460 [Advances](#), 6, 51. <https://doi.org/10.1126/sciadv.abd1273>

1461

1462 EUMETSAT (2024) Ocean and Sea Ice Satellite Application Facility. Accessed on 12 August 2024,  
1463 available online at <https://osi-saf.eumetsat.int/products/osi-405-c>

1464

1465 Feng, Z., Leung, L. R., Liu, N., Wang, J., Houze, R. A. Jr., Li, J., Hardin, J. C., Chen, D., Guo, J. (2021) A  
1466 global high-resolution mesoscale convective system database using satellite-derived cloud tops, surface  
1467 precipitation, and tracking. *Journal of Geophysical Research: Atmospheres*, 126, e2020JD034202.  
1468 <https://doi.org/10.1029/2020JD034202>

1469

1470 Finlon, J. A., Rauber, R. M., Wu, W., Zaremba, T. J., McFarquhar, G. M., Nesbitt, S. W., Schnaiter, M.,  
1471 Jarvinen, E., Waitz, F., Hill, T. C. J., DeMott, P. J. (2020) Structure of an atmospheric river over Australia  
1472 and the Southern Ocean: II. Microphysical evolution. *Journal of Geophysical Research: Atmospheres*, 125,  
1473 e2020JD032514. <https://doi.org/10.1029/2020JD032514>

1474

1475 Fons, S., Kurtz, N., Bagnardi, M. (2023) A decade-plus of Antarctic sea ice thickness and volume estimates  
1476 from CryoSat-2 using a physical model and waveform fitting. *The Cryosphere*, 17, 2487-2508.  
1477 <https://doi.org/10.5194/tc-17-2487-2023>

1478

1479 Fonseca, R., Francis, D., Aulicino, G., Mattingly, K., Fusco, G., Budillon, G. (2023) Atmospheric controls  
1480 on the Terra Nova Bay polynya occurrence in Antarctica. *Climate Dynamics*, 61, 5147-5169.  
1481 <https://doi.org/10.1007/s00382-023-06845-0>

1482

1483 Francis, D., Eayrs, C., Cuesta, J., Holland, D. (2019) Polar cyclones at the origin of the reoccurrence of the  
1484 Maud Rise Polynya in austral winter 2017. *Journal of Geophysical Research: Atmospheres*, 124, 5251-  
1485 5267. <https://doi.org/10.1029/2019JD030618>

1486

1487 Francis, D., Fonseca, R., Bozkurt, D., Nelli, N., Guan, B. (2024) Atmospheric River Rapids and Their Role  
1488 in the Extreme Rainfall Event of April 2023 in the Middle East. *Geophysical Research Letters*, 51,  
1489 e2024GL109446. <https://doi.org/10.1029/2024GL109446>

1490

1491 Francis, F., Fonseca, R., Mattingly, K. S., Lhermitte, S., Walker, C. (2023) Foehn winds at Pine Island  
1492 Glacier and their role in ice changes. *The Cryosphere*, 17, 3041-3062. <https://doi.org/10.5194/tc-17-3041-2023>

1492

1493

1494 Francis, D., Fonseca, R., Nelli, N., Bozkurt, D., Picard, G., Guan, B. (2022a) Atmospheric rivers drive  
1495 exceptional Saharan dust transport towards Europe. *Atmospheric Research*, 266, 105959.  
1496 <https://doi.org/10.1016/j.atmosres.2021.105959>

1497

1498 Francis, D., Mattingly, K. S., Lhermitte, S., Temimi, M., Heil, P. (2021) Atmospheric extremes caused high  
1499 oceanward sea surface slope triggering the biggest calving event in more than 50 years at the Amery Ice  
1500 Shelf. *The Cryosphere*, 15, 2147-2165. <https://doi.org/10.5194/tc-15-2147-2021>

1501

1502 Francis, D., Fonseca, R., Mattingly, K. S., Marsh, O. J., Lhermitte, S., Cherif, C. (2022b) Atmospheric  
1503 triggers of the Brunt Ice Shelf calving in February 2021. *Journal of Geophysical Research: Atmospheres*,  
1504 127, e2021JD036424. <https://doi.org/10.1029/2021JD036424>

1505

1506

1507 Francis, D., Mattingly, K. S., Temimi, M., Massom, R., Heil, P. (2020) On the crucial role of atmospheric  
1508 rivers in the two major Weddell Polynya events in 1973 and 2017 in Antarctica. *Science Advances*, 6.  
1509 <https://doi.org/10.1126/sciadv.abc2695>

1510

1511 Fraser, A. D., Wongpan, P., Langhorne, P. J., Klekociuk, A. R., Kusahara, K., Lannuzel, D., Massom, R.  
1512 A., Meiners, K. M., Swadling, K. M., Atwater, D. P., Brett, G. M., Corkill, M., Dalman, L. A., Fiddes, S.,  
1513 Granata, A., Guglielmo, L., Heil, P., Leonard, G. H., Mahoney, A. R., McMinn, A., van der Merwe, P.,  
1514 Weldrick, C. K., Wienecke, B. (2023) Antarctic landfast sea ice: A review of its physics, biogeochemistry  
1515 and ecology. *Reviews of Geophysics*, 61, e2022RG000770. <https://doi.org/10.1029/2022RG000770>

1516

1517 Gehring, J., Vignon, E., Billault-Roux, A. C., Ferrone, A., Protat, A., Alexander, S. P., Berne, A. (2022)  
1518 Orographic flow influence on precipitation during an atmospheric river event at Davis, Antarctica. *Journal  
1519 of Geophysical Research: Atmospheres*, 127, e2021JD035210. <https://doi.org/10.1029/2021JD035210>.

1520

1521 Gelaro, R., McCarty, W., Suarez, M. J., Todling, R., Molod, A., Takacs, L., Randles, C. A., Darmenov, A.,  
1522 Bosilovich, M. G., Reichle, R., Wargan, K., Coy, L., Cullather, R., Draper, C., Akella, S., Buehard, V.,  
1523 Conaty, A., da Silva, A. M., Gu, W., Kim, G. K., Koster, R., Lucchesi, R., Merkova, D., Nielsen, J. E.,  
1524 Partyka, G., Pawson, S., Putman, W., Rienecker, M., Schubert, S. D., Sienkiewicz, M., Zhao, B. (2017)  
1525 The Modern Era Retrospective Analysis for Research and Applications, Version 2 (MERRA-2). *Journal of  
1526 Climate*, 30, 5419–5454. <https://doi.org/10.1175/JCLI-D-16-0758.1>

1527

1528 Ghiz, M.L., Scott, R. C., Vogelmann, A. M., Lenaerts, J. T. M., Lazzara, M., Lubin, D. (2021) Energetics  
1529 of surface melt in West Antarctica. *The Cryosphere*, 15, 3459–3494. [https://doi.org/10.5194/tc-15-3459-2021](https://doi.org/10.5194/tc-15-3459-<br/>1530 2021)

1531

1532 Gilbert, E., Pishniak, D., Torres, J. A., Orr, A., MacLennan, M., Wever, N., Verro, K. (2025) Extreme  
1533 precipitation associated with atmospheric rivers over West Antarctic ice shelves: insights from the  
1534 kilometre-scale regional climate modeling. *The Cryosphere*, 19, 597–618. [https://doi.org/10.5194/tc-19-597-2025](https://doi.org/10.5194/tc-19-<br/>1535 597-2025)

1536

1537 Goosse, H., Contador, A., Bitz, C., Blanchard-Wrigglesworth, C. M., Eayrs, E., Fichefet, C., Himmich, T.,  
1538 Huot, K., Klein, P.-V., Marchi, F., Massonnet, S., Mezzina, F., Pelletier, B., Roach, C., Vancoppenolle, L.,  
1539 van Lipzig, N. P. M. (2023) Modulation of the seasonal cycle of the Antarctic sea ice extent by sea ice  
1540 processes and feedbacks with the ocean and the atmosphere. *The Cryosphere*, 17, 407–425.  
1541 <https://doi.org/10.5194/tc-17-407-2023>

1542

1543 Gorodetskaya, I. V., Duran-Alarcon, C., Gonzalez-Herrero, S., Clem, K. R., Zou, X., Rowe, P., Imazio, P.  
1544 R., Campos, D., Leroy-Dos Santos, C., Dutrievoz, N., Wille, J. D., Chyhareva, A., Favier, V., Blanchet, J.,  
1545 Pohl, B., Cordero, R. R., Prak, S.-J., Colwell, S., Lazzara, M. A., Carrasco, J., Gulisano, A. M., Krakovska,  
1546 S., Ralph, F. M., Dethinne, T., Picard, G. (2023) Record-high Antarctic Peninsula temperatures and surface  
1547 melt in February 2022: a compound event with an intense atmospheric river. *Npj Climate and Atmospheric  
1548 Science*, 6, 202. <https://doi.org/10.1038/s41612-023-00529-6>

1549

1550 Gorodetskaya, I. V., Silva, T., Schmithusen, H., Hirasawa, N. (2020) Atmospheric river signatures in  
1551 radiosonde profiles and reanalyses at the Dronning Maud Land Coast, East Antarctica. *Advances in*  
1552 *Atmospheric Sciences*, 37, 455-476. <https://doi.org/10.1007/s00376-020-9221-8>

1553

1554 Gorodetskaya, I. V., Van Lipzig, N. P. M., Van den Broeke, M. R., Mangold, A., Boot, W., Reijmer, C. H.  
1555 (2013) Meteorological regimes and accumulation patterns at Utsteinen, Dronning Maud Land, East  
1556 Antarctica: Analysis of two contrasting years. *Journal of Geophysical Research: Atmospheres*, 118, 1700-  
1557 1715. <https://doi.org/10.1002/jgrd.50177>

1558

1559 Gossart, A., Helsen, S., Lenaerts, J. T. M., Vanden Broucke, S., van Lipzig, N. P. M., Souverijns, N. (2019)  
1560 An Evaluation of Surface Climatology in State-of-the-Art Reanalyses over the Antarctic Ice Sheet. *Journal*  
1561 *of Climate*, 32, 6899-6915. <https://doi.org/10.1175/JCLI-D-19-0030.1>

1562

1563 Guest, P. S. (2021) Inside katabatic winds over the Terra Nova Bay polynya: 2. Dynamic and  
1564 thermodynamic analyses. *Journal of Geophysical Research: Atmospheres*, 126, e2021JD034904.  
1565 <https://doi.org/10.1029/2021JD034904>

1566

1567 ~~Gumley, L., Deselotries, J., Schmaltz, J. (2010) Creating Reprojected True Color MODIS Images: A  
1568 Tutorial. Accessed on 23 October 2024, available online at <https://www.earthdata.nasa.gov/s3fs-public/2022-02/MODIS-True-Color.pdf>~~

1570

1571 Haas, C. (2017) Sea ice thickness distribution. In: *Sea Ice*, D. N. Thomas (Ed.). Blackwell Science.  
1572 <https://doi.org/10.1002/9781118778371.ch2>

1573

1574 ~~Hart, N. C. G., Reason, C. J. C., Fauchereau, N. (2013) Cloud bands over southern Africa: seasonality,  
1575 contribution to rainfall variability and modulation by the MJO. *Climate Dynamics*, 41, 1199-1212.  
1576 <https://doi.org/10.1007/s00382-012-1589-4>~~

1577

1578 ~~Hines, K. M., Bromwich, D. H., Wang, S. H., Silber, I., Verlinde, J., Lubin, D. (2019) Microphysics of  
1579 summer clouds in central West Antarctica simulated by the Polar Weather Research and Forecasting Model  
1580 (PWRF) and the Antarctic Mesoscale Prediction System. *Atmospheric Chemistry and Physics*, 19, 12431-  
1581 12454. <https://doi.org/10.5194/acp-19-12431-2019>~~

1582

1583 Haumann, F. A., Gruber, N., Munnich, M., Frenger, I., Kern, S. (2016) Sea-ice transport driving Southern  
1584 Ocean salinity and its recent trends. *Nature*, 537, 89-92. <https://doi.org/10.1038/nature19101>

1585

1586 Heil, P. (2006) Atmospheric conditions and fast ice at Davis, East Antarctica: A case study. *Journal of*  
1587 *Geophysical Research*, 111, C05009. <https://doi.org/10.1029/2005JC002904>

1588

1589 Heil, P., Allison, I., Lytle, V. I. (1996) Seasonal and interannual variations of the oceanic heat flux under a  
1590 landfast Antarctic sea ice cover. *Journal of Geophysical Research*, 101(C11), 25741-25752.  
1591 <https://doi.org/10.1029/96JC01921>

1592

1593 Hersbach, H., Bell, B., Berrisford, P., Biavati, G., Horanyi, A., Munoz Sabater, J., Nicolas, J., Peavey, C.,  
1594 Radu, R., Rozum, I., Schepers, D., Simmons, A., Soci, C., Dee, D., Thepaut, J.-N. (2023a) ERA5 hourly  
1595 data on single levels from 1940 to present [Dataset]. Copernicus Climate Change Service (C3S) Climate  
1596 Data Store (CDS). Accessed on 22 April 2024, available online at <https://doi.org/10.24381/cds.adbb2d47>  
1597

1598 Hersbach, H., Bell, B., Berrisford, P., Biavati, G., Horanyi, A., Munoz Sabater, J., Nicolas, J., Peavey, C.,  
1599 Radu, R., Rozum, I., Schepers, D., Simmons, A., Soci, C., Dee, D., Thepaut, J.-N. (2023b) ERA5 hourly  
1600 data on pressure levels from 1940 to present [Dataset]. Copernicus Climate Change Service (C3S) Climate  
1601 Data Store (CDS). Accessed on 22 April 2024, available online at <https://doi.org/10.24381/cds.bd0915c6>  
1602

1603 Hersbach, H., Bell, B., Berrisford, P., Hirahara, S., Horanyi, A., Munoz-Sabater, J., Nicolas, J., Peavey, C.,  
1604 Radu, R., Schepers, D., Simmons, A., Soci, C., Abdalla, S., Abellán, X., Balsamo, G., Bechtold, P., Biavati,  
1605 G., Bidiot, J., Bonavita, M., De Chiara, G., Dahlgren, P., Dee, D., Diamantakis, M., Dragani, R., Fleming,  
1606 J., Forbes, R., Fuentes, M., Geer, A., Haimberger, L., Healy, S., Hogan, R. J., Holm, E., Janiskova, M.,  
1607 Keeley, S., Laloyaux, P., Lopez, P., Lulu, C., Radnoti, G., de Rosnay, P., Rozum, I., Vamborg, F., Villaume,  
1608 S., Thepaut, J.-N. (2020) The ERA5 global reanalysis. Quarterly Journal of the Royal Meteorological  
1609 Society, 146, 1999-2049. <https://doi.org/10.1002/qj.3803>  
1610

1611 Hines, K. M., Bromwich, D. H., Silber, I., Russell, L. M., Bai, L. (2021) Predicting frigid mixed-phase  
1612 clouds for pristine coastal Antarctica. Journal of Geophysical Research: Atmospheres, 126,  
1613 e2021JD035112. <https://doi.org/10.1029/2021JD035112>  
1614

1615 Hines, K. M., Bromwich, D. H., Wang, S.-H., Silber, I., Verlinde, J., Lubin, D. (2019) Microphysics of  
1616 summer clouds in central West Antarctica simulated by the Polar Weather Research and Forecasting Model  
1617 (WRF) an the Antarctic Mesoscale Prediction System (AMPS). Atmospheric Chemistry and Physics, 19,  
1618 12431-12454. <https://doi.org/10.5194/acp-19-12431-2019>  
1619

1620 Hobbs, W., Spence, P., Meyer, A., Schroeter, S., Fraser, A. D., Reid, P., Tian, R. T., Wang, Z., Liniger, G.,  
1621 Doddridge, E. W., Boyd, P. W. (2024) Observational Evidence for a Regime Shift in Summer Antarctic  
1622 Sea Ice. Journal of Climate, 37, 2263-2275. <https://doi.org/10.1175/JCLI-D-23-0479.1>  
1623

1624 Hoppmann, M., M. Nicolaus, P. A. Hunkeler, P. Heil, L.-K. Behrens, G. König-Langlo, R. Gerdes (2015)  
1625 Seasonal evolution of an ice-shelf influenced fast-ice regime, derived from an autonomous thermistor chain.  
1626 *Journal of Geophysical Research: Oceans*, 120, 1703–1724, <https://doi.org/10.1002/2014JC010327>.  
1627

1628 Hoskins, B., Fonseca, R., Blackburn, M., Jung, T. (2012) Relaxing the Tropics to an ‘observed’ state:  
1629 analysis using a simple baroclinic model. Quarterly Journal of the Royal Meteorological Society, 138, 1618-  
1630 1626. <https://doi.org/10.1002/qj.1881>  
1631

1632 Hoskins, B. J., Karoly, D. J. (1981) The Steady Linear Response of a Spherical Atmosphere to Thermal  
1633 and Orographic Forcing. *Journal of Atmospheric Sciences*, 38, 1179-1196. [https://doi.org/10.1175/1520-0469\(1981\)038<1179:TSLROA>2.0.CO;2](https://doi.org/10.1175/1520-0469(1981)038<1179:TSLROA>2.0.CO;2)  
1634  
1635

1636 Hoskins, B. J., Valdes, P. J. (1990) On the Existence of Storm-Tracks. *Journal of Atmospheric Sciences*,  
1637 47, 1854-1864. [https://doi.org/10.1175/1520-0469\(1990\)047<1854:OTEOST>2.0.CO;2](https://doi.org/10.1175/1520-0469(1990)047<1854:OTEOST>2.0.CO;2)

1638

1639 Houze, R. A. Jr. (2004) Mesoscale convective systems. *Reviews of Geophysics*, 42, RG4003.  
1640 <https://doi.org/10.1029/2004RG000150>

1641

1642 Hu, H., Zhao, J., Heil, P., Qin, Z., Ma, J., Hui, F., Cheng, X. (2023) Annual evolution of the ice-ocean  
1643 interaction beneath landfast ice in Prydz Bay, East Antarctica. *The Cryosphere*, 17, 2231-2244.  
1644 <https://doi.org/10.5194/tc-17-2231-2023>

1645

1646 Iacono, M. J., Delamere, J. S., Mlawer, E. J., Shephard, M. W., Clough, S. A., & Collins, W. D. (2008)  
1647 Radiative forcing by long-lived greenhouse gasses: Calculations with the AER radiative transfer models.  
1648 *Journal of Geophysical Research*, 113, D13103. <https://doi.org/10.1029/2008JD009944>

1649

1650 Jackson, K., J. Wilkinson, T. Maksym, D. Meldrum, J. Beckers, C. Haas, and D. Mackenzie (2013) A Novel  
1651 and Low Cost Sea Ice Mass Balance Buoy. *Journal of Atmospheric and Oceanic Technology*, 30, 2676-  
1652 2688. <https://doi.org/10.1175/JTECH-D-13-00058.1>

1653

1654 Kacimi, S., Kwok, R. (2020) The Antarctic sea ice cover from ICESat-2 and CryoSat-2: freeboard, snow  
1655 depth, and ice thickness. *The Cryosphere*, 14, 4453-4474. <https://doi.org/10.5194/tc-14-4453-2020>

1656

1657 Kain, J. S. (2004) The Kain-Fritsch convective parameterization: An update. *Journal of Applied  
1658 Meteorology*, 43, 170-181. [https://doi.org/10.1175/1520-0430\(2004\)043<0170:tkcpau>2.0.co;2](https://doi.org/10.1175/1520-0430(2004)043<0170:tkcpau>2.0.co;2)

1659

1660 Kawamura, T., Takizawa, T., Ohshima, K. I., Ushio, S. (1995) Data of sea-ice cores obtained in Lutzow-  
1661 Holm Bay from 1990 to 1992 (JARE-31, -32) in the period of Japanese Antarctic climate research. JARE  
1662 Data Rep. 204 (Glaciol. 24), 42 pp., National Institute of Polar Research, Tokyo.

1663

1664 Koh, T.-Y., Wang, S., Bhatt, B. C. (2012) A diagnostic suite to assess NWP performance. *Journal of  
1665 Geophysical Research*, 117, D13109. <https://doi.org/10.1029/2011JD017103>

1666

1667 Kurtz, N. T., Markus, T. (2012) Satellite observations of Antarctic sea ice thickness and volume. *Journal  
1668 of Geophysical Research*, 117, C08025. <https://doi.org/10.1029/2012JC008141>

1669

1670 [Lapere, R., Thomas, J. L., Favier, V., Angot, H., Asplund, J., Ekman, A. M. L., Marelle, L., Raut, J. P., Da  
1671 Silva, A., Wille, J. D., Zieger, P. \(2024\) Polar aerosol atmospheric rivers: Detection, characteristics, and  
1672 potential applications. \*Journal of Geophysical Research: Atmospheres\*, 129, e2023JD039606.  
1673 <https://doi.org/10.1029/2023JD039606>.](https://doi.org/10.1029/2023JD039606)

1674

1675 Lavergne, T., Eastwood, S., Teffah, Z., Schuberg, H., Breivik, L.-A. (2010) Sea ice motion from low-  
1676 resolution satellite sensors: an alternative method and its validation in the Arctic. *Journal of Geophysical  
1677 Research: Oceans*, 115, C10032. <https://doi.org/10.1029/2009JC005958>

1678

1679 Laffin, M. K., Zender, C. S., Singh, S., Van Wessem, J. M., Smeets, C. J. P. P., Reijmer, C. H. (2021)  
1680 Climatology and evolution of the Antarctic Peninsula foehn wind-induced melt regime from 1979-2018.  
1681 Journal of Geophysical Research: Atmospheres, 126, e2020JD033682.  
1682 <https://doi.org/10.1029/2020JD033682>

1683

1684 Lazzara, M. (2024) Antarctic Meteorological Research Center & Automatic Weather Stations Project  
1685 [Dataset]. Accessed on 12 May 2024, available online at <https://amrc.ssec.wisc.edu/>.

1686

1687 Lea, E. J., Jamieson, S. S. R., Bentley, M. J. (2024) Alpine topography of the Gamburtsev Subglacial  
1688 Mountains, Antarctica, mapped from ice sheet surface morphology. *The Cryosphere*, 18, 1733-1751.  
1689 <https://doi.org/10.5194/tc-18-1733-2024>

1690

1691 Li, H., Fedorov, A. V. (2021) Persistent freshening of the Arctic Ocean and changes in the North Atlantic  
1692 salinity caused by Arctic sea ice decline. *Climate Dynamics*, 57, 2995-3013.  
1693 <https://doi.org/10.1007/s00382-021-05850-5>

1694

1695 Li, X.-Q., Hui, F.-M., Zhao, J.-C., Zhai, M.-X., Cheng, X. (2022) Thickness simulation of landfast ice  
1696 along Mawson Coast, East Antarctica based on a snow/ice high-resolution thermodynamic model.  
1697 *Advances in Climate Change Research*, 13, 375-384. <https://doi.org/10.1016/j.accre.2022.05.005>

1698

1699 Liang, K., Wang, J., Luo, H., Yang, Q. (2023) The role of atmospheric rivers in Antarctic sea ice variations.  
1700 *Geophysical Research Letters*, 50, e2022GL102588. <https://doi.org/10.1029/2022GL102588>

1701

1702 Liao, Z., Cheng, B., Zhao, J., Vihma, T., Jackson, K., Yang, Q., Yang, Y., Zhang, L., Li, Z., Qiu, Y., Cheng,  
1703 X. (2018). Snow depth and ice thickness derived from SIMBA ice mass balance buoy data using an  
1704 automated algorithm. *International Journal of Digital Earth*, 12(8), 962-979.  
1705 <https://doi.org/10.1080/17538947.2018.1545877>

1706

1707 Liao, S., Luo, H., Wang, J., Shi, Q., Zhang, J., Yang, Q. (2022) An evaluation of Antarctic sea-ice thickness  
1708 from the Global Ice-Ocean Modeling and Assimilation System based on it situ and satellite observations.  
1709 The Cryosphere, 16, 1807-1819. <https://doi.org/10.5194/tc-16-1807-2022>

1710

1711 Lin, P., Zhong, R., Yang, Q., Clem, K. R., Chen, D. (2023) A record breaking cyclone over the southern  
1712 ocean in 2022. *Geophysical Research Letters*, 50, e2023GL104012.  
1713 <https://doi.org/10.1029/2023GL104012>

1714

1715 Liu, Y., Key, J. R., Wang, X., Tschudi, M. (2020) Multidecadal Arctic sea ice thickness and volume derived  
1716 from ice age. *The Cryosphere*, 14, 1325-1345. <https://doi.org/10.5194/tc-14-1325-2020>

1717

1718 Maksym, T., Markus, T. (2008) Antarctic sea ice thickness and snow-to-ice conversion from atmospheric  
1719 reanalysis and passive microwave snow depth. *Journal of Geophysical Research*, 113, C02S12.  
1720 <https://doi.org/10.1029/2006JC004085>

1721

1722 Maksym, T., Stammerjohn, S., Ackley, S., Massom, R. (2012) Antarctic sea ice – A polar opposite?  
1723 *Oceanography* 25, 140-151. <https://doi.org/10.5670/oceanog.2012.88>

1724

1725 Marengo, J. A., Soares, W. R., Saulo, C., Nicolini, M. (2004) Climatology of the Low-Level Jet East of the  
1726 Andes as Derived from the NCEP-NCAR Reanalyses: Characteristics and Temporal Variability. *Journal of*  
1727 *Climate*, 17, 2261-2280. [https://doi.org/10.1175/1520-0442\(2004\)017<2261:COTLJE>2.0.CO;2](https://doi.org/10.1175/1520-0442(2004)017<2261:COTLJE>2.0.CO;2)

1728

1729 Marshall, G. J. (2003) Trends in the Southern Annular Mode from Observations and Reanalyses. *Journal*  
1730 of *Climate*, 16, 4134-4143. [https://doi.org/10.1175/1520-0442\(2003\)016<4134:TITSAM>2.0.CO;2](https://doi.org/10.1175/1520-0442(2003)016<4134:TITSAM>2.0.CO;2)

1731

1732 Massom, R.A., H. Eicken, C. Haas, M.O. Jeffries, M.R. Drinkwater, M. Sturm, A.P. Worby, X. Wu, V.I.  
1733 Lytle, S. Ushio, K. Morris, P.A. Reid, S. Warren, and I. Allison. (2001) Snow on Antarctic sea ice. *Reviews*  
1734 of *Geophysics*, 39(3), 413-445. <https://doi.org/10.1029/2000RG000085>

1735

1736 Massom, R. A., Pook, M. J., Comiso, J. C., Adams, N., Turner, J., Lachlan-Cope, T., Gibson, T. T. (2004)  
1737 Precipitation over the interior East Antarctic Ice Sheet related to mid-latitude blocking-high activity.  
1738 *Journal of Climate*, 17, 1914-1928. [https://doi.org/10.1175/1520-0442\(2004\)017%3C1914:POTIEA%3E2.0.CO;2](https://doi.org/10.1175/1520-0442(2004)017%3C1914:POTIEA%3E2.0.CO;2)

1740

1741 Massonnet, F., Mathiot, P., Fichefet, T., Goosse, H., Beatty, C. K., Vancopenolle, M., Lavergne, T. (2013)  
1742 A model reconstruction of the Antarctic sea ice thickness and volume changes over 1980-2008 using data  
1743 assimilation. *Ocean Modeling*, 64, 67-75. <https://doi.org/10.1016/j.ocemod.2013.01.003>

1744

1745 Matejka, M., Laska, K., Jeklova, K., Hosek, J. (2021) High-Resolution Numerical Modeling of Near-  
1746 Surface Atmospheric Fields in the Complex Terrain of James Ross Island, Antarctic Peninsula.  
1747 *Atmosphere*, 12, 360. <https://doi.org/10.3390/atmos12030360>

1748

1749 Mathworks (2024) Math. Graphics. Programming [Software]. Accessed on 18 March 2024, available online  
1750 at <https://uk.mathworks.com/products/matlab.html>

1751

1752 McLennan, M. L., Lenaerts, J. T. M., Shields, C. A., Hoffman, A. O., Wever, N., Thompson-Munson, M.,  
1753 Winters, A. C., Pettit, E. C., Scambos, T. A., Wille, J. D. (2023) Climatology and surface impacts of  
1754 atmospheric rivers on West Antarctica. *The Cryosphere*, 17, 865-881. <https://doi.org/10.5194/tc-17-865-2023>

1755

1756

1757 McLennan, M. L., Lenaerts, J. T. M., Shields, C., Wille, J. D. (2022) Contribution of atmospheric rivers to  
1758 Antarctic precipitation. *Geophysical Research Letters*, 49, e2022GL100585.  
1759 <https://doi.org/10.1029/2022GL100585>

1760

1761 Meredith, M. P., Stammerjohn, S. E., Ducklow, H. W., Leng, M. J., Arrowsmith, C., Brearley, J. A.,  
1762 Venables, H. J., Barham, M., van Wessem, J. M., Schofield, O., Waite, N. (2021) Local- and large-scale  
1763 drivers of variability in the coastal freshwater budget of the Western Antarctic Peninsula. *Journal of*  
1764 *Geophysical Research: Oceans*, 126, e2021JC017172. <https://doi.org/10.1029/2021JC017172>

1765

1766 Miles, B. W. J., Stokes, C. R., Jamieson, S. S. R. (2017) Simultaneous disintegration of outlet glaciers in  
1767 Porpoise Bay (Wilkes Land), East Antarctica, driven by sea ice break-up. *The Cryosphere*, 11, 427-442.  
1768 <https://doi.org/10.5194/tc-11-427-2017>

1769  
1770 Mills, C. M. (2011) Modification of the Weather Research and Forecasting Model's treatment of sea ice  
1771 albedo over the Arctic Ocean. WRF3.3.1 Code Submission Doc., 2 pp. Accessed on 19 August 2024,  
1772 available online at  
1773 [http://publish.illinois.edu/catrinmills/files/2012/10/Mills\\_WRFIceAlbedoProj\\_Summary.pdf](http://publish.illinois.edu/catrinmills/files/2012/10/Mills_WRFIceAlbedoProj_Summary.pdf)

1774  
1775 Montini, T. L., Jones, C., Carvalho, L. M. V. (2019) The South American low-level jet: A new climatology,  
1776 variability, and changes. *Journal of Geophysical Research: Atmospheres*, 124, 1200-1218.  
1777 <https://doi.org/10.1029/2018JD029634>

1778  
1779 Morrison, H., Milbrandt, J. A. (2015) Parameterization of Cloud Microphysics Based on the Prediction of  
1780 Bulk Ice Particle Properties. Part I: Scheme Description and Idealized Tests. *Journal of the Atmospheric*  
1781 *Sciences*, 72, 287-311. <https://doi.org/10.1175/JAS-D-14-0065.1>

1782  
1783 Nakanishi, M., Niino, H. (2006) An improved Mellor-Yamada level-3 model: Its numerical stability and  
1784 application to a regional prediction of advection fog. *Boundary-Layer Meteorology*, 119, 397-407.  
1785 <https://doi.org/10.1007/s10546-005-9030-8>

1786  
1787 Nelli, N. R., Francis, D., Fonseca, R., Abida, R., Weston, M., Wehbe, Y., Al Hosary, T. (2021) The  
1788 atmospheric controls of extreme convective events over the southern Arabian Peninsula during the spring  
1789 season. *Atmospheric Research*, 262, 105788. <https://doi.org/10.1016/j.atmosres.2021.105788>

1790  
1791 NOAA ARL (2024) HYSPLIT for Linux - Public (unregistered) version download [Software]. National  
1792 Oceanic and Atmospheric Administration Air Resources Laboratory. Accessed on 04 July, available online  
1793 at [https://www.ready.noaa.gov/HYSPLIT\\_linuxtri](https://www.ready.noaa.gov/HYSPLIT_linuxtri)

1794  
1795 NOAA/NWS (2024) Cold & Warm Episodes by Season [Dataset]. National Oceanic and Atmospheric  
1796 Administration / National Weather Service Climate Prediction Center. Accessed on 24 July, available  
1797 online at [https://origin.cpc.ncep.noaa.gov/products/analysis\\_monitoring/ensostuff/ONI\\_v5.php](https://origin.cpc.ncep.noaa.gov/products/analysis_monitoring/ensostuff/ONI_v5.php)

1798  
1799 Oliveira, F. N. M., Carvalho, L. M. V., Ambrizzi, T. (2013) A new climatology for Southern Hemisphere  
1800 blockings in the winter and the combine defect of ENSO and SAM phases. *International Journal of*  
1801 *Climatology*, 34, 676-1692. <https://doi.org/10.1002/joc.3795>

1802  
1803 Oolman, L. (2025) University of Wyoming - atmospheric soundings [Dataset]. Accessed on 04 July 2024,  
1804 data available online at <https://weather.uwyo.edu/upperair/sounding.html>

1805  
1806 Parkinson, C. L. (2019) A 40-y record reveals gradual Antarctic sea ice increases followed by decreases at  
1807 rates far exceeding the rates seen in the Arctic. *Environmental Sciences*, 116, 14414-14423.  
1808 <https://doi.org/10.1073/pnas.1906556116>

1809

1810 Parkinson, C. L., Cavalieri, D. J. (2012) Antarctic sea ice variability and trends, 1979-2010. The  
1811 Cryosphere, 6, 871-880. <https://doi.org/10.5194/tc-6-871-2012>

1812

1813 Plante, M., Lemieux, J.-F., Tremblay, L. B., Tivy, A., Angnatok, J., Roy, F., Smith, G., Dupont, F., Turner,  
1814 A. K. (2024) Using Icepack to reproduce ice mass balance buoy observations in landfast ice: improvements  
1815 from the mushy-layer thermodynamics. The Cryosphere, 18, 1685-1708. <https://doi.org/10.5194/tc-18-1685-2024>

1816

1817

1818 Pook, M. J., Risbey, J. S., McIntosh, P. C., Ummenhofer, C. C., Marshall, A. G., Meyers, G. A. (2013) The  
1819 seasonal cycle of blocking and associated physical mechanisms in the Australian region and relationship  
1820 with rainfall. Monthly Weather Review, 141, 4534-4553. <https://doi.org/10.1175/MWR-D-13-00040.1>

1821

1822 Purich, A., Doddridge, E. W. (2023) Record low Antarctic sea ice coverage indicates a new sea ice state.  
1823 Communications Earth & Environment, 4, 314. <https://doi.org/10.1038/s43247-023-00961-9>

1824

1825 PWRF (2024) The Polar WRF. Byrd Polar and Climate Research Center. The Ohio State University  
1826 [Model]. Accessed on 08 April 2024, available online at <https://polarmet.osu.edu/PWRF/>.

1827

1828 Quan, J., Di, Z., Duan, Q., Gong, W., Wang, C., Gan, Y., Ye, A., Miao, C. (2016) An evaluation of  
1829 parametric sensitivities of different meteorological variables simulated by the WRF model. Quarterly  
1830 Journal of the Royal Meteorological Society, 142, 2925-2934. <https://doi.org/10.1002/qj.2885>

1831

1832 Ratna, S. B., Behera, S., Ratnam, J. V., Takahashi, K., Yamagata, T. (2013) An index for tropical temperate  
1833 troughs over southern Africa. Climate Dynamics, 41, 421-441. <https://doi.org/10.1007/s00382-012-1540-8>

1834

1835 Raphael, M. N., Hobbs, W., Wainer, I. (2011) The effect of Antarctic sea ice on the Southern Hemisphere  
1836 atmosphere during the southern summer. Climate Dynamics, 36, 1403-1417.  
1837 <https://doi.org/10.1007/s00382-010-0892-1>

1838

1839 Raphael, M. N., Marshall, G. J., Turner, J., Fogt, R. L., Schneider, D., Dixon, D. A., Hosking, J. S., Jones,  
1840 J. M., Hobbs, W. R. (2016) The Amundsen Sea Low: Variability, Change, and Impact on Antarctic Climate.  
1841 Bulletin of the American Meteorological Society, 97, 111-121. <https://doi.org/10.1175/BAMS-D-14-00018.1>

1842

1843

1844 Rauber, R., M., Hu, H., Dominguez, F., Nesbitt, S. W., McFarquhar, G. M., Zaremba, T. J., Finlon, J. A.  
1845 (2020) Structure of an atmospheric river over Australia and the Southern Ocean. Part I: Tropical and  
1846 midlatitude water vapor fluxes. Journal of Geophysical Research: Atmospheres, 125, e2020JD032513.  
1847 <https://doi.org/10.1029/2020JD032513>

1848

1849 Reid, P., Stammerjohn, S., Massom, R. A., Barreira, S., Scambos, T., Lieser, J. L. (2024) Sea-ice extent,  
1850 concentration, and seasonality [in “State of the Climate in 2023”]. Bulletin of the American Meteorological  
1851 Society, 105, 350-353. <https://doi.org/10.1175/BAMS-D-24-0099.1>

1852

1853 Riihelä, A., Bright, R. M., Anttila, K. (2021) Recent strengthening of snow and ice albedo feedback driven  
1854 by Antarctic sea-ice loss. *Nature Geosciences*, 14, 832-836. <https://doi.org/10.1038/s41561-021-00841-x>

1855

1856 Roach, L. A., Dorr, J., Holmes, C. R., Massonnet, F., BLockley, E. W., Notz, D., Rackow, T., Raphael, M.  
1857 N., O'Farrell, S. P., Bailey, D. A., Bitz, C. M. (2020) Antarctic Sea Ice Area in CMIP6. *Geophysical  
1858 Research Letters*, 47, e2019GL086729. <https://doi.org/10.1029/2019GL086729>

1859

1860 **Schroeter, S., Hobbs, W., Bindoff, N. L., Massom, R., Matear, R. (2018) Drivers of Antarctic sea ice volume  
1861 change in CMIP5 models. *Journal of Geophysical Research: Oceans*, 123, 7914-7938.  
1862 <https://doi.org/10.1029/2018JC014177>**

1863

1864 Schroeter, S., Sandery, P. A. (2022) Large-ensemble analysis of Antarctic sea ice model sensitivity to  
1865 parameter uncertainty. *Ocean Modeling*, 177, 102090. <https://doi.org/10.1016/j.ocemod.2022.102090>

1866

1867 Sledd, A., Shupe, M. D., Solomon, A., Cox, C. J., Perovich, D., Lei, R. (2024) Snow thermal conductivity  
1868 and conductive flux in the Central Arctic: Estimates from observations and implications for models.  
1869 *Elements: Science of the Anthropocene*, 12, 00086. <https://doi.org/10.1525/elementa.2023.00086>

1870

1871 Skamarock, W. C., Klemp, J. B., Dudhia, J., Gill, D. O., Liu, Z., Berner, J., Wang, W., Powers, J. G., Duda,  
1872 M. G., Barker, D., Huang, X.-Y. (2019) Description of the Advanced Research WRF Model Version 4.3  
1873 (No. NCAR/TN-556+STR). Accessed on 03 June 2024, available online at  
1874 <https://opensky.ucar.edu/islandora/object/opensky:2898>

1875

1876 Spreen, G., Kaleschke, L., Heygster, G. (2008) Sea ice remote sensing using AMSR-E 89-GHz channels.  
1877 *Journal of Geophysical Research*, 113, C02S03. <https://doi.org/10.1029/2005JC003384>

1878

1879 Stein, A. F., Draxler, R. R., Rolph, G. D., Stunder, B. J. B., Cohen, M. D., Ngan, F. (2015) NOAA's  
1880 HYSPLIT atmospheric transport and dispersion modeling system. *Bulletin of the American Meteorological  
1881 Society*, 96, 2059-2077. <https://doi.org/10.1175/BAMS-D-14-00110.1>

1882

1883 **Sturm, M., Massom, R. A. (2017) Snow in the Sea Ice System: Friend or Foe? In D. Thomas (editor): Sea  
1884 Ice. 3rd Edition, Wiley Blackwell, New York (USA) and Oxford (UK), pp. 65-109.  
1885 <https://doi.org/10.1002/9781118778371.eh3>**

1886

1887 Szapiro, N., Cavallo, S. (2018) TPVTrack v1.0: A watershed segmentation and overlap correspondence  
1888 method for tracking tropopause polar vortices. *Geoscientific Model Development*, 11, 5173-5187.  
<https://doi.org/10.5194/gmd-11-5173-2018>

1889

1890 Takaya, K., Nakamura, H. (2001) A Formulation of a Phase-Independent Wave-Activity Flux for Stationary  
1891 and Migratory Quasigeostrophic Eddies on a Zonally Varying Basic Flow. *Journal of the Atmospheric  
1892 Sciences*, 58, 608-627. [https://doi.org/10.1175/1520-0469\(2001\)058<0608:AFOAPI>2.0.CO;2](https://doi.org/10.1175/1520-0469(2001)058<0608:AFOAPI>2.0.CO;2)

1893

1894 Tewari, M., Chen, F., Wang, W., Dudhia, J., Lemone, M. A., Mitchell, K. E., et al. (2004) Implementation  
and verification of the unified NOAH land surface model in the WRF model. *20th Conference on Weather  
Analysis and Forecasting/16th Conference on Numerical Weather Prediction*, Seattle, W, American

1895 Meteorological Society, 14.2.a. Accessed on 25 January 2024, available online at  
1896 <https://opensky.ucar.edu/islandora/object/conference:1576>

1897 Tewari, K., Mishra, S. K., Salunke, P., Ozawa, H., Dewan, A. (2023) Potential effects of the projected  
1898 Antarctic sea-ice loss on the climate system. *Climate Dynamics*, 60, 589-601.  
1899 <https://doi.org/10.1007/s00382-022-06320-2>

1900 Thomas, D (editor) (2017) *Sea Ice*. 3rd Edition. Wiley-Blackwell, New York (USA) and Oxford (UK), 664  
1901 pp. ISBN: 978-1-118-77838-8.

1902 Terpstra, A., Gorodetskaya, I. V., Sodemann, H. (2021) Linking sub-tropical evaporation and extreme  
1903 precipitation over East Antarctica: An atmospheric river case study. *Journal of Geophysical Research:  
1904 Atmospheres*, 126, e2020JD033617. <https://doi.org/10.1029/2020JD033617>

1905 Trusel, L. D., Kromer, J. D., Datta, R. T. (2023) Atmospheric Response to Antarctic Sea-Ice Reductions  
1906 Drives Ice Sheet Surface Mass Balance Increase. *Journal of Climate*, 19, 6879-6896.  
1907 <https://doi.org/10.1175/JCLI-D-23-0056.1>

1908 Turner, J., Phillips, T., Thamban, M., Rahaman, W., Marshall, G. J., Wille, J. D., Favier, V., Holly, V.,  
1909 Winton, L., Thomas, E., Wang, Z., van den Broeke, M., Hosking, J. S., Lachlan Cope, T. (2019) The  
1910 dominant role of extreme precipitation events in Antarctic snowfall variability. *Geophysical Research  
1911 Letters*, 46, 3502-3511. <https://doi.org/10.1029/2018GL081517>

1912 University of Bremen (UoB) (2024) Sea Ice Remote Sensing, Data Archived. Accessed on 01 August 2024,  
1913 available online at <https://data.seaice.uni-bremen.de/>.

1914 Vignon, E., Alexander, S. P., DeMott, P. J., Sotiropoulou, G., Gerber, F., Hill, T. C. J., Marchand, R.,  
1915 Nenes, A., Berne, A. (2021) Challenging and improving the simulation of mid-level mixed-phase clouds  
1916 over the high-latitude Southern Ocean. *Journal of Geophysical Research: Atmospheres*, 126,  
1917 e2020JD033490. <https://doi.org/10.1029/2022JD033490>

1918 Vignon, E., Traulle, O., Berne, A. (2019) On the fine vertical structure of the low troposphere over coastal  
1919 margins of East Antarctica. *Atmospheric Chemistry and Physics*, 19, 4659-4683.  
1920 <https://doi.org/10.5194/acp-19-4659-2019>

1921 Wallace, J. M., Hobbs, P. V. (2006) *Atmospheric science: An introductory survey*. 504 pp. Academic Press  
1922 Inc., second edition. ISBN-10: 012732951X, ISBN-13: 978-0127329512.

1923 Wang, Z., Li, Z., Zeng, J., Liang, S., Zhang, P., Tang, F., Chen, S., Ma, X. (2020) Spatial and temporal  
1924 variations of Arctic sea ice from 2002 to 2017. *Earth and Space Science*, 7, e2020EA001278.  
1925 <https://doi.org/10.1029/2020EA001278>

1926 Wang, M., Linhardt, F., Lion, V., Oppelt, N. (2024) Melt Pond Evolution along the MOSAiC Drift:  
1927 Insights from Remote Sensing and Modeling. *Remote Sensing*, 16, 3748.  
1928 <https://doi.org/10.3390/rs16193748>

1933

1934 Wang, J., Massonnet, F., Goosse, H., Luo, H., Barthelemy, A., Wang, Q. (2024) Synergistic atmosphere-ocean-ice influences have driven the 2023 all-time Antarctic sea-ice record low. *Communications Earth & Environment*, 5, 415. <https://doi.org/10.1038/s43247-024-01523-3>

1935

1936

1937

1938 Webster, M., Gerland, S., Holland, M., Hunke, E., Kwok, R., Lecomte, O., Masson, R., Perovich, D., Sturm, M. (2018) Snow in the changing sea-ice system. *Nature Climate Change*, 8, 945-954. <https://doi.org/10.1038/s41558-018-0286-7>

1939

1940

1941

1942 Wille, J. D., Alexander, S. P., Amory, C., Baiman, R., Barthelemy, L., Bergstrom, D. M., Berne, A., Binder, H., Blanchet, J., Bozkurt, D., Bracegirdle, T. J., Casado, M., Choi, T., Clem, K. R., Cordron, F., Datta, R., Di Battista, S., Favier, V., Francis, D., Fraser, A. D., Fourre, E., Garreaud, R. D., Genthon, C., Goorodetskaya, I. V., Gonzalez-Herrero, S., Heinrich, V. J., Hubert, G., Joos, H., Kim, S.-J., King, J. C., Kittel, C., Landais, A., Lazzara, M., Leonard, G. H., Lieser, J. L., MacLennan, M., Mikolajczyk, D., Neff, P., Ollivier, I., Picard, G., Pohl, B., Ralph, F. M., Rowe, P., Schlosser, E., Shields, C. A., Smith, I. J., Sprenger, M., Trusel, L., Udy, D., Vance, T., Vignon, E., Walker, C., Wever, N., Zou, X. (2024a) The Extraordinary March 2022 East Antarctica “Heat” Wave. Part I: Observations and Meteorological Drivers. *Journal of Climate*, 37, 757-778. <https://doi.org/10.1175/JCLI-D-23-0175.1>

1951

1952 Wille, J. D., Alexander, S. P., Amory, C., Baiman, R., Barthelemy, L., Bergstrom, D. M., Berne, A., Binder, H., Blanchet, J., Bozkurt, D., Bracegirdle, T. J., Casado, M., Choi, T., Clem, K. R., Cordron, F., Datta, R., Di Battista, S., Favier, V., Francis, D., Fraser, A. D., Fourre, E., Garreaud, R. D., Genthon, C., Goorodetskaya, I. V., Gonzalez-Herrero, S., Heinrich, V. J., Hubert, G., Joos, H., Kim, S.-J., King, J. C., Kittel, C., Landais, A., Lazzara, M., Leonard, G. H., Lieser, J. L., MacLennan, M., Mikolajczyk, D., Neff, P., Ollivier, I., Picard, G., Pohl, B., Ralph, F. M., Rowe, P., Schlosser, E., Shields, C. A., Smith, I. J., Sprenger, M., Trusel, L., Udy, D., Vance, T., Vignon, E., Walker, C., Wever, N., Zou, X. (2024b) The Extraordinary March 2022 East Antarctica “Heat” Wave. Part II: Impacts on the Antarctic Ice Sheet. *Journal of Climate*, 37, 779-799. <https://doi.org/10.1175/JCLI-D-23-0176.1>

1961

1962 Webster, M., Gerland, S., Holland, M., Hunke, E., Kwok, R., Lecomte, O., Masson, R., Perovich, D., Sturm, M. (2018) Snow in the changing sea ice system. *Nature Climate Change*, 8, 945-954. <https://doi.org/10.1038/s41558-018-0286-7>

1963

1964

1965

1966 Wille, J. D., Bromwich, D. H., Cassano, J. J., Nigro, M. A., Mateling, M. E., Lazzara, M. A. (2017) Evaluation of the AMPS Boundary Layer Simulations on the Ross Ice Shelf, Antarctica, with Unmanned Aircraft Observations. *Journal of Applied Meteorology and Climatology*, 56, 2239-2258. <https://doi.org/10.1175/JAMC-D-16-0339.1>

1967

1968

1969

1970

1971 Wille, J. D., Bromwich, D. H., Nigro, M. A., Cassano, J. J., Mateling, M., Lazzara, M. A., Wang, S.-H. (2016) Evaluation of the AMPS Boundary Layer Simulations on the Ross Ice Shelf with Tower Observations. *Journal of Applied Meteorology and Climatology*, 55, 2349-2367. <https://doi.org/10.1175/JAMC-D-16-0032.1>

1972

1973

1974

1975

1976 Wille, J. D., Favier, V., Dufour, A., Gorodetskaya, I. V., Turner, J., Agosta, C., Codron, F. (2019) West  
 1977 Antarctic surface melt triggered by atmospheric rivers. *Nature Geoscience*, 12, 911-916.  
 1978 <https://doi.org/10.1038/s41561-019-0460-1>

1979

1980 Wille, J. D., Favier, V., Gorodetskaya, I. V., Agosta, C., Baiman, R., Barrett, J. E., Barthelemy, L., Boza,  
 1981 B., Bozkurt, D., Casado, M., Chyhareva, A., Clem, K. R., Codron, F., Datta, R. T., Duran-Alarcon, C.,  
 1982 Francis, D., Hoffman, A. O., Kolbe, M., Krakosvska, S., Linscott, G., MacLennan, M. L., Mattingly, K. S.,  
 1983 Mu, Y., Pohl, B., Santos, C. L.-D., Shields, C. A., Toker, E., Winters, A. C., Yin, Z., Zou, X., Zhang, C.,  
 1984 Zhang, Z. (2025) Atmospheric rivers in Antarctica. *Nature Reviews Earth & Environment*, 6, 178-192.  
 1985 <https://doi.org/10.1038/s43017-024-00638-7>

1986

1987 Wille, J. D., Favier, V., Gorodetskaya, I. V., Agosta, C., Kittel, C., Beeman, J. C., Jourdain, N. C., Lenaerts,  
 1988 J. T. M., Codron, F. (2021) Antarctic atmospheric river climatology and precipitation impacts. *Journal of*  
 1989 *Geophysical Research: Atmospheres*, 126, e2020JD033788. <https://doi.org/10.1029/2020JD033788>

1990

1991 Wille, J. D., Pohl, B., Favier, V., Winters, A. C., Baiman, R., Cavallo, S. M., Leroy-Dos Santos, C., Clem,  
 1992 K., Udy, D. G., Vance, T. R., Gorodetskaya, I., Codron, F., Berchet, A. (2024c) Examining atmospheric  
 1993 river life cycles in East Antarctica. *Journal of Geophysical Research: Atmospheres*, 129, e2023JD039970.  
 1994 <https://doi.org/10.1029/2023JD039970>

1995

1996 Williams, N., Byrne, N., Feltham, D., Van Leeuwen, P. J., Bannister, R., Schroeder, D., Ridout, A., Nerger,  
 1997 L. (2023) The effects of assimilating a sub-grid-scale sea ice thickness distribution in a new Arctic sea ice  
 1998 data assimilation system. *The Cryosphere*, 17, 2509-2532. <https://doi.org/10.5194/tc-17-2509-2023>

1999

2000 Worby, A. P., Steer, A., Lieser, J. L., Heil, P., Yi, D., Markus, T., Allison, I., Massom, R. A., Galin, N.,  
 2001 Zwally, J. (2011) Regional-scale sea-ice and snow thickness distribution from in situ and satellite  
 2002 measurements over East Antarctica during SIPEX 2007. *Deep Sea Research Part II: Topical Studies in*  
 2003 *Oceanography*, 58, 1125-1136. <https://doi.org/10.1016/j.dsr2.2010.12.001>

2004

2005 Xie, H., Ackley, S. F., Yi, D., Zwally, H. J., Wagner, P., Weissling, B., Lewis, M., Ye, K. (2011) Sea-ice  
 2006 thickness distribution of the Bellingshausen Sea from surface measurements and ICESat altimetry. *Deep*  
 2007 *Sea Research Part II: Topical Studies in Oceanography*, 58, 1039-1051.  
 2008 <https://doi.org/10.1016/j.dsr2.2010.10.038>

2009

2010 Xiong, X., Che, N., Barnes, W. L. (2006) Terra MODIS on board spectral characterization and  
 2011 performance. *IEEE Transactions on Geosciences and Remote Sensing*, 44, 8.  
 2012 <https://doi.org/10.1109/TGRS.2006.872083>

2013

2014 Xue, J., Xiao, Z., Bromwich, D. H., Bai, L. (2022) Polar WRF V4.1.1 simulation and evaluation for the  
 2015 Antarctic and Southern Ocean. *Frontiers of Earth Science*, 16, 1005-1024. <https://doi.org/10.1007/s11707-022-0971-8>

2017

2018 Yang, J., Xiao, X., Liu, J., Li, Q., Qin, D. (2021) Variability of Antarctic sea ice extent over the past 200 years.  
 2019 *Science Bulletin*, 66, 2394-2404. <https://doi.org/10.1016/j.scib.2021.07.028>

2020

2021 Zhang, J. (2014) Modeling the Impact of Wind Intensification on Antarctic Sea Ice Volume. *Journal of Climate*, 27, 202-214. <https://doi.org/10.1175/JCLI-D-12-00139.1>

2022

2023

2024 Zhang, R., Screen, J. A. (2021) Diverse Eurasian winter temperature responses to Barents-Kara sea ice anomalies of different magnitudes and seasonality. *Geophysical Research Letters*, 48, e2021GL092726. <https://doi.org/10.1029/2021GL092726>

2025

2026

2027

2028 Zeng, X., Beljaars, A. (2005) A prognostic scheme of sea surface skin temperature for modeling and data assimilation. *Geophysical Research Letters*, 32, L14605. <https://doi.org/10.1029/2005GL023030>

2029

2030

2031 Zou, X., Bromwich, D. H., Montenegro, A., Wang, S.-H., Bai, L. (2021a) Major surface melting over the Ross Ice Shelf part I: Foehn effect. *Quarterly Journal of the Royal Meteorological Society*, 147, 2874-2894. <https://doi.org/10.1002/qj.4104>

2032

2033

2034

2035 Zou, X., Bromwich, D. H., Montenegro, A., Wang, S.-H., Bai, L. (2021b) Major surface melting over the Ross Ice Shelf part II: Surface energy balance. *Quarterly Journal of the Royal Meteorological Society*, 147, 2895-2916. <https://doi.org/10.1002/qj.4105>

2036

2037

2038

2039 Zou, X., Rowe, P. M., Gorodetskaya, I., Bromwich, D. H., Lazzara, M. A., Cordero, R. R., Zhang, Z., Kawzenuk, B., Cordeira, J. M., Wille, J. D., Ralph, F. M., Bai, L.-S. (2023) Strong warming over the Antarctic Peninsula during combined atmospheric River and foehn events: Contribution of shortwave radiation and turbulence. *Journal of Geophysical Research: Atmospheres*, 128, e2022JD038138. <https://doi.org/10.1029/2022JD038138>

2040

2041

2042

2043